Politecnico di Milano

School of Industrial and Information Engineering
Master of Science in Materials Engineering
and Nanotechnology

Functional CVD Graphene
for
Sensing Applications

Candidate
Tiziana Bardelli
ID n. 799139

Supervisors
Prof. Carlo E. Bottani
Dr Antonio Lombardo

Academic Year 2013–2014

Acknowledgments

First of all, I am really grateful to Prof. Carlo E. Bottani and Prof. Andrea Ferrari for giving me the opportunity to have this fantastic experience at the Cambridge Graphene Centre. These months in Cambridge highly enriched my knowledge and gave me a really useful life experience.

I would like to acknowledge the help of all the people who assisted me throughout this research project. In particular, I want to thank Dr Antonio Lombardo, my tutor, for assisting me step by step through all my project and sharing with me all his experience in the research field.

A big thanks also to Ugo Sassi, my desk-mate, for supporting me in all this work and training me on the growth of CVD graphene. Thanks to Dr Antonio Lombardo, Ugo Sassi, Domenico De Fazio, Matteo Barbone, Dr Anestis Katsounaros and Silvia Milana for training and helping me on the use of all the processes useful in the project, the Raman Spectrometer, the AFM, the Probe Station, the procedure to transfer graphene and many others.

Furthermore, I want to mention Anna Katharina Ott, Dr Ilya Goykhman, Dr Matteo Bruna, Dr Chang Goo Kang, Dr Alan Colli, Dr Mari Ijas, Giovanni Vescio, Dr Nicolas Decorde, Dr Panagiotis Karagiannidis, Lucia Lombardi, Flavia Tomarchio, Anna Eiden, Dr Valentin Wittwer, Dr Felice Torrisi, Dr Daniel Popa, Dr Anna Motta and all the people of the Cambridge Graphene Centre. Thanks to all these brilliant students and researchers for creating an inspirational and pleasant working environment, and for sharing with me their professional and academic experiences.

Thanks also to Marcello for being my personal computer supporter.

This project for me is not only a eight months experience in Cambridge but it is also the end of the work done in my last five years studying engineering, thus I would like to thank all the people that went along with me. Marco as big support in my first years in Milan. Lidia, Andrea, Francesco, Marco, Ambra, Alessandro, Francesco and Simone as great classmates. Lidia, Samantha, Mari, Giovanni, Hugo, David, David and Dan for making my life in Cambridge full of wonderful experiences and Claudio for being a great friend always ready to challenge, comfort and support me during these months. Lastly Giorgia, Valeria, Valentina as best friends ready to follow and support me everywhere.

Finally, the most important thanks has to be done to my family, my grandparents Pasqua and Giovanni, my sister Eleonora and in particular to my parents Daniela and Corrado for morally and economically supporting me in these twenty four years of my life.

Contents

List of Figures

List of Tables

Abstract

Graphene is a monolayer of carbon atoms arranged into a two-dimensional honeycomb lattice, characterised by excellent optical, electronic and mechanical properties, such as high charge carrier mobility and optical transparency, in addition to flexibility, mechanical robustness and environmental stability.

Graphene is suitable for a large range of applications among which functional nanodevices for bio and gas sensing, due to its electronic structure and high surface to volume ratio that can lead to a very high sensitivity.

Several techniques have been developed for the production of graphene layers with different properties, in particular Chemical vapour deposition (CVD) is emerged as ideal process for large-scale applications.

In this work CVD growth of graphene has been investigated and optimized in order to achieve a novel functional material with high chemical reactivity and electrical conductivity, to be used for sensing application.

Particular treatments are often required to deposit specific functional groups, able to interact with a desired chemical specie on the surface. Since graphene's basal plane is hydrophobic and chemically inert, these treatments are difficult on a flat surface and always disrupt graphene's electrical conductivity. The presence of edges and defects on the surface can help the process, because of the increase of the reactivity of a defected layer with respect to a continuous one.

This work aims to the synthesis of a bilayer graphene consisting of a bottom continuous layer covered by top discontinuous one, consisting of small "islands". The bottom layer ensures high conductivity, while the top offers a large number of edges and therefore is highly suitable for functionalization.

Starting from the parameters normally used for the growth of polycrystalline single layer graphene on Cu foils, the effect of pressure, temperature, growth time and gas flow ratio have been investigated and optimized in order to obtain a densely packed amount of small islands to maximize the amount of available edges.

The optimized functional material has been investigated by optical and Raman analysis. Optical analysis allowed the visualization of the morphology of the surface and Raman analysis proved the quality of the graphene in the different areas.

The material has been also integrated into back-gated field effect transistors to investigate its conductivity, the charge carrier mobility and the contact resistance. Two sets of such devices, one with the standard CVD monolayer and one with the "functional" layer have been simultaneously characterised in order to compare the electrical properties of the two surfaces.

The "new" graphene showed an high enhancement in reactivity. Contact resistance almost one order of magnitude less than the standard monolayer has been measured. A slightly change in the electrical performance has been also found, sheet resistance is increased and mobility is decreased. The presence of the islands rises the number of edges, thus increases the reactivity, but also enhances the scattering of the electrons through the channel. Furthermore, the bottom continuous layer was found less doped and less effected by the environment. The islands act as a screen to shield the effect of the environment and partially protect the bottom one.

The more attractive applications for this material are in the field of sensors. The combined properties of the two layers offer the possibility of high sensitive and selective detectors. The highly conductive bottom layer can accurately sense the effect of exposure to specific molecules that react with the chemical species added with functionalization while the top reactive layer can help the functionalization process and enhance the selectivity, shielding the effect of other substances of the environment.

The devices investigated in this work are being tested for chemical functionalization in order to assess their suitability for detection of human chorionic gonadotropin, a cancer risk biomarker.

Sommario

Il grafene è un materiale bidimensionale costituito da uno strato monoatomico di atomi di carbonio disposti ai vertici di esagoni regolari. Tra le sue ottime proprietà ottiche, elettriche e meccaniche mostra alta trasparenza, elevata mobilità, flessibilità e una buona stabilità alla condizioni ambientali.

Date le sue peculiarità, la sua struttura elettronica e il suo elevato rapporto superficie-volume, può essere sfruttato per svariate applicazioni tra le quali nanodispositivi come biosensori e sensori gas ad alta sensibilità.

Negli anni sono state sviluppate diverse tecniche per la produzione di grafene, tra le quali la deposizione chimica da fase vapore (CVD) ha ottime potenzialità nella produzione di grafene su larga scala.

In questo progetto la crescita di grafene CVD è stata investigata ed ottimizzata per ottenere un materiale ad alta reattività chimica e buona conduttività elettrica ottimo per la realizzazione di sensori.

Spesso nella realizzazione di sensori sono necessari specifici trattamenti superficiali, in cui particolari gruppi funzionali vengono connessi alla superficie per renderla più sensibile alla presenza di specifiche molecole nell'ambiante. Essendo un materiale idrofobico e chimicamente inerte, questo processo è molto difficile da attuare su una superficie perfettamente regolare e riduce molto la conducibilità elettrica del grafene. La presenza di difetti e discontinuità potrebbe rendere molto più agevole la funzionalizzazione, in quanto aumenta il numero di legami liberi del sistema, migliorandone la reattività.

L'obiettivo di questo progetto consiste nella sintesi di una superficie multistrato di grafene con uno strato inferiore continuo e una strato superiore discontinuo composto da una serie piccole isole densamente impaccate. La parte inferiore assicura la conducibilità, mentre la presenza delle isole au-

menta il numero di legami liberi, utili per effettuare la funzionalizzazione.

Utilizzando la procedura standard per la crescita di grafene su rame, è stato investigato l'effetto di alcuni parametri - pressione, temperatura, tempo di crescita e rapporto tra i flussi di gas - in modo da ottimizzare la formazione di una superficie coperta da un alto numero di isole.

Per caratterizzare le superfici così ottenute sono stati utilizzati il microscopio ottico e la spettroscopia Raman. Tramite l'analisi ottica è stata identificata la morfologia del campione mentre con la spettroscopia Raman è stata verificata l'effettiva qualità della struttura.

Il materiale ottenuto è stato integrato in un transistor ad effetto di campo a tre terminali, per investigarne la conducibilità, la mobilità e la resistenza di contatto. Due set di dispositivi, uno sul grafene standard e uno sul nuovo materiale funzionale, sono stati costruiti simultaneamente in modo da poterne comparare le proprietà.

È stato ottenuto un notevole aumento di reattività nel nuovo materiale. La resistenza di contatto è diminuita di quasi un ordine di grandezza rispetto al grafene standard. Le proprietà elettriche sono leggermente peggiorate, in quanto la resistività di superficie è aumentata e la mobilità è diminuita. Lo strato discontinuo migliora molto la reattività nel materiale, data la presenza di un alto numeri di legami incompleti, ma nello stesso tempo aumenta le interazioni degli elettroni all'interno del canale. In più, il materiale è molto poco dopato e in generale meno affetto da variazioni dell'ambiente circostante. Lo isole schermano parzialmente l'interazione con l'esterno, proteggendo lo strato inferiore.

Date le sue qualità questo materiale è molto adatto per la produzione di sensori. La combinazione delle proprietà dei due strati è ottimale per la costruzione di sistemi ad elevata sensitività e selettività. Lo strato inferiore conduttivo è molto sensibile alla presenza di specifiche molecole interagenti con le specie chimiche aggiunte durante la funzionalizzazione mentre lo strato superiore permette la funzionalizzazione, data la sua alta reattività, e aumenta anche la selettività del sistema schermando l'effetto delle altre sostanze presenti nell'ambiente.

È in corso di realizzazione una funzionalizzazione chimica dei dispositivi sviluppati in questo progetto, per testarne il loro possibile utilizzo nel rilevare la presenza di gonadotropina corionica, ormone specifico associato ad un alto rischio di cancro.

Chapter 1

Introduction

Since 2010, when the two scientists Andre K. Geim and Konstantin S. Novoselov were awarded the Nobel Prize in Physics, graphene has received even growing attention from both the industrial and the scientific communities. The unique combination of properties of single layer graphene sheets, such as high mechanical strength, high elasticity and thermal conductivity, very high room temperature electron mobility and tunable optical properties, raised a great interest in the scientific community, especially in the areas of materials, physics, and chemistry. Different, but similarly fascinating properties are exhibited also by double, few, and multi-layers graphene [1].

Several production techniques have been developed to obtain graphene of different dimensions, shape and quality according the requirements of specific applications [2]. Nanoelectronics has the most demanding requirements, with low defect density single crystals, printable electronics can tolerate lower quality, e.g. lower mobility graphene, while other applications, such as biosensors, may require defective graphene [3].

Chemical vapour deposition (CVD) techniques are emerging as ideal processes for large-area graphene films for large-scale applications. Starting from few layers graphene growth on Ni and Co substrates, the first real uniform large area graphene on metal has been grown on polycrystalline Cu foil in 2009 [3]. Since then, the growth has been deeply studied and it is currently a research topic.

The exceptional electronic and thermal properties of graphene are particularly suitable for a range of new applications from flexible electronics

to functional nanodevices, such as biosensors, gas sensors and high performance transistors. Graphene devices and sensors promise to be a disruptive technology in next generation electronics and healthcare diagnostic applications, due to graphene's exceptional electronic properties and extreme surface to volume ratio which offer greatly enhanced sensitivity [4].

1.1 Motivation

The aim of this work is to investigate and optimize graphene CVD growth parameters in order to achieve a novel functional material combining high conductivity, field effect and chemical reactivity to be used for sensing application.

Graphene's basal plane is hydrophobic and chemically inert [5] and requires specific treatments, such as partial oxidation [6], reaction with salts [4] or surface silanization [7] in order to deposit functional groups such as hydroxyl or carboxyl [6] groups. Functionalization however disrupts graphene's electrical conductivity as a consequence of the localization of the π electrons [8]. On the other end, graphene edges have a much higher chemical reactivity than the basal plane and can be easily functionalized with different functional groups [9].

This work aims to the synthesis of a bilayer graphene made of a bottom continuous layer covered by top discontinuous ones, consisting of small "islands". The bottom layer ensures high conductivity, while the top offers a large number of edges and therefore is highly suitable for functionalization. The combined properties of the two layers offer therefore the possibility of sensitive detectors, as the highly conductive bottom layer can accurately sense the effect of exposure to specific molecules.

This work starts from the parameters normally used for the growth of polycrystalline single layer graphene on Cu foils. The effect of pressure, temperature, growth time and gas flow ratio have been investigated and optimized in order to obtain a densely packed amount of small island, thus maximizing the amount of available edges.

The optimized functional material has been investigated by optical and Raman analysis and it has been also integrated into back-gated field effect transistors to investigate its conductivity, the charge carrier mobility and

the contact resistance.

1.2 Structure of the thesis

The dissertation is organised as follows:

Chapter 2 reviews structure and properties of graphene, giving an overview of the main production method and the current applications.

Chapter 3 describes the growth of the graphene, the procedure to transfer it on desired substrates and all the technological step required to build the structure needed to measure the electronical properties. All the used instrumentations are explained in details.

Chapter 4 shows all the results obtained about the optimization of the CVD growth and the further electrical characterization.

Chapter 5 presents the conclusions, summarizing the main achievements and outlining possible future developments.

Chapter 2

Graphene

2.1 Structure and properties

Graphene is a monolayer of sp^2 hybridised carbon atoms, arranged in Bravais lattice with two atoms per basis, also known as honeycomb lattice [10, 11] and can be thought of as composed of benzene rings stripped out from their hydrogen atoms (Figure 2.1). In-plane σ bonds result from the sp^2 hybridization of the s, $2p_x$ and $2p_y$ orbitals and connect each atom with its three nearest neighbours, with a bond length of 1.42 $\AA$ [11]. The σ bonds are responsible for the robustness of the lattice structure in all allotropes. Due to the Pauli principle, these bands have a filled shell and, hence, form a deep valence band. The fourth carbon valence electron is in the $2p_z$ orbital. The $2p_z$ orbitals are orthogonal to the graphene plane and form the π bonds, which form a distributed electron cloud. Since each p_z orbital has one extra electron, the band is half filled [11].

2.1.1 Electronical properties

The hexagonal honeycomb lattice of graphene, with two carbon atoms per unit cell, leads to a rather unique band structure. Its electronic structure can be described using a tight-binding Hamiltonian [13].

The p_z electrons, which form the π bonds, can be treated independently from the other valence electrons. Within this π-band approximation the dispersion relation restricted to the first nearest neighbour interaction bring to the formation of two non interacting bands π and π^*.

The π states form the valence band and the π^* states the conduction

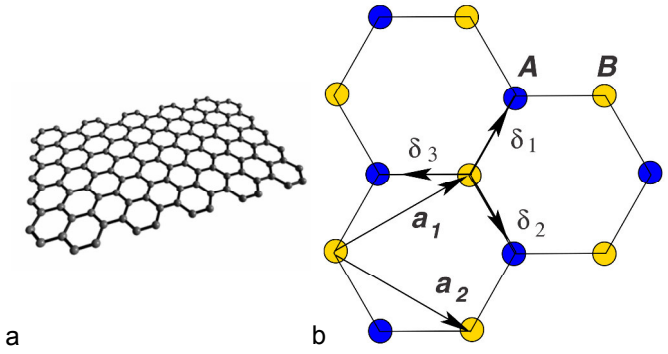

Figure 2.1: Graphene. a) Schematic of a graphene monolayer. Adapted from [12]. b) Lattice structure of graphene, made out of two interpenetrating triangular lattices. a_1 and a_2 are the lattice unit vectors, and $\delta_i, i = 1, 2, 3$ are the nearest-neighbour vectors. Adapted from [11].

band. These two bands touch at six points, the so-called Dirac points. Symmetry allows these six points to be reduced to a pair, K and K', which are independent of one another. If we limit ourselves to low energies, which are the most relevant in electron transport, the bands have a linear dispersion, in contrast with the usual quadratic energy-momentum relation obeyed by electrons at band edges in conventional semiconductors. The band structure can be viewed as two cones touching at E_{Dirac} (Figure 2.2). This is because the orthogonal π and π^* states do not interact, so their crossing is allowed. The fact that these bands touch at E_{Dirac} indicates that graphene has zero band gap, and it is therefore usually described as a zero-gap semiconductor. Since the band structure is symmetric about the Dirac point, electrons and holes in pure, free-standing graphene should have the same properties [13]. The full derivation of the electronic band structure is omitted here, but a detailed description can be found in [11].

Graphene's charge carriers exhibit very high carrier mobility, up to $\sim 10^6\ cm^2/Vs$ in suspended devices [14]. For samples deposited on a substrate, mobility is reduced due to scattering, caused by surface roughness, charge trapped, defects etc. On the most commonly used substrate, oxidized silicon wafers, graphene shows charge carrier mobilities up to a few thousands cm^2/Vs at room temperature [11] due to scattering and charge inhomogeneity.

Because of the linear low-energy spectrum, charge carrier transport in

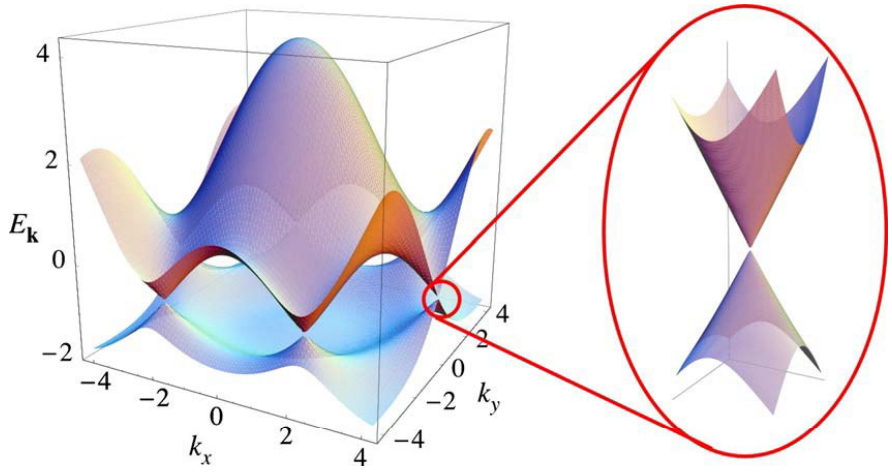

Figure 2.2: Energy band diagram of graphene with a zoom in of the energy bands close to one of the Dirac points, showing the linear dispersion of graphene. Adapted from [11].

graphene is ampibolar [13], i.e. majority charge carriers can be continuously "tuned" between electrons and holes by applying an electric field by a suitable gate [10]. Gate bias shifts the Fermi level E_F either above or below the Dirac point, resulting in electron or hole transport respectively [13] (Figure 2.3). As the Fermi level is shifted by the gate, the density of states (DOS) and therefore the carrier density are changed [13]. The Fermi energy can be shifted away from the Dirac point, either by applying a gate voltage or by doping.

The sheet resistance of graphene is determined by the response of electrons to the electric fields. Theoretically, it reach value about few hundreds of Ω/sq, but can be highly increased (up to 10^5 Ω/sq) in presence of defects: interflake junction or grain boundaries act as tunnelling barriers and obstruct the movement of the electrons [15].

The sheet resistance is related to the density of state of the material, thus, since the DOS of graphene can be tuned by doping, the sheet resistance can slightly change depending on the environment [15].

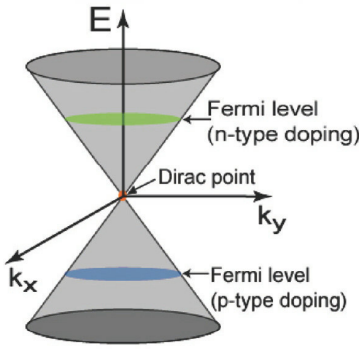

Figure 2.3: Approximation of the low energy bandstructure as two cones touching at the Dirac point. The position of the Fermi level determines the nature of the doping and the transport carrier. Adapted from [13].

In technology, graphene is part of a more complex structure and is used under conditions that are dictated by the application. Under such realistic conditions, electronic transport is subject to a variety of scattering interactions [16]. Graphene field effect transistors (FET) are currently among the most renowned graphene devices for electronic. A FET is a three terminals device, with two of them (source and drain) separated by a channel and the third one (called gate) under it and insulated with a thin dielectric layer [17].

The operation of graphene devices is not only dependent on the electrical properties of the graphene material used, but is also strongly affected by what happens in other parts of the device. Specifically, carriers have to be injected into a graphene channel and then collected through metal contacts. These contacts generate potential energy barriers that have to be circumvented and can profoundly affect the performance of graphene devices leading, for example, to the doping of graphene underneath the metal [13]. Enhanced carrier injection is experimentally achieved in graphene devices in Ref. [18] by forming cuts in the graphene within the contact regions. These cuts facilitate bonding between the contact metal and carbon atoms at the graphene cut edges, maximizing the current injection.

The electronic structure and properties of multi-layer graphene depend on the number of layers and their stacking. The most stable stacking in graphite is the so-called ABA stacking, or Bernal stacking, where half of

the atoms of a given layer are directly over those of the layer below and the other half are over the centres of the hexagons. In an AB bilayer the rather strong interaction between the layers forms a unique band structure with a four atom unit cell [13].

2.1.2 Optical properties

Light transmittance through free-standing graphene can be derived using the Fresnel equations for a thin film [19].

Because of its linear energy spectrum, single monolayer graphene transmits $\sim$ 97% of the incident light and absorbs $\sim$ 2.3%, independent of its wavelength from $\sim$ 300 to 2500 nm. The reflectivity of one layer, on the other hand, is $< 0.1\%$ in the visible region, rising to $\sim$ 2% for 10 layers [20]. Furthermore, the absorbance of multi-layer, up to 6 sheets, at energies above $\sim 0.5\,eV$ is additive, thus the optical contrast can be useful to distinguish the number of layers [20].

Given its thickness, graphene exhibits a strong light absorption. For comparison, a film of InGaAs would require a thickness of 20 nm to absorb the same amount of light (at 1.55 μm) [13].

Graphene is easily optically identified, despite its atomic thickness, if placed onto appropriate substrates, consisting of a spacer (typically SiO_2) and a reflecting surface (typically Si) [20, 21]. By adjusting either the spacer thickness or the light wavelength it is possible to maximize the optical contrast [20, 21]. The contrast is the result of light interference in the trilayer structure formed by graphene, spacer and reflecting surface and linearly scales with the number of layers [20, 21]. A better explanation of the reasons than lead to this phenomena will be given in section 3.2.

2.1.3 Mechanical properties

Graphene is considered one of the strongest and stiffest material known, it can sustain strain up to 10% without plastic deformations [22].

Monolayer graphene is a true 2D material, so its strain energy density is normalized by the area of the graphene sheet rather than by the volume. Therefore, its behaviour under tensile loading is properly described by a

2D breaking stress σ^{2D} and elastic constants E^{2D} with units of force/length [23].

Elastic stiffness for monolayer graphene E^{2D} of $340 \pm 50\, N/m$ and intrinsic breaking strength σ_{int}^{2D} of $42 \pm 4\, N/m$ have been measured and simulated in Ref. [23]. These correspond to a Young's modulus $E = 1.0 \pm 0.1\ TPa$, assuming an effective graphene thickness of $0.335\ nm$ and to an intrinsic breaking stress $\sigma_{int} = 130 \pm 10\, GPa$ at a strain of $\epsilon_{int} = 0.25$. These values are very close to the ones obtained theoretically by Griffith in his studies about the breaking strength of brittle materials in which $\sigma_{int} \sim E/9$ [23].

Besides its extraordinary strength, graphene also exhibits unusual mechanical properties. Unlikely other materials, graphene shrinks with increasing T at all values of T [24]. Also, graphene exhibits simultaneously high pliability (folds and pleats are commonly observed) and brittleness (it fractures like glass at high strains) [24].

Equally unprecedented is the observation that the one atom thick film is impermeable to gases, including helium [24].

The intrinsic strength serves as a benchmark for structural and mechanical applications, although the strength of macroscopic graphitic materials is still limited by the presence of defects and grain boundaries [23].

2.1.4 Chemical properties

Graphene has a wide open double-sided surface that can undergo a broad class of organic reactions analogous to unsaturated systems in organic molecules. For chemists, graphene is an analogue of a giant aromatic "polymolecule" possessing high electrical conductivity, mechanical strength and optical absorption properties [25].

Graphene can adsorb and desorb various atoms and molecules (for example, NO_2 , NH_3 , K, and OH). Weakly attached adsorbates often act as donors or acceptors and lead to changes mostly in the carrier concentration, leaving graphene highly conductive. Thermal annealing or chemical treatment allows the reduction of graphene to its original state with relatively few defects left behind [24].

The surface chemistry of graphene can be also modified by chemical functionalization and it can be used to tailor the chemical specificity and the electronic properties of the surface [4].

The functionalization of graphene can be performed by covalent and non-covalent modification techniques [8].

Covalent functionalization involves the acid oxidation of graphene or graphite followed by a reduction process. The oxidation imparts oxygenated species like carboxyl, epoxy and hydroxyl on the material, generating graphene or graphite oxide (GO) [25].

The presence of oxygenated groups on the basal plane of graphene disrupts the π-conjugation, thus GO is insulating. Also after reduction the graphene sheet exhibits resistivity several times larger than that of unprocessed graphite [25]. In addition, GO is a non-stoichiometric material because the density of oxygen groups cannot be precisely controlled, which means that functionalization chemistry based on coupling chemistry to the oxygenated groups will inevitably lead to non-stoichiometric functionalization [25].

The non-covalent interactions are based on van der Waals forces or π-π stacking of aromatic molecules on the graphene plane. The advantage is that this does not disrupt the extended π conjugation on the graphene surface, unlike covalent functionalization which creates defects on the graphene sheet [25].

The covalent modification of graphene can be achieved in different ways among which nucleophilic substitution, electrophilic addition and condensation [8]. The structural alteration can take place at the end of the sheets and/or on the surface. Surface functionalization is associated with rehybridization of one or more sp_2 carbon atoms of the carbon network into the sp_3 configuration accompanied by simultaneous loss of electronic conjugation [8].

The main reactive sites in the nucleophilic substitution reaction are the epoxy groups of GO. An amine ($-NH_2$) functionality, for example, bearing a lone pair of electrons, attacks the epoxy groups of the GO. In comparison to other methods, nucleophilic substitution occurs very easily, also at room temperature and in an aqueous medium. Instead, electrophilic substitution reactions with graphene involve the displacement of a hydrogen atom by an electrophile [8].

A condensation reaction is a chemical reaction in which two molecules (functional groups) combine to form one single molecule with a loss of entropy. In the case of graphene, condensation occurs with isocyanate,

diisocyanate, and amine compounds through the formation of amides and carbamate ester linkages [8].

In order to obtain functionalized graphene from functionalized GO, reduction is an essential step. All reducing agents that are generally used for the reduction of organic ketones, carboxylic acids, and epoxy functional groups can be used in the reduction of pure GO or functionalized GO. A lot a these chemicals are hazardous to human health and the environment, thus some alternative methods, as acetic acid and HCl reduction, have been recently proposed [8].

Geometrically strained regions in the graphene lattice are areas of preferential reactivity because of the displacement of electron density above the plane of the ring. Engineering strain in a periodic manner on the surface lattice to control reactivity is a potential way of achieving stoichiometric functionalization of graphene [25]

Due to the two-dimensional nature of graphene sheets, the edge regions play an important role in the electronic structure of the molecules. Edges are preferred sites for functionalization, due to their higher reactivity with respect to the basal plane. In particular, they can manifest as either zig-zag tracks or arm-chair tracks. In the zig-zag edges, the attainment of aromatic sextets is frustrated in the majority of the rings, hence such a structure is thermodynamically unstable compared to the arm-chair edges, thus it can be expected that the zig-zag edges will display higher reactivity as compared to the arm-chair edges [25].

2.2 Production

Several production techniques are available for the fabrication of graphene, as shown in Figure 2.4. The most currently used are Micromechanical cleavage (MC), Chemical vapour deposition (CVD) and Liquid phase exfoliation.

2.2.1 Micromechanical cleavage

Micromechanical cleavage (MC) is based on the splitting of strongly layered materials into individual atomic planes by means of adhesive tape. MC was the method used by Novoselov *et al.* to isolate single layer graphene

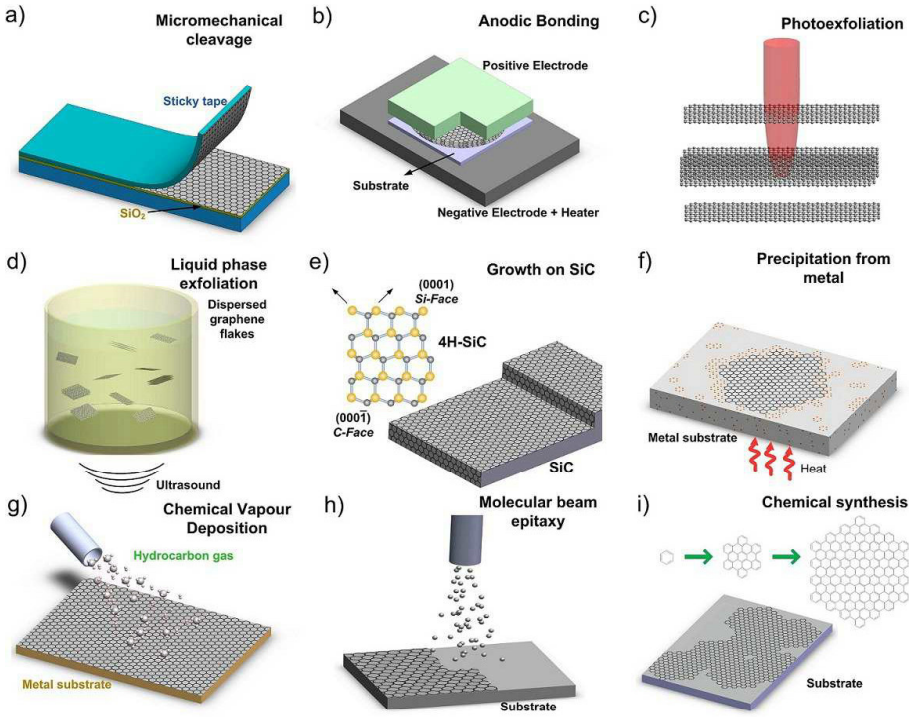

Figure 2.4: Schematic illustration of the main graphene production techniques. a) Micromechanical cleavage. b) Anodic bonding. c) Photoexfoliation. d) Liquid phase exfoliation. e) Growth on SiC. Gold and grey spheres represent Si and C atoms, respectively. At elevated T, Si atoms evaporate (arrows), leaving a carbon-rich surface that forms graphene sheets. f) Segregation/precipitation from carbon containing metal substrate. g) Chemical vapour deposition. h) Molecular Beam epitaxy. i) Chemical synthesis using benzene as building block. Adapted from [3].

and investigate their electronic properties [26].

Natural or highly oriented pyrolitic graphite (HOPG) is firstly repetitively cleaved in order to expose a flat and clean surface. Then another tape is used to extract part of the graphite from the bulk and obtain a thin, flat graphite flake. This flake is then cleaved several times in order to uniformly distribute graphite on the tape. Then an oxidized silicon substrate is placed on the tape, bringing its flat surface in contact with the graphite. The thickness of the oxide is chosen to ensure good optical contrast, therefore either 100 or 300 nm are used [20, 21]. When the tape is removed, graphitic flakes are transferred onto the substrate because of Van

der Walls interactions.

MC is now optimized to yield high quality layers, and samples up to about $1\,mm$ have been obtained [24]. The size of the extracted layers is limited by the single crystal grains in the starting graphite. Despite low yield, samples produced by MC are still the best in terms of structural and electronic quality, providing defect-free single crystals [3] and does not require complex or expensive equipment. Therefore MC is still and is like to remain the method of choice to investigate new physics and proof-of-concept devices [3] but is not good for mass production.

2.2.2 Chemical vapour deposition

Although micromechanical exfoliation of graphite still gives the best samples in terms of purity, defects, mobility and optoelectronic properties [26], large-scale assembly is needed for the widespread application of this material.

Chemical vapour deposition (CVD) is a process widely used in the semiconductor industry to grow high quality single layer graphene with large area [27]. Graphene monolayer film is grown on various substrates by feeding a source gas (containing carbon atoms) at a suitable temperature. The process parameters such as temperature, pressure and source gas flow, have a key role in the resulting structure of the monolayer film in terms of thickness (to obtain from one layer to few layers) and defects. There are different types of CVD, the most used for graphene are thermal and plasma enhanced (PECVD) [3].

The growth of thin graphitic films on metals has been studied since the sixties primarily targeting the understanding of the catalytic and thermionic activity of the metal surfaces in the presence of carbon [3].

Carbide formation is one of the main obstruction in the graphene growth, acting as competitive process. Metals like Ti, Ta, Hf, Zr and Si, form thermally stable carbides thus are not ideal as grown substrate, moreover, all have a large ($> 20\%$) lattice mismatch with graphene [3]. Non-carbide forming metals like Cu, Ni, Au, Pt and Ir are preferred [28].

One of the first investigation in the growth of graphitic layers was performed on Co, Pt and Ni by [29] in 1974. They observed single layer graphene by Auger analysis at $T > 1000\,K$, followed by graphite formation

upon cooling. During high T annealing, carbon diffuses into the metal until it reaches the solubility limit (few atomic percent). Upon cooling, carbon precipitates forming first graphene, then graphite [29]. The graphite film thickness depend on many parameters among which the type of metal, the solubility of carbon in that metal, the T at which the carbon is introduced, the thickness of the metal and the cooling rate [29].

After the discovery of the many interesting properties of graphene in 2004, the focus on the growth of single layer sheets increased.

Low pressure chemical vapour deposition (LPCVD) on Ir single crystals using an ethylene precursor was found to yield graphene structurally coherent. Because of the difficulties in transfer and the high cost of the Ir, attention shifted to Ni [30] and Co [31], metals compatible with silicon processing and less expensive than Ir. However, growth on these metals involves carbon precipitation and yields few layers graphene [30, 31, 32].

There are two different mechanisms for the formation of graphene depending on the metal substrates used. For metals with relatively high carbon solubility, such as nickel ($\sim$ 1.3 atom% at 1000 °C), the dissolved carbon atoms at high temperature can precipitate out to form multiple layer graphitic films on the metal surface upon cooling, as a result of carbon supersaturation in the solid [30, 32].

On the other hand, low carbon solubility metals (e.g. copper, platinum) show predominately uniform monolayer graphene growth due to a self-limiting effect [28].

Actually, if the graphene is not directly produced on the metal surface by the reaction and deposition of the precursor at the growth T, but grows by carbon segregation from the metal bulk, as in the case of Ni, the process cannot be completely considered a CVD growth [3].

The first real CVD growth of uniform, large area ($\sim\ cm^2$) single layer graphene on a metal surface was achieved on polycrystalline Cu foils, exploiting thermal catalytic decomposition of methane and low carbon solubility [32]. Cu substrate catalyzes the cracking of the carbon source, giving rise to a self-limited process. Growth mostly ceases as soon as the Cu surface is fully covered with graphene [28, 33].

Growth of graphene on Cu was then scaled up by increasing the Cu foil

size (30 inches) [34], trying to understand the growth mechanism and to find the best growing conditions to create a almost defect-free large area sheet with high electronical performances [35]. Films with $\mu \sim 7350\, cm^2/Vs$ at $6\ K$ were produced by [34], and large grain graphene ($\sim\ 20 - 500\ \mu m$) with μ ranging from $\sim\ 16,400$ to $\sim\ 25,000\ cm^2/Vs$ at room temperature after transfer to SiO_2 was reported in [36, 37].

The current understanding of the growth mechanism is as follows. Carbon atoms, after decomposition from hydrocarbons, nucleate on Cu, and the nuclei grow into large domains [37, 35]. The nuclei density is principally a function of T and pressure and, at low precursor pressure ($mTorr$) and $T > 1000\ ^\circ C$, very large single crystal domains, (up to $\sim 0.5\, mm$) are observed [37, 35].

The layer grown by CVD usually shows several domains, with different orientation separated by grain boundaries. The dimension of the domains depends mainly on the growth conditions.

Graphene preferentially nucleates along linear axes, which could be due to the initial graphene nucleation occurring more frequently at step edges, folds, or other imperfections in the copper foil that are linear in character [38].

The electronic properties of graphene are highly influenced by the final structure of the layer. An higher number of grain boundary lead to a lower mobility because the movement of the electrons is obstructed by the presence of defects in the theoretical honeycomb lattice [39].

There are some difficulties when growing graphene on most metal substrates, especially Cu, because of the difference in thermal expansion coefficient between Cu and graphene, of about an order of magnitude. The thermal mismatch gives rise to a significant wrinkle density upon cooling [33]. These wrinkles are defective, and may also cause significant device degradation through defect scattering [37].

Also multi-layer graphene films with specific stacking orders have attracted enormous attention due to their tunable electronic structures [40]. Consequently, method to develop growth procedures for multi-layer graphene with controlled thickness that are compatible with manufacture technologies, started to be studied.

Ref. [41] demonstrated that the self-limiting effect of graphene growth on Cu foil can be broken by using high H_2:CH_4 ratio in a low-pressure CVD process to enable the continued growth of bilayer graphene.

Methods to produce large area graphene films with precise thickness control has been demonstrated in few works [42, 43, 41, 44, 45, 46, 38].

The number of layers was controlled precisely by regulating the flow ratio of CH_4 and H_2 , the reaction pressure, the temperature and the reaction time [42].

Graphene with 1-7 layers have been synthesized on Cu substrates by Ref. [42]. Although the detail mechanism of formation remains unclear, the number of layers of graphene should be determined by the diffusion rate of carbon atoms, which is mainly affected by the concentration of the available carbon atoms on the Cu surface.

As the growth pressure increases, thicker graphene films grow on the Cu surfaces. Specifically, bi, tri, and tetra layers graphene films have been grown by Ref. [43] at CH_4 pressure of 3.6, 5.2, and 9.6 *Torr*, respectively. In general, low pressure is favourable to the formation of few layers (1-3) of graphene whereas atmosphere pressure is suitable for the formation of multi-layer (3-7) [42].

Graphene grows from multiple growth centres and the crystals subsequently merge seamlessly, as indicates the polycrystalline nature of the films usually grown. In Ref. [43] the graphene thickness is defined at the initial stage. The islands maintain their thickness and stacking order while the edges propagate laterally on the Cu surface. Multi-layer graphene seeds form when carbon atoms are supersaturated in the surface of the Cu [43].

In the other hand, in Ref. [38] few layers graphene consisting of approximately 5-10 layers in the central region and thinning out toward the edges of the domain have been grown. The central part of the domain contains more layers than the outer regions. This indicates that the number of graphene layers diminishes closer to the graphene grain boundary in a step pyramid type structure [38].

Graphene with controllable number of layers has also been reported on Ni-Cu alloy substrates by tuning of the growth conditions, but the uniformity of the bilayer graphene was limited due to the non uniform

alloy composition [47].

2.2.3 Liquid phase exfoliation

Liquid phase exfoliation (LPE) consists in the exfoliation of graphite in a liquid environment exploiting ultrasound [3]. The exfoliation is controlled by hydrodynamic shear-forces, associated with cavitation, i.e. the formation, growth, and collapse of bubbles or voids in liquids due to pressure fluctuations [48]. After exfoliation, the solvent-graphene interaction needs to balance the inter-sheet attractive forces. Solvents ideal to disperse graphene are those that minimize the interfacial tension between the liquid and graphene flakes, i.e. the force that minimizes the area of the surfaces in contact [3].

The most suitable solvents for the dispersion of graphene are those with surface tension in the region of $\sim 50\ mJ/m^2$ [49, 50]. Water's surface tension ($\sim 72\ mN/m$) is too high for the dispersion of graphene and graphite [3, 50]. Therefore linear chain surfactancts or polymers are required to prevent re-aggregation of exfoliated flakes.

The sonication process produces flakes of different thickness. In order to obtain dispersions enriched in monolayers, a "purification" process is required. This is usually achieved by ultracentrifugation either in a uniform medium (sedimentation based-separation, SBS) or in a density gradient medium (density gradient ultracentrifugation, DGU) [3]. High concentration of monolayers (up to $\sim$ 70%) with flake lateral size of $\sim 30-200\ nm$, or lower concentration ($\sim$ 33%) but larger flake size ($\sim 1\ \mu m$) are achieved with different solvent [51, 49].

LPE is cheap and easily scalable, and does not require expensive growth substrates. It is an ideal mean to produce inks, thin films, and composites [52]. The resulting material can be deposited on different substrates (rigid and flexible) by drop and dip casting, rod coating, spray coating and inkjet printing [3, 49, 48]. Therefore LPE is the method of choice to produce inexpensive large conductive films consisting of a percolating path of small flakes [3].

2.3 Applications

Graphene properties such as high carrier mobility, broadband light absorption, mechanical strength, high conductivities and impermeability to gases make it highly attractive for numerous applications. For example the combination of transparency, conductivity and elasticity will find use in flexible electronics, whereas transparency, impermeability and conductivity will find application in transparent protective coatings, barrier films, sensors and many others.

2.3.1 Electronics

Transparent conductive coatings are widely used in electronic products such as touch screen displays and e-paper and require a low sheet resistance with high transmittance (of over 90%) depending on the specific application. Graphene meets the electrical and optical requirements and an excellent transmittance of 97.7% perlayer, although the traditionally used indium tin oxide (ITO) still demonstrates slightly better characteristics, with a sheet resistance less than $100\,\Omega/sq$ and an optical transparency of $\sim 90\%$ [13].

Graphene also has outstanding mechanical flexibility and chemical durability, very important characteristics for flexible electronic devices, in which ITO usually fails. Moreover, the fracture strain of graphene is ten times higher than that of ITO, meaning that it could also successfully be applied to bendable and rollable devices also if the contact resistance between the graphene electrode and the metal line of the driving circuitry is still a problem [2].

Graphene based transistors (GFET) have developed rapidly and are now considered an option for post-silicon electronics.

The basic of the "switching" in GFET is the tuning of the density of state applying a gate voltage. However, unlike transistors made of conventional semiconductors with a band gap, a GFET does not turn off completely, even though the DOS is zero at the neutrality point. A residual conductivity is always present, thus this material is not suitable for logic application in which on/off ratio of at least 10^6 is required.

The chemical functionalization of graphene offers an alternative approach to the control of its electronic properties. The hydrogenation of

graphene, which involves the change of electronic structure from sp_2 to sp_3, results in a conversion from a metallic graphene to an insulator [25].

If graphene is covalently bonded to electron-withdrawing oxygen functionalities, p-doping can be induced. Similarly, if it is functionalized by electron-donating nitrogen functionalities, n-doping can be achieved. With precise control of the interface between p-doped and n-doped graphene regions, it is possible to selectively engineer a graphene p-n junction by chemical doping [25].

Graphene has been considered and intensively researched also for high frequency transistor applications [53, 2]. However, it has to compete against more mature technologies such as compound semiconductors (III-V materials).

In the low cost sector liquid-phase exfoliation produces such graphene coatings without the use of expensive vacuum technology. Although the resistance of these films is on the high side, they still perform well enough for smart windows, solar cells and some touch screen applications [2].

Finally graphene's electrical and thermal conductivities as well as its excellent barrier properties might push this material towards being used as interconnects as well as for thermal dissipation in integrated circuits [2].

2.3.2 Photonics

Conversion of light into electrical signals is essential for a variety of applications, ranging from imaging to high-speed communication, medical diagnostic and photovoltaics.

Graphene strongly interacts with light and is therefore an excellent candidate for several photonic and optoelectronic applications. Graphenes unique gapless electronic bandstructure allows charge carrier generation upon light absorption over a very wide energy spectrum, including ultraviolet, visible, infrared and THz [13, 2].

Graphene shows remarkable light absorption, with each layer absorbing 2.3% of the incoming light, exhibiting an absorption coefficient one to three orders of magnitude higher than technologically relevant materials such as InGaAs, GaAs or Ge [13].

Furthermore, graphene optical properties can be tuned by electrostatic doping. Several mechanisms determine the generation of free charge carriers upon light interaction, including photovoltaic, photo-thermoelectric, bolometric effects and plasma wave-assisted absorption. This in turn allows the realization of a variety of photodetectors, able to respond to light ranging from deep UV to far IR (THz) [54].

Graphene detectors offer different advantages over current technologies: their response is extremely fast, graphene allows tunable spectral selectivity and graphene field-effect transistors allow room-temperature detection of THz radiation, at the moment lacking of fast solid state detectors.

Given that graphene absorbs 2.3% of the light different strategies have been used to improve the sensitivity of graphene-based detectors. These include the integration of graphene into optical microcavities, planar photonic crystal cavities and optical waveguides [54].

Schottky junctions formed between graphene and semiconductors have also been successfully applied (under reverse bias) as photodetectors, where the semiconductor absorbs the light and graphene acts as optically transparent charge carrier collector. Hybrid systems, consisting of an absorbing layer (such as colloidal quantum dots) deposited on graphene, have shown very efficient conversion on light into electrical signals [54].

Ultrafast passively mode-locked lasers have been used for various applications. They usually use saturable absorbers to cause intensity modulation by selectively transmitting high-intensity light only. Compared with the widely used semiconductor saturable absorbers, graphene absorbs a significant amount of photons per unit thickness and therefore reaches saturation at a lower intensity over a wide spectral range [2].

Finally different studies demonstrate the possibility to use graphene as THz genetarots. Using a pulsed excitation of single-layer graphene or using multi-layer graphite under a femtosecond laser pulse field it is possible to generate carriers that will be accelerated to generate the THz wave. THz generators can be used in various applications such as medical imaging, chemical sensors, and security devices [2].

2.3.3 Composite materials, paints and coating

Graphene-based paints can be used for conductive ink, antistatic, electromagnetic interference shielding, and gas barrier applications. Graphene is

highly inert, and so can also act as a corrosion barrier against water and oxygen diffusion. Given that it can be grown directly on the surface of different metals, it could form a protective conformal layer, also on complex surfaces [2].

The mechanical, chemical, electronic and barrier properties of graphene along with its high aspect ratio make graphene attractive also for applications in composite materials [23]. Graphene can contribute gas and moisture barrier properties, electromagnetic shielding, electrical and thermal conductivity, and a strain monitoring capability to the surrounding polymer matrix. As an additive to a composite matrix polymer it might increase the operating temperature level of composites, reduce moisture uptake, induce antistatic behaviour, give lightning strike protection and improve composite compressive strength [2].

2.3.4 Graphene for sensors and bioapplications

Graphene, being a two-dimensional fabric and a surface without bulk, can be extremely sensitive to the environment [24]. His resistivity, in presence of different chemical species, can considerably change. Thus, graphene is ideal for sensing applications.

The major advantage of graphene sensors is their multi-functionality. A single device can be used in multidimensional measurements: from strain and gas environment to pressure and magnetic field [2].

Graphene has a number of properties which make it potentially promising also for bioapplications. Its large surface area, chemical purity and the possibility of functionalization provide opportunities for drug delivery and might lead to fast and ultrasensitive measurement devices, capable of detecting a wide range of biological molecules.

The interaction between the functional groups of biomolecules and pristine graphene is unfavorable due to the absence of hydrophilic groups. On the contrary, functionalized graphene interacts very easily with the biomolecules compared to pure graphene [8]

One of the most promising applications of functionalized graphene is the fabrication of sensors to diagnose diseases. These sensors are based upon the large surface area of graphene and the fact that molecules are sensitive to particular disease indicators and can attach to the carbon atoms

in graphene. It has been found that the functionalized graphene-based biosensors can successfully detect glucose, NADH, cholesterol, hydrogen peroxide, and other molecules [8].

Its unique mechanical properties suggest also tissue engineering applications and regenerative medicine [2].

The biocompatibility of graphene with microorganisms and living cells need to be explored. Several research efforts have been focused to analyse the biocompatibility of GO and graphene with microorganisms [8].

Most of the applications of graphene in electronic devices rely on lateral conduction of carriers in high quality two-dimensional sheets. Different kinds of graphene-based materials derived from various preparation methods rather than the pristine graphene have been widely used in electrochemical biosensors, because it is difficult to make practical electrochemical electrodes from single-layer, high-purity graphene. The mostly used graphene-based materials, typically GO, are available in bulk quantities. These chemically modified graphene contain certain amounts of defects and oxygen-containing functional groups, which are deleterious to the two-dimensional electrical conductivity. However, it is well-known that heterogeneous electron transfer in the electrochemistry of carbon nanomaterials occurs at the edge planes and defects, and is sluggish at the basal plane of graphene sheets. Thus, the structural defects of chemically modified graphene can be beneficial for electrochemistry, as these are likely to be the major sites for rapid heterogeneous electron transfer. Furthermore, the presence of functional groups facilitates the functionalization with various biomolecules for biorecognition events. The combination of these mentioned excellent properties with high surface to volume ratio and easy availability enables graphene as an attractive transducer material for electrochemical biosensors [55].

Chapter 3

Procedure and Instrumentations

This chapter reports the experimental procedures used to produce and characterize single and multi-layer graphene grown by thermal CVD. Starting from the known conditions (temperature, pressure, growth time and gases flow ratio) used for the growth of polycrystalline single layer films, this work investigates the tuning of such parameters in order to engineer graphene surface properties, by growing a two layers structures. Graphene layers are grown onto copper substrates at high temperature and subsequently transferred onto oxidized silicon wafers by means of a sacrificial polymer layer.

Graphene layers are characterized by optical microscopy and Raman spectroscopy to assess uniformity, structural and electronic properties and process residuals.

The growing parameters are optimized to achieve a double layer structure, consisting of a bottom continuous layers (ensuring high conductivity) and a top discontinuous layer (closely packed small islands).

Surface-optimized graphene along with "standard" single layer graphene are integrated into field effect transistors in order to further investigate the material in terms of conductivity and charge carrier mobility.

Metal electrodes are fabricated by electron beam lithography patterning, followed by thermal evaporation and lift-off. Channels are subsequently defined by another electron beam lithography and plasma etching.

Output and trans-characteristics of optimized and standard graphene

transistors are acquired and sheet resistance, charge carrier mobility and contact resistance are identified for a large number of devices.

3.1 CVD growth

Graphene is grown by thermal CVD using a Graphene Square CVD reactor. This consist of a sealed chamber with precise control of temperature, pressure and flow rate of gas species used for the process. Under specific conditions of temperature, pressure and flow rate gas molecules are catalytically decomposed on a copper substrate and carbon atoms are deposited on the surface. Different conditions and growth time lead to the deposition of materials with different properties. The gases used for graphene deposition are methane (CH_4) as source of carbon atoms and hydrogen (H_2), in an inert atmosphere.

The substrate used in this work is a 25 μm thick copper foil with high purity (99,8%). It was chosen for the growth of single layer graphene, because it combines catalytic activity and low carbon solubility, yielding to growth self-limited to single layer [28].

The machine used is shown in Figure 3.1. It contains a quartz chamber where the substrate is inserted placed in a transparent tube and the gases flow under the action of a pump. The electric heater (blue device in Figure 3.1) heats up the chamber by means of resistors that emit radiant energy by Joule effect. The peculiarity of this furnace is the fact that the heater can be moved sideways to allow a fast cooling down, important in the growth on single layer graphene.

Graphene growth is a catalytic process, involving hydrocarbon decomposition and surface diffusion. Due to strong C-H bonds in methane molecule (440 kJ/mole), its thermal (non-catalytic) decomposition would occur at very high temperatures (1200 °C) [56]. At a constant temperature, the methane decomposition rate on an ideal flat copper surface is uniform. However, the sheet used in this process is not monocrystalline. It shows a high density of atomic steps and grain boundaries even after annealing. These sites have much higher chemical activation energy than the flat regions of the surface, thus they represent nucleation centres and the decomposition rate of hydrocarbons on them is higher. This phenomenon implies that the graphene film tends to have lower number of layers away

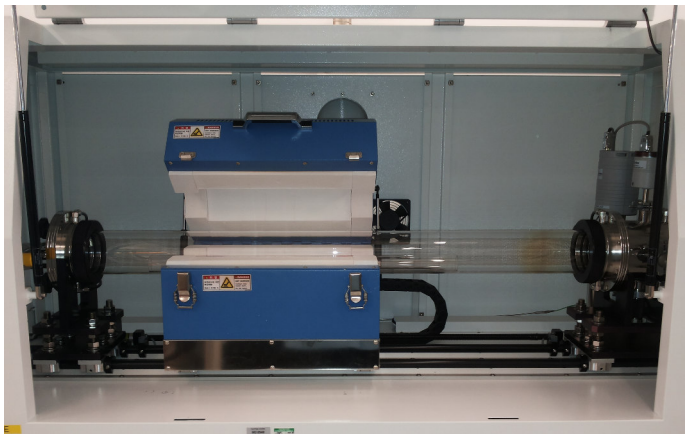

Figure 3.1: CVD furnace. It is visible a quartz chamber and a blue device. In the chamber the gases flow under the action of a pump. The blue device heat up the chamber and can be moved sideways.

from the nucleation centres. Furthermore, since the growth starts from different copper site, graphene grows in grain with different orientations [56].

The graphene growth rate and number of layers are determined by the diffusion rate of carbon atoms which, in turn, is influenced by the temperature and the density of carbon atoms on the surface. High diffusion rate and high carbon concentration result in few layer or multi-layer graphene. Therefore, to control the number of graphene layers and growth rate, the concentration of the carbon atoms on the surface has to be controlled with high accuracy. Since this parameter depends on the partial pressure of the hydrocarbon gas at a given temperature, controlling it is a critical factor for the growth of graphene [56].

The surface treatment of the foil is another critical parameter that affects the growth of graphene. Before starting the process, an accurate cleaning of the copper surface is necessary to increase the process reproducibility.

3.1.1 Growth steps

The growth procedure consists in these main steps:

- The Cu substrate has to be cut with a cutter, trying to obtain a wrinkle-free surface. The smoother is the surface, the higher is the quality of

the grown graphene. The sample dimension is limited by the quartz tube diameter. The two surfaces of the Cu sheets do not have the same properties, due to a pre-treatment performed by the producing company. For this reason, it is important the sheet orientation during the growth process, and thus the samples cannot be flipped.

- The substrate is cleaned by acetic acid. The immersion of the Cu foil in acetic acid for 10 minute removes the upper oxide layer and other impurities on the surface. After that, the sample is washed in de-ionized water and blow-dried using a nitrogen flow.

- The Cu sheet is inserted in a quartz transparent tube of $3\,cm$ internal diameter (Figure 3.2). The Cu foil can be positioned in the tube either flat or rolled. In the second case with the pre-treated surface on the inner part.

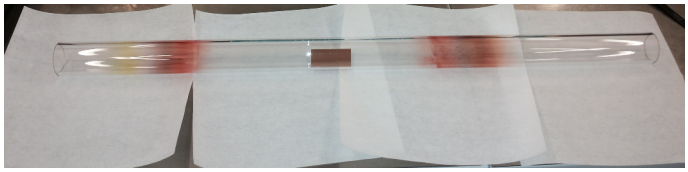

Figure 3.2: Quartz tube with copper sample inside. The pre-treated surface is the upper part of the sample.

- The chamber is cleaned before inserting the tube. This procedure require a flow of hydrogen and methane at low pressure and room temperature.

- The chamber is vented and the tube is loaded in it. The tube has to be placed on a side of the chamber with the heater placed exactly above it. This configuration leaves space to move the heater from the tube if a fast cooling down is required.

- The pump is activated and, once the desired pressure has been reached, the temperature cycle is set by programming a Yokogawa controller.
  Hydrogen (and argon when necessary) is flowed through the chamber according the desired recipe and the heat process starts. From room temperature the chamber in heated to a temperature of 1000 $^{\circ}C$ and

then this value is kept constant until the end of the process. The total amount of time depend on the type of layer that has to be grown.

The first part of the growth is indicated as "**heating**" and consists in the slow heating ($\sim$ 10 $^{\circ}C/min$) of the chamber up to the desired temperature avoiding thermal shocks that might damage the chamber. Usually it take at least one hour.

The second part is indicated as "**annealing**" and it is performed at high and constant temperature. The main reasons to perform an annealing are:

- Any possible oxide layer is removed from the copper surface, due to the reducing activity of the hydrogen.
- Copper atoms sublimate, thus the surface become smoother.
- Copper grains grow, thus the number of nucleation site decrease increasing the homogeneity in the graphene growth process.

Figure 3.3 shows the same Cu foil before and after 30 minutes annealing at 1000 $^{\circ}C$.

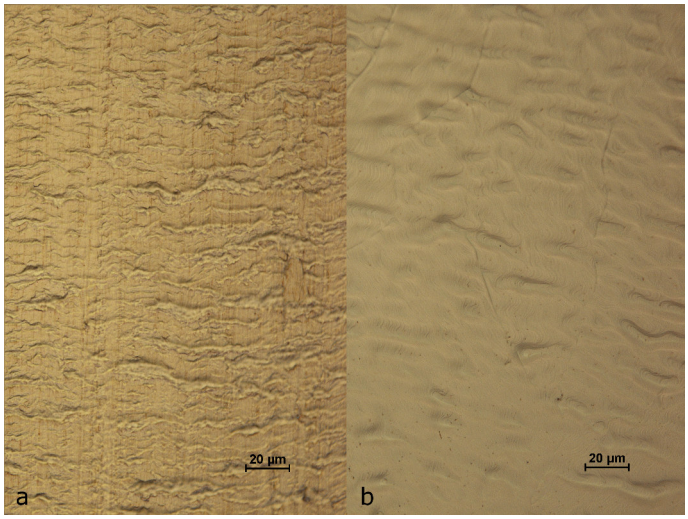

Figure 3.3: Copper foils. a) Optical image of the copper foil before annealing. b) Optical image of the copper foil after a growth process with annealing of 30 minutes at 1000 $^{\circ}C$.

The third part is the "**growth**" of the graphene layer. Once the annealing is complete, methane is added to the flow without changing the temper-

ature in the chamber. The methane in contact with the copper substrate dissociates, bringing to the growth of a graphene layer.

The last part is the "**cooling down**". It can be performed as fast as possible (quenching process), or slowly, depending on the recipe. In the first case the heater has to be shifted sideway far from the sample. In the second case the heater is switched off but is kept on the sample, so the temperature drop is smoother.

The fast cooling down usually is performed when a single layer graphene is required. Although copper has low carbon solubility, some atoms can diffuse from the bulk to the surface during the cooling down creating imperfections in the single graphene layer. An abrupt temperature drop does not allow the carbon to diffuse through the substrate and thus single layer is preserved.

A graphical representation of the all process is shown in Figure 3.4.

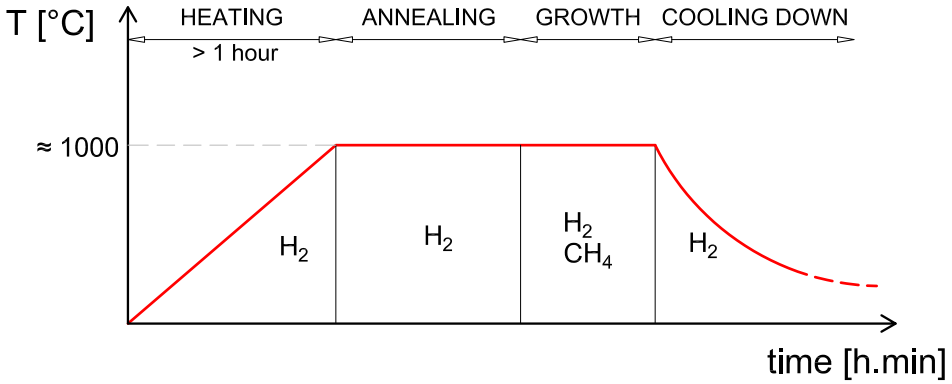

Figure 3.4: Standard CVD process: the chamber is heated up to $900 - 1000\,°C$, it is kept at constant temperature during the annealing and the growth and then it is cooled down.

3.2 Optical analysis

One of the key-reason that triggered graphene research is the ease of optically identifying layers even only one atom thick. Monolayers cannot be seen in a optical microscope on most substrates (like copper) but they become visible if placed onto appropriate substrates, usually silicon with a

carefully chosen thickness of thermally grown SiO_2, typically $300\,nm$ [20].

The origin of the contrast which allows detection of a single atomic layer lies in an interference-like process.

The image contrast δ is defined as the difference between substrate and sample intensity, normalized to the substrate intensity [20].

When the light impinges on a multilayer, multiple reflections take place. Thus, the detected signal I results from the superposition of the reflected field from the air-graphene E_G, graphene-SiO_2 E_{SiO_2} and SiO_2-Si interfaces E_{Si} [20].

The field at the detector is dominated by two contributions: the reflection by the graphene layer and the reflection from the Si after transmission through graphene and after passing through the SiO_2 layer twice. Thus, the intensity at the detector can be approximated as:

$$I \approx |E_G + E_{Si}|^2 = |E_G|^2 + |E_{Si}|^2 + 2|E_G||E_{Si}|cos\phi \tag{3.1}$$

where ϕ is the total phase difference that includes the phase change due to the optical path length of the oxide.

Assuming the field reflected from graphene to be very small, $|E_G|^2 = 0$, the image contrast δ results from interference with the strong field reflected by the silicon:

$$\delta = \frac{I_{Si} - I}{I_{Si}} \approx \frac{-2|E_G|cos\phi}{|E_{Si}} \tag{3.2}$$

Eq. 3.2 shows that the main role of the SiO_2 is to act as a spacer: the contrast is defined by the phase variation of the light reflected by the Si. Thus, the contrast for a given wavelength can be tailored by adjusting the spacer thickness or its refractive index [20].

The contrast strongly depends on the number of layers. For a few layers (< 6), the samples behave as a superposition of single sheets, while for thicker samples the behaviour becomes more complex. Darker colours correspond to thicker samples up to 6 layers then the colour can change from blue to yellow to grey [20].

Another useful optical technique to analyse the samples is the Dark Field (DF) microscopy. It is a widely used technique to visualize objects that have

low contrast in bright-field microscopy, such as surface contamination [57]. In DF microscopy, the central part of the illumination light which ordinarily passes through and around the sample is blocked by a light stop, allowing only oblique rays to strike the sample on the microscope slide [57]. If the oblique rays are scattered by the specimen (for example by crystal steps or surface contamination), the light will reach the objective and form the DF image, otherwise the light will miss the objective.

3.3 Raman analysis

Raman spectroscopy is a fast non-destructive characterisation method that makes use of inelastic light scattering to probe the vibrational and electronic properties of materials. This technique is particularly useful for organic materials in general, however it proves to be especially valuable for carbon allotropes, including graphene. Unlike other characterization techniques, Raman does not require any sample preparation or specific substrates and can be performed on functional electronic devices, even during their operation [58].

Raman scattering is the inelastic scattering of photons by phonons [59]. When a photon impinge on a sample creates a time-dependent perturbation in the Hamiltonian of the system. Due to the photon fast changing electric field, only electrons respond to the perturbation. The perturbation introduced by a photon of energy $\hbar\omega_L$ increases the total energy to $E_{GS} + \hbar\omega_L$, where E_{GS} is the ground state energy. In general, $E_{GS} + \hbar\omega_L$ does not correspond to a stationary state, therefore the system is said to be in a virtual level. In classical language, a virtual level corresponds to a forced oscillation of the electrons with a frequency ω_L. After a small time interval, the system tends to exit from the non-stationary energy state $E_{GS} + \hbar\omega_L$, and moves back to a stable state. One can formally consider the photon as being emitted by the perturbed system, which jumps back to one of its stationary states [59].

The photon scattering process can be either elastic or inelastic. In the first case, called Rayleigh scattering, the frequency of the emitted photon is the same as the incident one and the main effect is that the photon changes its

propagation direction. Instead in a Raman process the scattering is inelastic and the photon can either reduce or increase its energy. Raman scattering happens always with a much lower probability than Rayleigh scattering [59].

When the photon loses part of its energy in the interaction process, it exits the sample with a lower energy $\hbar\omega_{Sc}$. This corresponds to the Stokes (S) process. Since the sample has to return to a stationary state, the energy loss must correspond to a phonon energy $\hbar\omega_L - \hbar\omega_{Sc} = \hbar\Omega$. If the incoming photon finds the sample in an excited vibrational state, and after the interaction the system returns to its ground level, the photon can leave the sample with an increased energy $\hbar\omega_{Sc} = \hbar\omega_L + \hbar\Omega$. This corresponds to the Anti-Stokes (AS) process [60]. Figure 3.5 shows a sketch of the process.

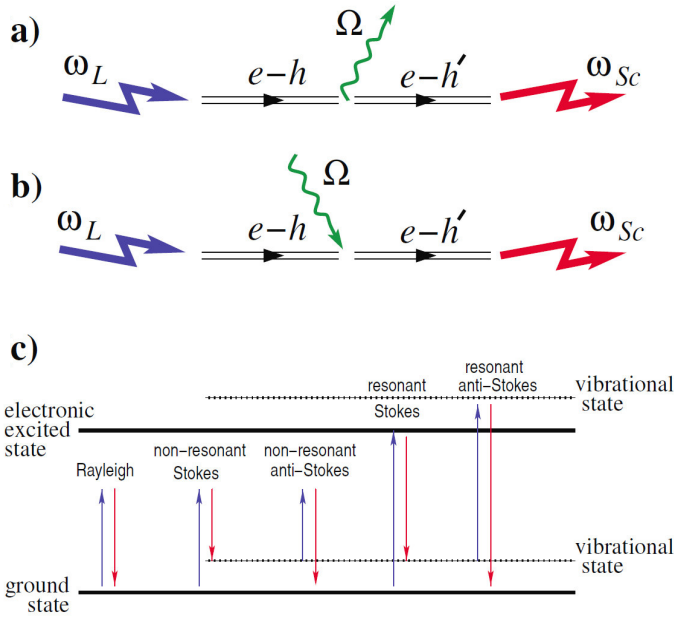

Figure 3.5: Raman Scattering. a) Stokes. An incoming photon ω_L excites an $e-h$ pair. This pair decays into a phonon Ω and another electron-hole pair $e-h'$. The latter recombines, emitting a photon ω_{Sc}. b) Anti-Stokes. The phonon is absorbed by the $e-h$ pair. c) Rayleigh and Raman scattering in resonant and non resonant conditions. Adapted from [60].

Given that S is the most probable, the vast majority of Raman spectra in literature are S measurements plotting the intensity of the scattered light as a function of the difference between incident and scattered photon energy,

the so called "Raman shift" [59]. Even though the Raman shift units should be those of energy, it is historically plotted in cm^{-1}. This can be converted in meV using the relation $1\,meV = 8.0655\,cm^{-1}$.

The S/AS ratio depends on the sample temperature, and is a very popular method to monitor it. Since, in order for an AS process to take place the system must be in an excited vibrational state in the first place, this may occur through thermal excitation [59].

When $E_{GS} + \hbar\omega_L$ does not correspond to a stationary state the Raman scattering is called non-resonant. If the excitation is selected to match a specific energy level, then the process is called resonant, and the intensities are strongly enhanced, as a result of the greater perturbation efficiency [60, 59].

The peculiar band structure of graphene, with the absence of a band gap makes all wavelengths of incident radiation resonant, thus the intensity of the Raman spectrum is enhanced and contains information about both atomic structure and electronic properties [60].

The Raman spectrum of graphene, similar to other carbon-based materials, consists of only few prominent features. It is the shape, position and intensity of these peaks that contains the information (e.g. doping, defects, strain, disorder, chemical modifications, edges) and therefore accurate data interpretation is essential [60, 61].

Excitations used for Raman spectroscopy are typically in the IR to UV spectral range [60]. The wavelengths used in this work are $514\,nm$ on the $Si - SiO_2$ substrate and $457\,nm$ on the copper one. The reason that leads to use the green laser ($514\,nm$) on the silicon substrate is that this wavelength matches with the interference condition required to enhance the contrast of the graphene (see section 3.2) and thus the emitted light is more intense.

Concerning the copper substrate another emitting phenomena has to be consider, the photoluminescence. In a photoluminescence (PL) process an electron and a hole recombine radiatively, i.e. emitting a photon, at a wavelength typical of the material electronic structure. When the laser impinge on the sample multiple recombinations may lead to a PL broad background. The intensity of the background depends on the exciting

wavelength but the PL peaks position, plotted on an absolute energy scale, does not (unlike in Raman scattering) [59]. Figure 3.6 shows an example of PL background.

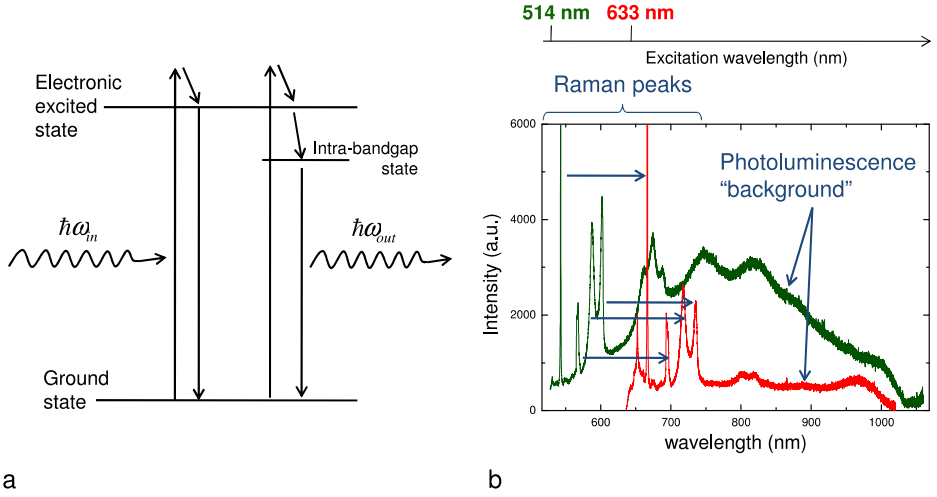

Figure 3.6: Photoluminescence. a) Sketch of a photoluminescence process. An electron and a hole recombine radiatively at a wavelength typical of the material electronic structure. b) Photoluminescence background. The intensity of the background depends on the exciting wavelength but the PL peaks position, plotted on an absolute energy scale, does not (unlike in Raman scattering).

Copper substrate, excited with a green laser, has a strong photoluminescence that overlaps the Raman peaks of graphene and makes difficult the interpretation of the spectra, thus a blue laser ($457\,nm$) is preferred. Figure 3.7 shows the spectra of graphene on copper both with $514\,nm$ and $457\,nm$ wavelengths.

The typical spectrum of a single layer graphene looks like Figure 3.8.

The two most intense features are the G peak at $1580\,cm^{-1}$ and the 2D band at $2700\,cm^{-1}$ [61]. In monolayer, not doped graphene the 2D peak is a sharp peak roughly four times more intense than the G peak. Other slightly intense peaks are present: the 2D' at $\approx 3200\,cm^{-1}$, the D+D'' at $\approx 2450\,cm^{-1}$ and the D peak at $1350\,cm^{-1}$. This last peak is due to the presence of defects and edges in the structure, thus it is a index of the

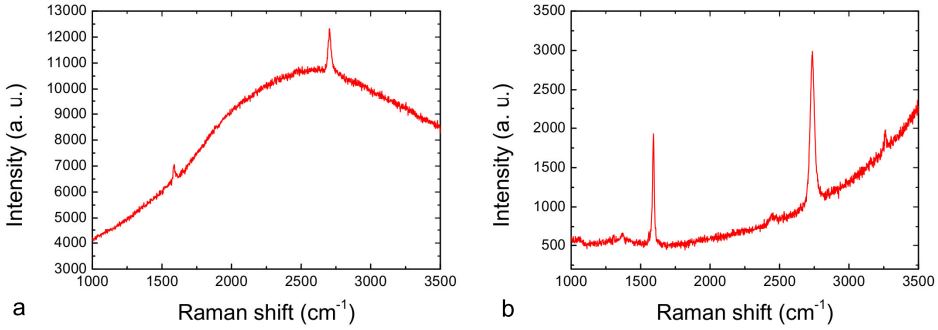

Figure 3.7: Raman spectra of graphene on copper. a) Spectrum acquired with a 514 nm wavelength laser. The photoluminescence background completely overlaps the Raman peaks of graphene. b) Spectrum extracted with a 457 nm wavelength laser. The photoluminescence background is shifted with respect the graphene peaks, thus they can be clearly detected.

homogeneity of the structure.

Figures 3.9 plots the evolution of the 2D band as a function of layers for 514 nm excitation. These immediately indicate that a bilayer has a much broader and up-shifted 2D band with respect to graphene. It has four components, two of which, have higher relative intensities than the other two. A further increase in layers leads to a significant decrease of the relative intensity of the lower frequency 2D peaks. For more than five layers the Raman spectrum becomes hardly distinguishable from that of bulk graphite [61].

These spectra are all extracted measuring perfectly Bernal stacked layers obtained from exfoliated graphite. However, not all multilayers are Bernal stacked, also turbostratic structure (not aligned superposed layers) are present, thus it is possible to observe more complex 2D peak shapes than those described so far, for example, in samples grown by chemical vapour deposition (as the samples in this work). Turbostratic graphite has a single 2D peak, but its full width at half maximum (FWHM) is 50 cm^{-1}, almost double that of the 2D peak of graphene and up-shifted of 20 cm^{-1} with often a first order D peak [60].

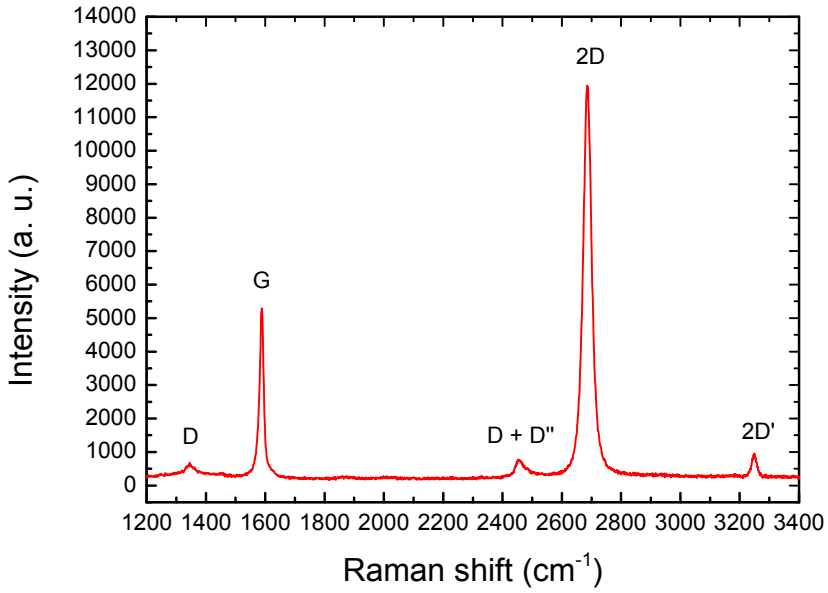

Figure 3.8: Single layer graphene Raman spectrum. The two most intense features are the G peak at $1580\,cm^{-1}$ and the 2D band at $2700\,cm^{-1}$. Other slightly intense peaks are the 2D′ at $\approx 3200\,cm^{-1}$, the D+D″ at $\approx 2450\,cm^{-1}$ and the D peak at $1350\,cm^{-1}$.

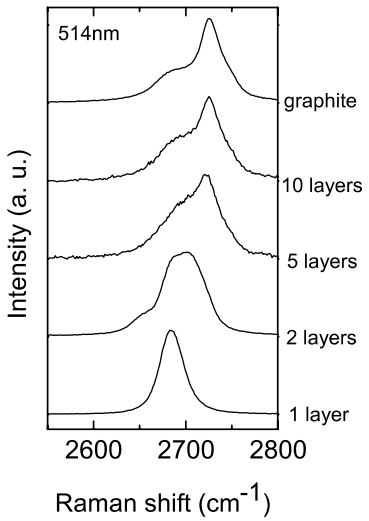

Figure 3.9: Evolution of the 2D band as a function of layers for $514\,nm$ excitation. Adapted from [61].

The position and the intensity of the G and the 2D peaks are also influenced by the doping level of graphene. The G peak sharpens for both electron and hole doping, while the 2D peak shows a different response to holes and blue-shifting of electrons, thus G and 2D peaks have different doping dependence and the 2D/G height ratio can be a sensitive parameter to monitor it [58].

The Raman spectrometer used to perform the measurements is shown in Figure 3.10. The laser, emitted by a Ar-Kr ion laser, passes through different filters and is focused under an optical microscopy. The beam interacts with the material and photons containing the information about the sample are emitted. The produced beam contains both elastic and inelastic photon scattering processes, thus the beam is directed through a notch filter to eliminate the elastic component to have a more accurate analysis of the data. The beam then runs into a diffraction grating that spits the different wavelengths and collected them in a CCD camera that counts the number of the different photons emitted.

3.4 Transfer procedure

In this section, the technique used to transfer the CVD graphene samples from the copper substrate (where graphene is grown) onto arbitrary ones is described. It consists in the deposition of a protective layer of poly methyl methacrylate (PMMA) on the graphene layer, followed by the etching of the copper in an acid solution. The PMMA/graphene film is then manually transferred onto the desired substrate and finally, PMMA is removed by organic solvent. Since are used an acid solution to dissolve the substrate and a solvent to remove the polymer, this is usually referred as ”wet transfer”.

During the CVD growth, graphene deposits on both sides of the Cu substrate, but not with the same quality. The inner surface has better catalytic properties and moreover, during the growth, the external side might touch the quartz tube obtaining a lower quality graphene.

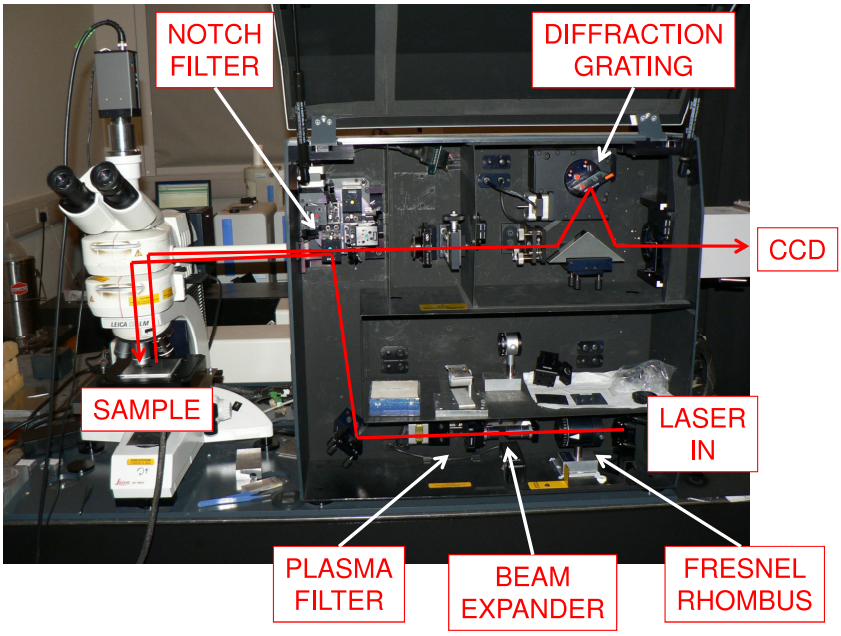

Figure 3.10: Raman spectrometer used to perform the measurements. The red line shows the path of the laser.

The first step is to spin coat a layer of PMMA on top of the high quality side. Spin coating is a procedure used to deposit a uniform thin film on flat substrates. A small amount of coating material is dropped on the centre of the substrate. This is then rotated at high speed in order to spread the coating material by centrifugal force. The coating material usually contains the film material blended with a volatile solvent that largely evaporates during the rotation. The higher is the angular speed of spinning, the thinner is the film. The final thickness depends also on the viscosity of the solution.

The spinning is performed using a PET foil to support the substrate. The copper sample is cut in the desired dimensions, keeping the higher quality graphene on top. It is then placed on the PET foil and fixed on it with some tape (Figure 3.11). The PET foil is then placed on the spinner and rotated for $40\,s$ at $4000\,rpm$. The coating material used is PMMA 950 A4. The name indicates the molecular weight of the polymer 950K and the percentage of it (4%) diluted in Anisole.

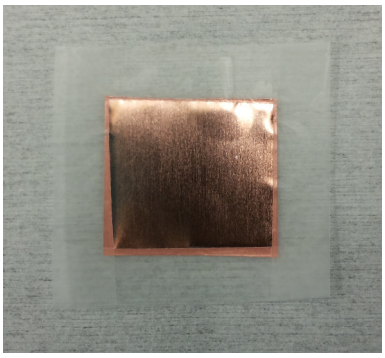

Figure 3.11: Transfer procedure: copper sample fixed on PET foil with tape.

After that, in order to remove the low quality graphene from the back surface, an etching step is required. It has been chosen to use the reactive ion etching (RIE), a technique that uses chemically reactive plasma to remove material deposited on a surface. The plasma is generated under low pressure by an electromagnetic field. High-reactive radicals are accelerated towards the surface and react with it.

To do this procedure, the copper foil is carefully detached from the PET support and placed in the vacuum chamber with the backside on top.

A cycle with plasma oxygen at 150 $mTorr$ of pressure for 30 s at 30 W is performed.

The Cu foil is then etched using a solution of ammonium persulfate in de-ionized water. The sample is laid on the surface of the aqueous solution, with the PMMA layer on top, and kept floating until the copper foil is completely dissolved. Figure 3.12 shows different etching steps. At the beginning the solution is colourless. After few hours some holes start to be visible on the copper foil and the solution acquires a light blue shade. At the end of the process the copper foil is completely removed and the solution is blue. The darker is the blue shade, the higher is the concentration of copper atoms in solution.

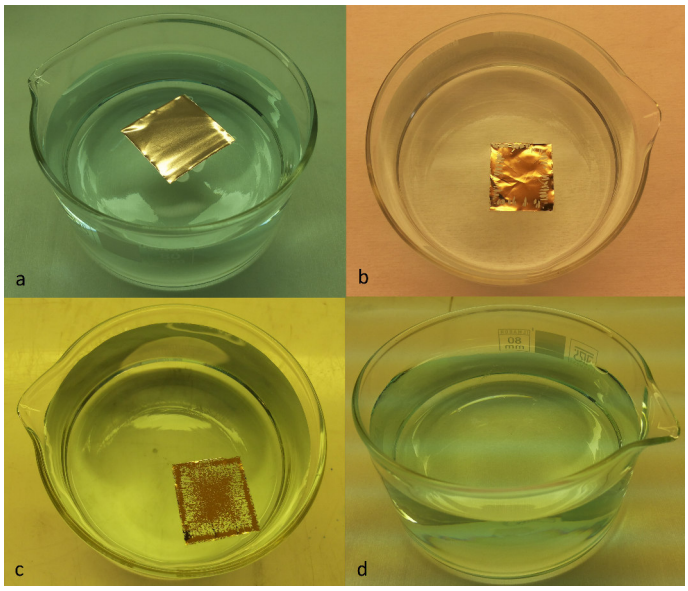

Figure 3.12: Transfer procedure: copper etching in ammonium persulfate solution. a) Sample just laid on the surface. b) Sample after $\approx$ 2 hours etching. Some holes start to be seen. c) Sample after $\approx$ 4 hours etching. Only few copper spots are left. d) Sample etched. The foil is completely transparent.

There is a trade-off between the etchant concentration and the total time needed for the etching. A strong acid solution dissolves quicker the copper foil but also can act on the graphene layer lowering the quality. Thus, higher quality graphene is obtained keeping the sample in a low concentrate solution for long time.

As soon as the copper is completely etched the sample has to be removed from the solution to avoid further action of the acid on the graphene foil.

The etching time depends also on the size of the copper foil. The bigger is the sample, the longer is the etching time since the amount of copper to dissolve is higher.

In order to have a good graphene layer the etching has to last at least 5-6 hours. A recipe is presented here as reference: a sample with a surface area of $4\,cm^2$ needs $1.8\,g$ of ammonium persulfate dissolved in $150\,ml$ of de-ionized water and the complete etching is obtained in 6 hours.

Once the copper is completely dissolved the sample is rinsed in de-ionized water for $15\,min$ to remove the residual etchant. The transparent foil floating in the solution is really fragile and can be easily damaged. Thus, the operation to take it from the etchant solution, called "fishing", is extremely delicate. It is performed with a piece of PET, earlier cleaned with acetone and IPA, immersed in the acid solution and approached to the transparent layer. Once, due to adhesion force between the graphene and the PET, one side of the graphene foil sticks on the PET, the plastic foil is slowly extracted from the water with the graphene layer laid on top as smoothly as possible. The PET foil is then slowly immersed in de-ionized water, where the graphene foil detaches and floats on the surface. This step can be repeated few times, using clean water every time, for additional cleaning.

After the last cleaning process, the $Si - SiO_2$ substrate is used instead of PET to fish the graphene foil. Before the fishing procedure, the $Si - SiO_2$ substrate has to be shaped and cleaned. First, the substrate is cut in the desired dimensions, then it is immersed for few minutes in acetone first and then in IPA, using an ultrasonic bath to make sure that all the dirtiness on the surface detaches. Once it is cleaned, the fishing procedure can be performed as described before.

The resulting sample is then placed on a vertical support and left to dry in air for at least 8 hours. The sample is laid vertically to increase the water flow and avoid the formation of blisters between the substrate and

the graphene. Faster dry with either an air flow or a higher temperature is discouraged since it could damage the graphene layer.

Finally, the sample is immersed in acetone to dissolve the PMMA layer. The rate of dissolution follow a decreasing exponent law: in the first few minutes most of the PMMA is removed but to eliminate the last part of the polymeric cover up to several days can be required.

The light blue spots sometime visible on the optical image of the graphene layers are PMMA residuals due to the wet transfer technique just described.

Optical image and Raman analysis are the two main instruments used to check the quality of the final transferred layer and in which amount the transfer procedure modifies the graphene properties.

To prove the success of the transfer, Raman analysis are performed before and after the procedure. Figures 3.13 and 3.14 show the spectra obtained with a 457 nm laser on copper and on the silicon substrate of two samples used in this work.

As can be seen, excepting for the photoluminescence background of the copper, the spectra before and after the transfer have the same features, with no enhancement of the D peak, indicating that the transfer procedure does not induce additional structural defects.

3.5 Electrical measurements setup

In order to assess the suitability of the graphene films grown by CVD for sensing applications, their electrical properties are measured by integrating the films into field-effect transistors. Such devices are fabricated both using standard and optimized graphene to compare their properties. Electrical measurements in both two and four probe configuration allowed extraction of sheet resistance, charge carrier mobility and contact resistance.

The total resistance of a sample can easily be determined with a two-point probe measurement: two tips are used to inject a current I trough the sample and measure the resultant electrical potential distribution V.

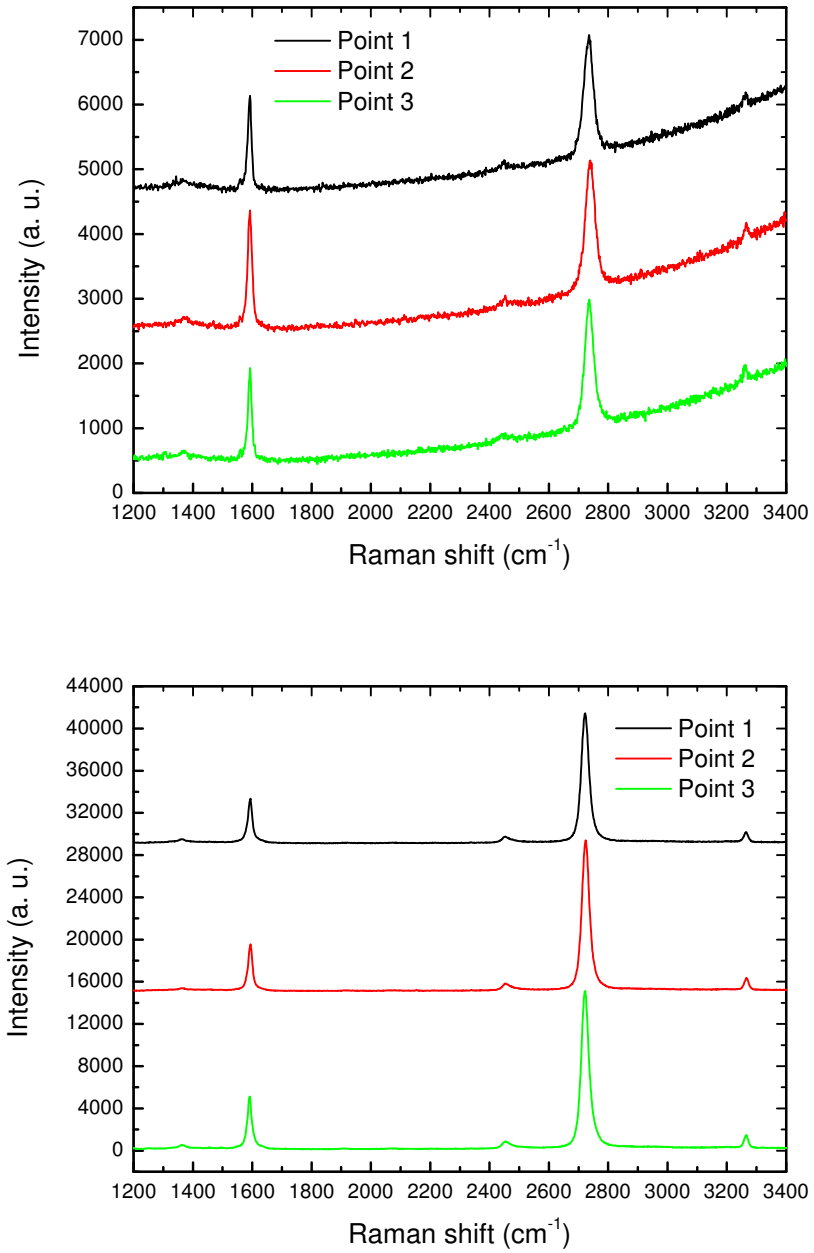

Figure 3.13: Raman spectra captured with 457 nm wave length laser on sample T01. Up) Raman spectra before transfer, on copper surface. Down) Raman spectra after transfer, on $Si - SiO_2$ substrate.

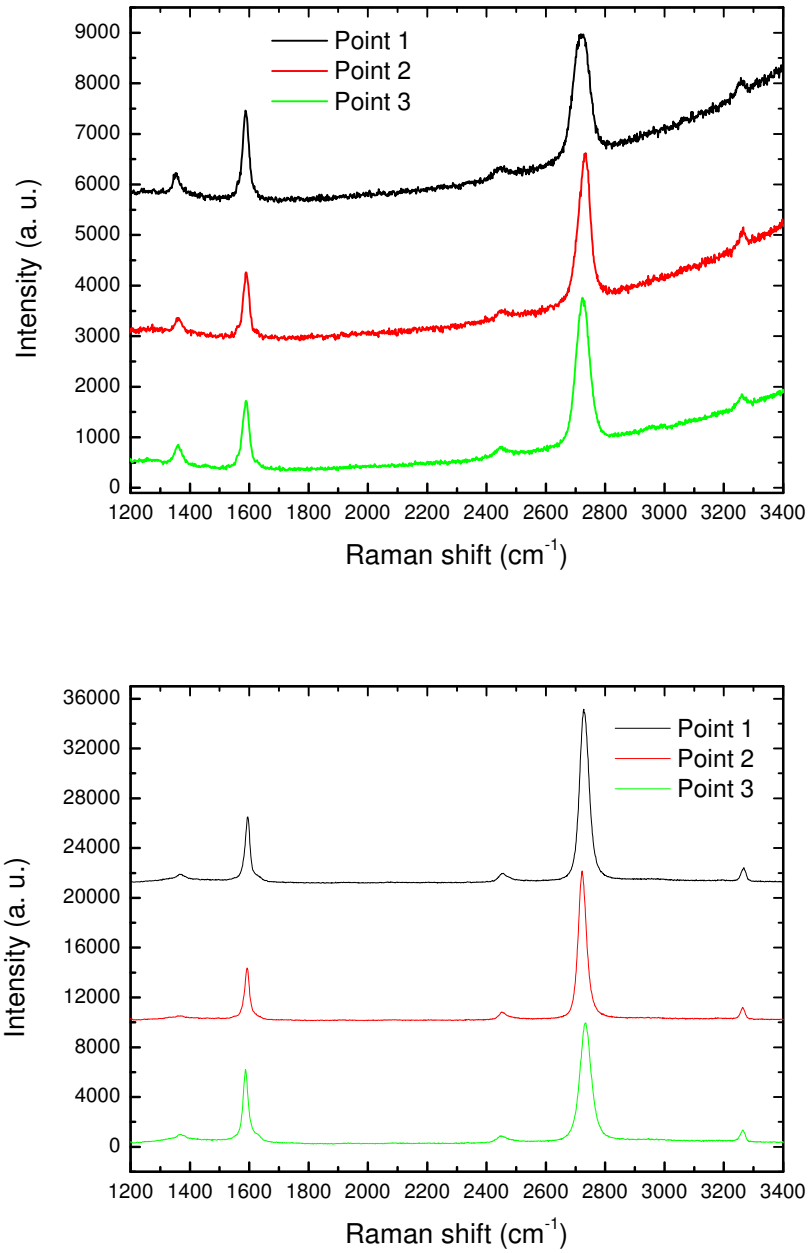

Figure 3.14: Raman spectra captured with 457 nm wave length laser on sample T07. Up) Raman spectra before transfer, on copper surface. Down) Raman spectra after transfer, on $Si - SiO_2$ substrate.

Assuming an Ohmic behaviour, the total resistance R_{tot} between the two tips can be calculated as:

$$R_{tot} = \frac{V}{I} \tag{3.3}$$

R_{tot} can be considered as a sum of different components:

$$R_{tot} = R_{gr} + 2R_c + 2R_m \tag{3.4}$$

where R_{gr} is the resistance of the channel, R_c is the resistance associated with the metal-graphene interface and R_m is the resistance due to the metal [62].

The resistance of a single contact would be $R_m + R_c$. However, in most situations, the resistivity of the metal in the contact is so low that $R_c >> R_m$, so R_m can be ignored.

3.5.1 Sheet resistance

Sheet resistance is typically used to characterize electrical properties of thin films.

When the sample dimensions are known, measurements of R_{gr} allow to determine the sample's resistivity ρ [63]:

$$R_{gr} = \frac{V}{I} = \frac{\rho\, L}{w\, h} \tag{3.5}$$

where L is the length of the channel, w the width and h the thickness of the film.

For thin conducting films, h is often unknown, and thus the only parameter that can be directly determined is the sheet resistance R_s of the film, defined as [63]:

$$R_s = \frac{\rho}{h} \tag{3.6}$$

Thus,

$$R_{gr} = R_s \frac{L}{w} \tag{3.7}$$

The measurement unit of R_s is "ohms per square" (Ω/sq), and represents the resistance of a squared sample of the material, regardless of the dimensions.

Today, four-point probe technique is the most used technique for the testing of thin films [63].

The classic arrangement of a four-probe measurement requires four needle-like electrodes in a linear arrangement. The two outer electrodes are used to inject the current while the voltage drop is measured with the two inner electrodes. Figure 3.15 shows the standard configuration of the electrodes.

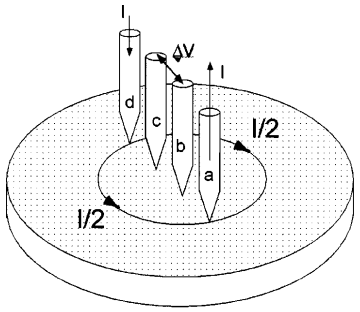

Figure 3.15: Standard configuration of the electrodes in a four-probe measurement. (Adapted from [64])

By using separate electrodes for the current injection (Force) and for the determination of the electric potential (Sense), the contact resistance between the metal electrodes and the material will not affect the measured results [64]. The sensing electrodes have a very big internal resistance in order to stop the passage of the current through them, thus the inner voltage measured is only due to the channel resistance R_{gr}.

3.5.2 Contact resistance

The metal-graphene contact resistance is usually measured using a combination of two and four-probe measurements or using the transfer length method (TLM) [65].

Since R_{tot} and R_{gr} can be evaluated respectively with two-probe and four-probe measurements, the first approach to calculate the contact resistance R_c come from Eq. 3.4. Considering R_m negligible:

$$R_c = \frac{R_{tot} - R_{gr}}{2} \tag{3.8}$$

Another method to calculate the contact resistance is the transfer length method (TLM). The value extracted with this method includes all the parameters that are not affected by the channel length [62].

The TLM is based on the equation below:

$$R_{tot} = R_s \frac{L}{w} + 2R_c \tag{3.9}$$

where R_{tot} is the total resistance, R_s the sheet resistance in the channel and L and w are the length and the width of the channel, respectively.

If resistors of several different lengths are constructed, keeping all other parameters the same, the total resistances of each can measured and plotted versus the channel length. In the limit of a zero-length resistor, the residual resistance is just twice R_c, thus the contact resistance can be extracted by the y-intercept of the plot [62]. A graphical representation of the method is shown in Figure 3.16.

The contact resistance thus calculated depend on the dimensions of the contacts themselves. To normalize the values and make them comparable to each other the unit length contact resistance R_{uc} can be calculated as [65]:

$$R_{uc} = R_c\, w \tag{3.10}$$

where w is the width of the channel.

3.5.3 Mobility

Among the several methods to evaluate the charge carrier mobility in graphene, the simpler one measures the field-effect mobility by means of a field-effect transistor (FET).

A FET is a three terminals device, with two of them (source and drain) separated by a channel and the third one (called gate) under it and insulated with a thin dielectric layer. Figure 3.17 shows the standard configuration.

The operation of a conventional FET relies on the modulation of the channel conductivity, and thus the drain current I_{DS}, with a voltage signal

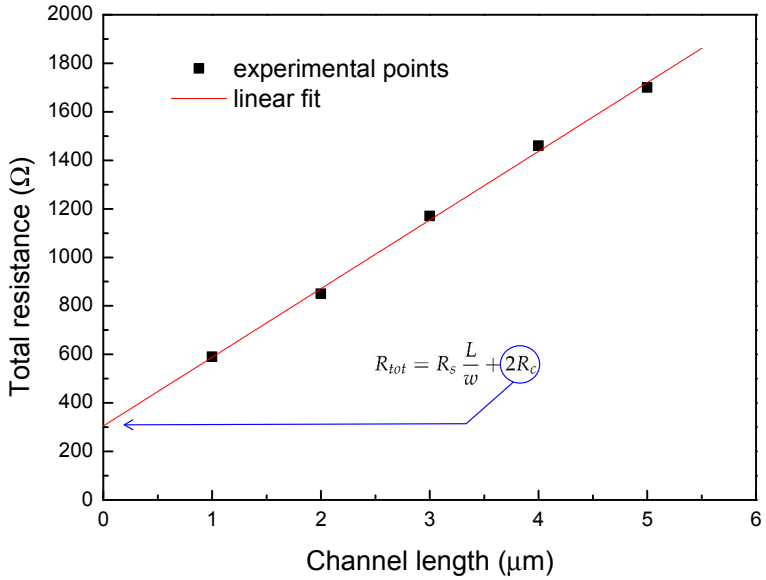

Figure 3.16: TLM method. Total resistance R_{tot} versus the channel length L. The y-intercept gives the total contact resistance.

V_G applied between the gate and the source [17].

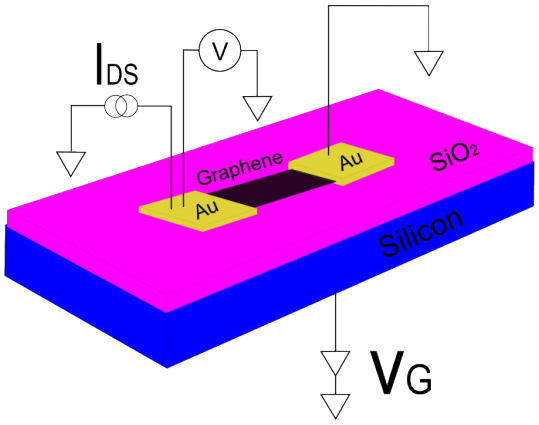

Figure 3.17: Schematic view of the transistor structure: the metallic electrodes (yellow) on top of graphene (black) are the transistor's source and drain, and the Si substrate (dark blue) covered by SiO_2 (pink) acts as the gate. Adapted from [66]

The standard measurement is performed keeping the source-drain voltage V_{DS} constant and sweeping the gate voltage V_G. The typical current-voltage trans-characteristic for graphene transistors is shown in Figure 3.18.

The carrier density and the type of carrier (in graphene electrons or holes) in the channel are governed by the potential difference between the channel and the gate. Positive gate voltage promote an electron accumulation in the channel (n-type channel), and negative gate voltage lead to a p-type channel with an excess of holes between source and drain. This ambipolar field effect gives rise to the two branches of the trans-characteristic separated by the so called Dirac point which corresponds to the neutrality point in which the Fermi level is found in absence of doping [17].

The field effect mobility can be extracted from the trans-characteristic with the following mathematical expression [67]:

$$\mu_{FE} = \frac{\Delta I_{DS}}{\Delta V_G} \frac{L}{w\, C_{OX}\, V_{DS}} \tag{3.11}$$

where I_{DS} and V_G are respectively the drain current and the gate voltage, thus $\frac{\Delta I_{DS}}{\Delta V_G}$ is the slope of the curve in Figure 3.18. This formula is based on the formation of a capacitor between the graphene and the silicon back

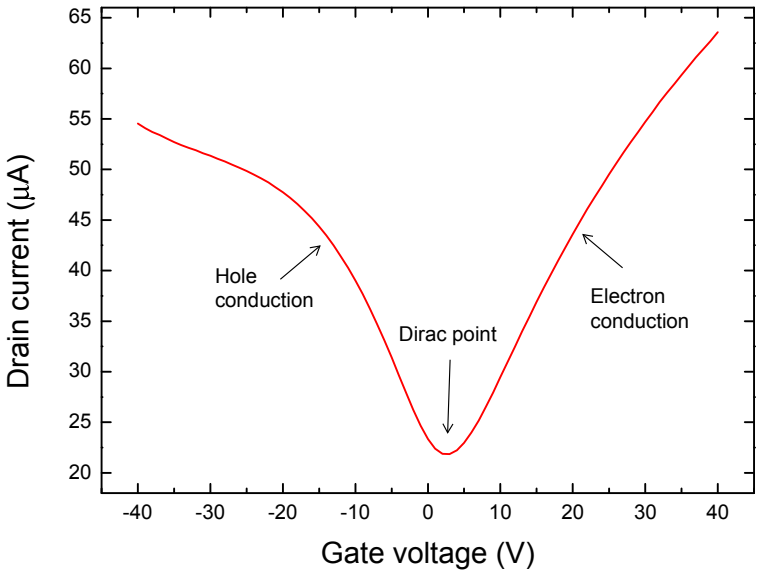

Figure 3.18: Typical current-voltage trans-characteristic for graphene transistors.

gate and it is more accurate in the proximity of the Dirac point, where the maximum slope is found. L and w are the channel length and width while V_{DS} in the fixed drain voltage. C_{OX} is the gate capacitance per unit area defined as [68]:

$$C_{OX} = \frac{\epsilon_0 \epsilon_r}{d} \tag{3.12}$$

where ϵ_0 is the vacuum permittivity, ϵ_r is the relative permittivity of the SiO_2 and d is the thickness of the SiO_2.

3.6 Devices fabrication

To fabricate the devices, initially dimensions and shape of the structures have to be designed in order to ensure accurate measurement of the desired properties. Then, few technological steps are required to make the contacts and define the channels to obtain the final structure.

3.6.1 Design

Two different structures have been designed. One for two and four-probe I-V measurements and one for the TLM technique. The two configurations are shown in Figure 3.19 and Figure 3.20.

To perform an electrical measurement several metallic contacts have been realized in order to define different micrometric channels on the structure. Since the dimension of the tips used for the measurements is also about few micrometers it is impossible to contact directly the metal strips between the channels. Thus, every contact has to be connected with an external pad. All the connections for the two devices are shown in the left part of Figures 3.19 and 3.20.

To perform a four-probe measurement four contacts are needed. The device contains 10 contacts in order to allow measurements on different channels in the same device. The right part of Figure 3.19 shows a zoom of the contacts. The channels have width $w = 40\,\mu m$ and length $L = 5\,\mu m$.

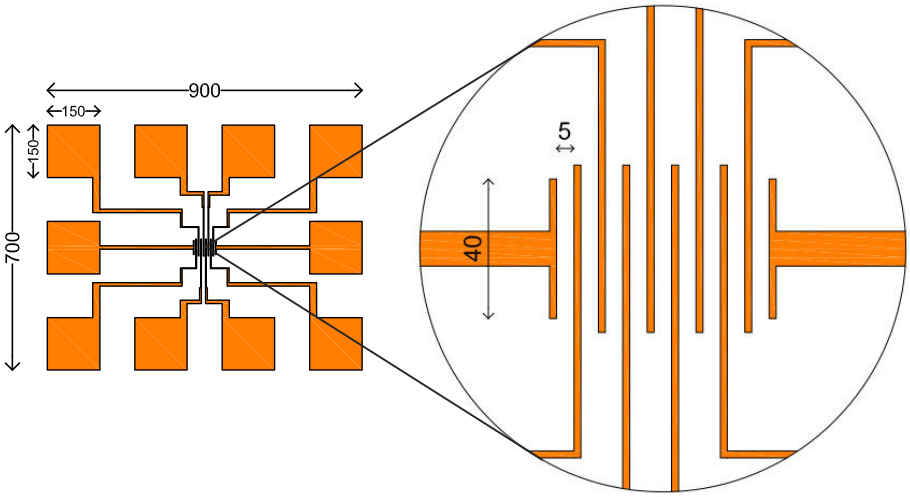

Figure 3.19: Sketch of the device used for the four-probe measurements. On the left all the device, on the right a zoom of the channels. All the sizes are in μm.

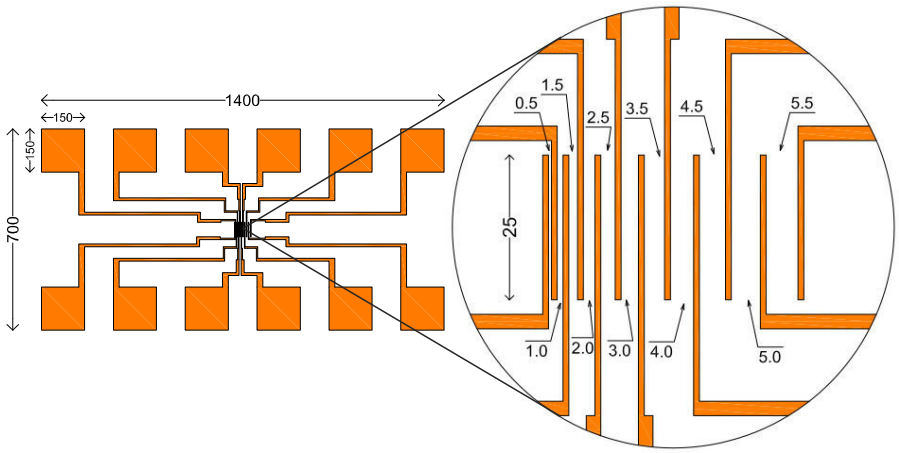

Figure 3.20: Sketch of the device used for TLM measurements. On the left all the device, on the right a zoom of the channels. All the sizes are in μm.

The TLM measurement needs different channels with increasing length and properties as more homogeneous as possible. The device has been thus designed with 11 contacts with increasing length from $0.5\,\mu m$ to $5.5\,\mu m$. The right part of Figure 3.20 shows the contacts configuration.

3.6.2 Contacts fabrication

An evaporation process is used to deposit the desired metallic structure on the samples. Since the evaporation is not a selective process and the metal deposits on all the surface of the samples, the definition of the pattern has to be done with a lithography. A summary of the process is shown in Figure 3.21.

The lithography has been done with an Nanobeam NB1 electron-beam system. The e-beam lithography consists in scanning a beam of electrons focused on a surface covered with an electron sensitive film, called resist, along a predefined pattern. The electron beam changes the solubility of the resist enabling selective removal of either the exposed or non-exposed regions of the resist by immersing it in a solvent (developing).

A spin coating (a technique already explained in section 3.4) is used to deposit the resist on the samples. The deposition of a first layer of PMMA 495 A4 is followed by a second layer of PMMA 950 A2 for a total thickness of about $200\,nm$. The double structure is used to facilitate the resist lift-off.

Exposition of PMMA to the electron-beam decreases the polymer molecular weight, thus increases the solubility of the exposed part that will be removed during the developing.

Once the resist is deposited, the e-beam system is set to write the pattern previously designed. The writing needs few hours.

Then, the samples are extracted from the e-beam chamber and developed in a mixture of de-ionized water and isopropyl alcohol (IPA) for few seconds. In this process the polymer previously exposed dissolves while the rest of the layer remains intact.

Optical images of the resultant structures after the developing are shown in Figure 3.22. The darker part is the developed one, where the polymer

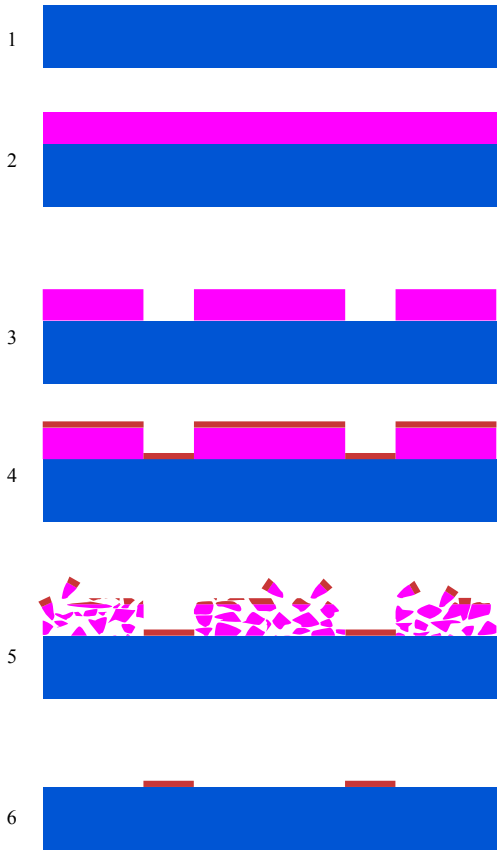

Figure 3.21: Summary of process used to create the metallic electrodes. 1. Preparation of the substrate. 2. Deposition of the sacrificial layer. 3. Patterning the sacrificial layer, creating an inverse pattern. 4. Deposition of the target material. 5. Resist lift-off. 6. Final pattern.

has been dissolved. Yellow shadows are visible all around it, this is due to a partial exposition of the edges of the pattern to the electrons and thus a partial developing.

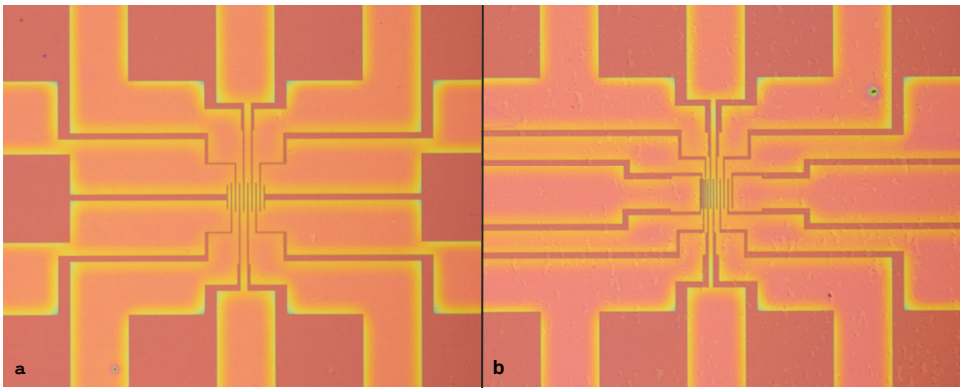

Figure 3.22: Optical images of the structure after lithography. The darker part is the developed one, where the polymer has been dissolved. The yellow shadow visible all around it is due to a partial exposition of the edges of the pattern to the e-beam and thus a beginning of developing.

The next step is the metal deposition in an evaporator. Thermal evaporation is a common method of thin-film deposition. The source material is evaporated in a vacuum chamber. It allows metal vapour particles to travel from the source to the target object, where they condense back to a solid state.

The metallic particles reach the substrate and condense all over the surface, partially covered with the polymer. At the end of the deposition, the polymer is removed from the substrate. Thus, only the metal deposited in the pattern previously developed will remain on the substrate.

The contacts are made with $80\,nm$ of gold, since it is a noble and very conductive metal. A very thin layer ($2\,nm$) of chromium is previously deposited on the graphene to improve the adhesion between the gold and the substrate. Both layers are deposited at pressure around $10^{-7}\,mbar$. As metal sources are used a chromium coated tungsten wire and an alumina coated tungsten wire basket filled with gold. By passing a large current through the tungsten wire, chromium and gold are heated up until they reach their evaporation temperature. A picture of the chamber ready for

the process is shown is Figure 3.23.

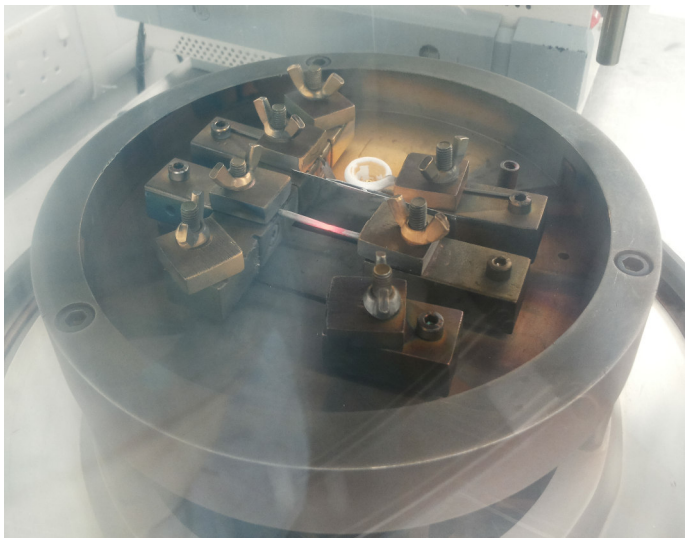

Figure 3.23: Evaporation chamber ready for the evaporation of chromium and gold. Forward the chromium coated tungsten wire, behind the alumina coated tungsten wire basket.

After the evaporation the samples are put in high purity acetone to dissolve the residual polymer. The whole process lasts at least 10 hours. When the polymer is completely dissolved the metal deposited on it is usually floating in the solution and has to be careful removed with tweezers. After checking the result the samples are washed in high purity IPA and dried with a flow of nitrogen. All this process is called lift-off.

Optical images of the final structures are shown in Figure 3.24. The metal pattern follows perfectly the structures previously designed.

3.6.3 Channels definition

Once the contacts are deposited, part of the graphene between the pads has to be removed, leaving only the defined channels. Without this procedure, the graphene layer surrounds the metallic structure and thus a voltage applied between two metallic pads will induce current through the whole substrate.

In order to remove selectively the graphene a second lithography is needed, followed but a reactive ion etching (RIE).

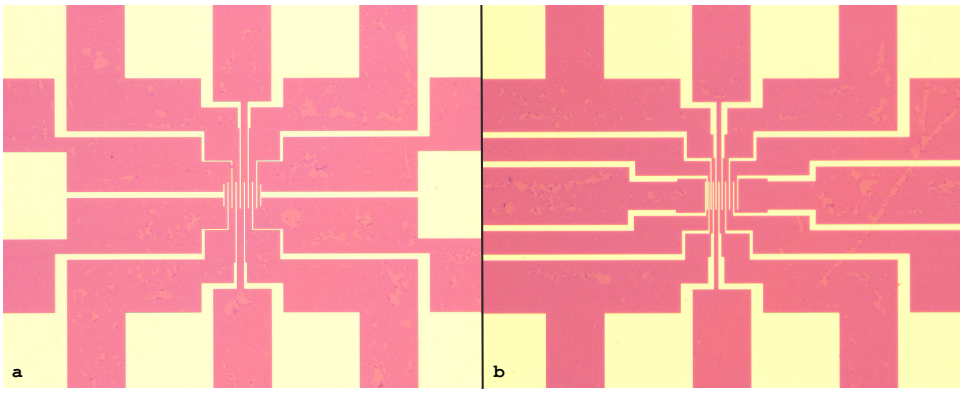

Figure 3.24: Optical images of the structures after evaporation and lift-off. The metal pattern follows perfectly the structures previously designed.

The second lithography is performed with PMMA 495 A8 as single layer resist. Double layer is no more required since the lithography is followed by an etching instead of a deposition. The patterns to write with the electron-beam are shown in Figure 3.25. The graphene has to be removed from all around the pads, leaving only a rectangle in the centre to define the channels.

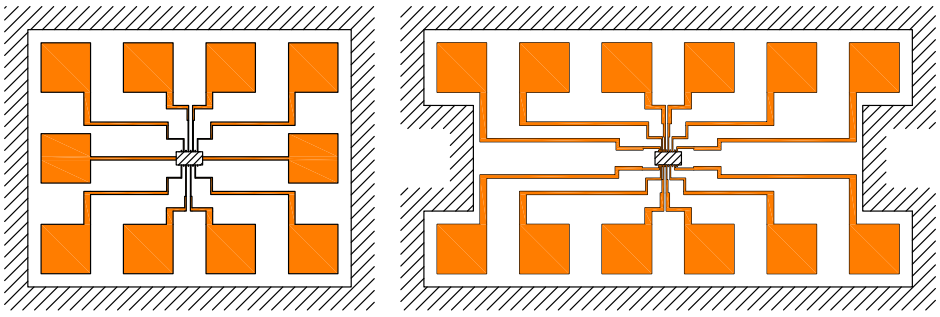

Figure 3.25: Sketch of the patterns needed for the etching. The graphene has to be removed from all around the pads, leaving only a rectangle in the centre to define the channels.

As before, the resist is deposited with a spin coater, then the samples are placed in the e-beam chamber and the system is set to write the patterns.

Once the patterns are written the samples are immersed in the water-IPA solution to develop for few seconds. Optical images of the resultant structures are shown in Figure 3.26.

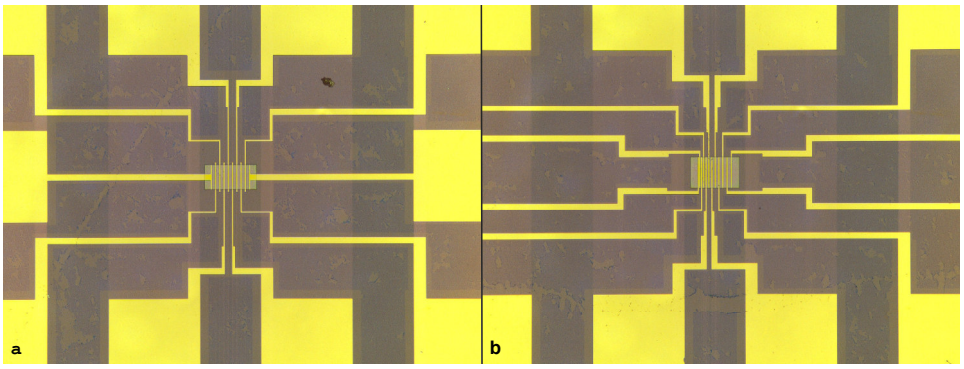

Figure 3.26: Optical images of the structure after the second lithography. The central part, in which the graphene does not have to be removed, is covered with the PMMA layer.

After that, the samples are put in the RIE chamber in order to remove the graphene. A cycle with plasma oxygen at 150 $mTorr$ of pressure for 2 min at 25 W is performed.

The samples are then immersed in high quality acetone for at least 10 hours to remove the residual polymer and finally washed in high purity IPA.

At this point, the samples are ready to be characterised with the procedure described in section 3.5.

Chapter 4

Experiments and Results

The results of the CVD growth and the following electrical measurements will be shown is this chapter.

In the first section the recipes developed to optimize the CVD growth will be explained in details, showing optical and Raman analysis of all the samples obtained. Once the surface topography has been optimized for maximum edge density, the optimized graphene, has been integrated into field-effect transistors and its electrical properties have been investigated. As comparison all the electrical measurements have been done also on a sample made with standard monolayer graphene.

In the second section the data obtained from the electrical measurements will be shown and analysed. The two samples will be compared and an explanation of the different properties of them will be provided.

4.1 Optimization of CVD growth

Starting from a recipe to grow single layer graphene, new recipes have been investigated to understand how the growth parameters can modify the surface. The goal was to increase the chemical reactivity of the layer keeping the same electronic performances. This is made possible by growing a two-layer material, consisting of a continuous bottom layer covered by a discontinuous layer consisting of closely packed islands.

4.1.1 Standard monolayer recipe

Sample T01

Single layer continuous graphene films are required for a variety of applications that require large-area graphene. This work starts from the conditions normally used to grow polycrystalline continuous films on Cu foils, here indicated as "standard" graphene. This "standard" material will be used as reference for comparing structural and electrical properties of the optimized graphene.

The recipe to grow monolayer graphene is described in table 4.1 and the process is summarized in Figure 4.1.

Heating	
Temperature:	55 min up to 900 $^{\circ}C$ 20 min up to 1000 $^{\circ}C$
Gas flow:	H_2 20 $sccm$
Pressure:	$\approx$ 190 $mTorr$
Time:	1 h and 15 min

Annealing	
Temperature:	1000 $^{\circ}C$
Gas flow:	H_2 20 $sccm$
Pressure:	$\approx$ 190 $mTorr$
Time:	30 min

Growth	
Temperature:	1000 $^{\circ}C$
Gas flow:	H_2 20 $sccm$ CH_4 5 $sccm$
Pressure:	$\approx$ 290 $mTorr$
Time:	30 min

Cooling down	
Temperature:	from 1000 $^{\circ}C$ to 25 $^{\circ}C$
Gas flow:	H_2 20 $sccm$
Pressure:	$\approx$ 190 $mTorr$
Time:	few hours

Table 4.1: Recipe to growth single layer graphene.

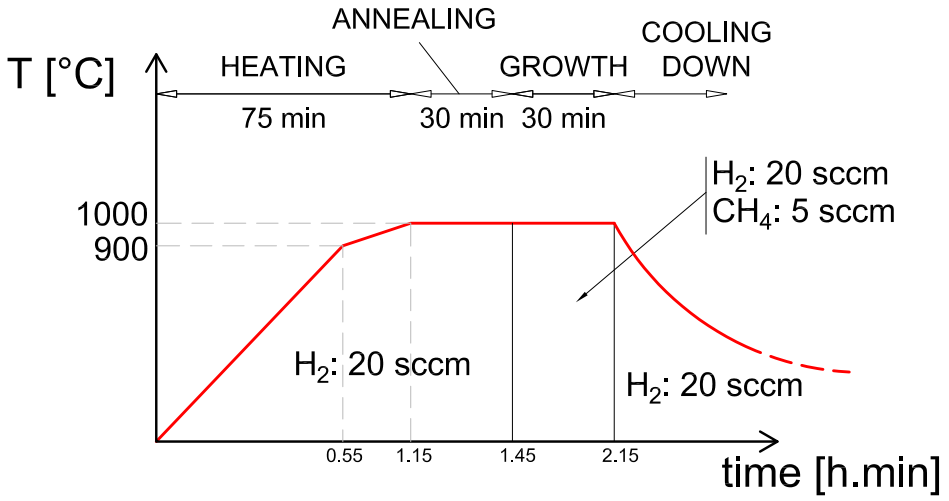

Figure 4.1: Sample T01. Time and temperature used to grow standard monolayer graphene.

The growth of monolayer graphene requires a pressure in the range of hundreds of $mTorr$, gas ratio CH_4:H_2 = 1:4 and a growth time of 30 minutes. The amount of H_2 flowing during the annealing is set to be consistent with the value needed for the growth. During the annealing process high temperature and a reducing atmosphere are the important conditions while the gases concentration has limited effect on the final result.

The heating process is divided in two different steps with different heating rate due to thermal inertia of the heater. Indeed, if a high rate is used, the system might reach a temperature higher than the set-point, leading to partial melting of the copper foil. To avoid that, it is a good practice to divide the heating in two steps, with reduced rate in the second one. Firstly the temperature is increased up to 900 $^{\circ}C$ with a rate of 16$^{\circ}C/min$, then it is set to reach the steady state value of 1000 $^{\circ}C$ with a rate of 5 $^{\circ}C/min$.

Optical image and Raman spectra of the graphene layer transfered on $Si - SiO_2$ substrate are shown respectively in Figure 4.2 and 4.3.

The optical image shows a perfectly smooth and homogeneous graphene layer. The Raman analysis performed on three different points of the sur-

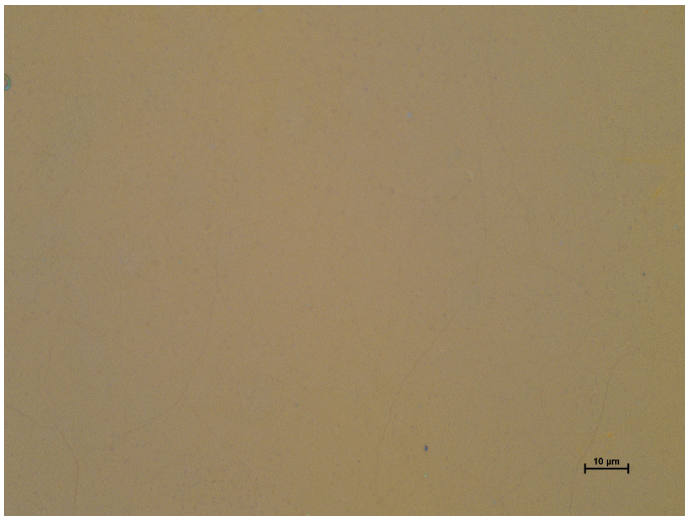

Figure 4.2: Sample T01. Optical image of single layer graphene on $Si - SiO_2$ substrate, grown with the standard monolayer recipe described in Table 4.1.

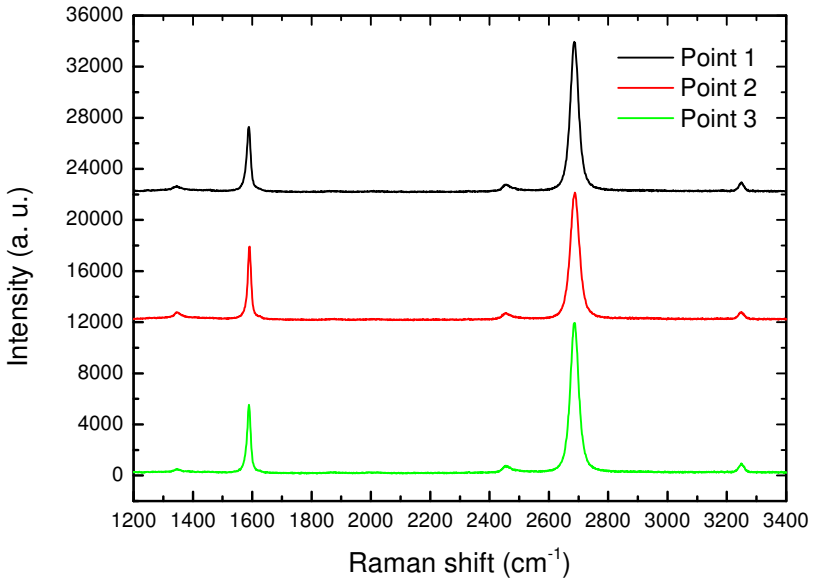

Figure 4.3: Sample T01. Raman spectra acquired with 514 nm wave length laser on $Si - SiO_2$ substrate. Single layer graphene grown with the standard monolayer recipe described in Table 4.1.

face (see Figure 4.3) proves that the graphene is single layer (see section 3.3 for the complete analysis explanation).

4.1.2 New recipe developing

Several growths have been performed for different values of the main parameters - pressure, temperature, growth time, gases ratio - in order to grow a second, discontinuous graphene layer. This improves the adhesion properties and enhance the chemical reactivity, because of the large amount of edges available.

The samples have been obtained adapting some recipes found in literature ([45, 42, 46]) with the capability of the available furnace.

Sample T02

The first recipe is the one described in Ref. [46], adapted as reported in Table 4.2:

Temperature:	1000 $^{\circ}C$
Gas flow:	H_2 10 *sccm*
	CH_4 30 *sccm*
Pressure:	$\approx$ 1 *Torr*
Time:	210 *min*

Table 4.2: Sample T02 growth recipe.

Heating and annealing process are the same as in the standard monolayer procedure, keeping an H_2 flow of 10 *sccm* during the all process. A graphical representation of the new process is shown in Figure 4.4.

Increasing the CH_4 flow from 5 *sccm* to 30 *sccm* the density of carbon atoms on the copper top surface increases. In the same way, increasing the growth time from 30 to 210 *min*, surface exposure to the methane flow increases. Thus, the presence of few layers graphene spots is expected. Furthermore, increasing the pressure increases the probability of the nucleation of few layers graphene [43].

An optical image of the sample obtained with this recipe, after the transfer on Si substrate, is shown in Figure 4.5.

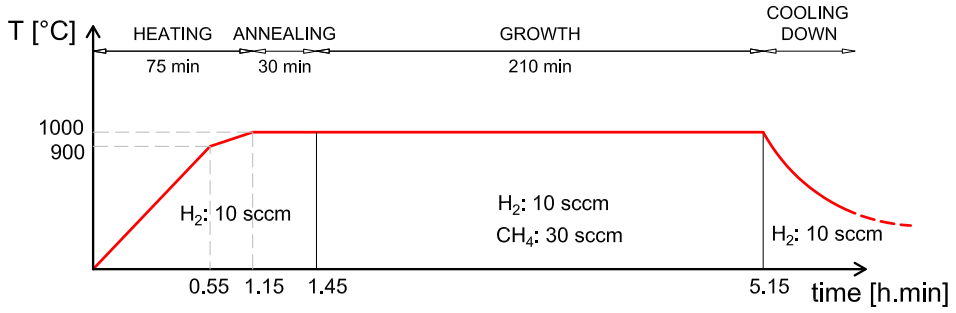

Figure 4.4: Sample T02. Time and temperature used to grow the graphene layer.

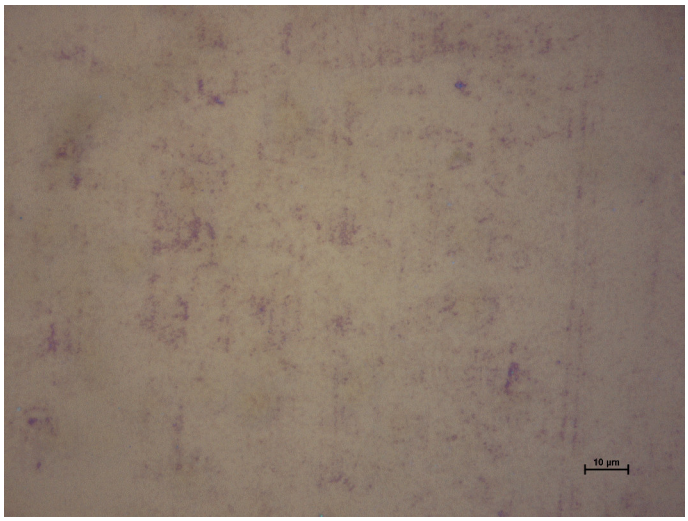

Figure 4.5: Sample T02. Optical image of graphene layers on $Si - SiO_2$ substrate, grown with the recipe described in Table 4.2.

The image 4.5 shows a light brown background with dark spots on top. There are regions with high concentration of dark spots randomly distributed, other with a more regular pattern and others with a much lower spot density. The spots size is less than $1\mu m$. The Raman analysis performed in different points of the light brown background of the sample (lower part of Figure 4.6) proves that it is single layer graphene. Instead, Raman spectrum of the dark spots (upper part of Figure 4.6) shows the typical configuration of a few layer graphene spectrum. This is consistent with the optical contrast as higher optical contrast is due to a higher number of layers (see section 3.2).

It is impossible to estimate the exact amount of layers: the surface is too heterogeneous to use only the optical contrast and the single spot is smaller than the area of the laser thus the spectrum is mediated on all the laser area (a superposition of single and few layers graphene).

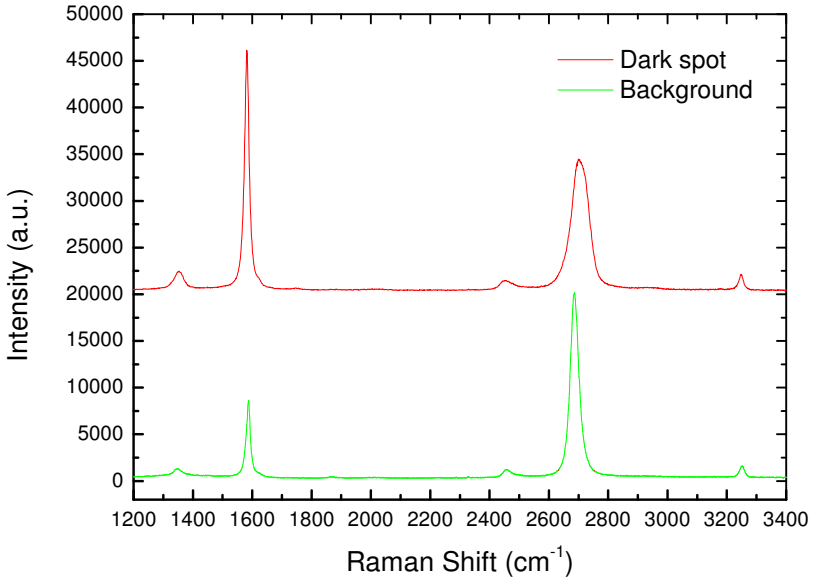

Figure 4.6: Sample T02. Raman spectra acquired with 514 nm wave length laser on $Si - SiO_2$ substrate. Surface grown with the recipe described in Table 4.2.

Sample T03

Another recipe has been developed starting from the process described in Ref. [45]. The growing parameters are itemized in Table 4.3:

Temperature:	1000 °C
Gas flow:	H_2 2 *sccm*
	CH_4 35 *sccm*
Pressure:	$\approx$ 1 *Torr*
Time:	120 *min*

Table 4.3: Sample T03 growth recipe.

Heating and annealing process are the same as in the previous recipes, keeping an H_2 flow of 2 *sccm* during the all process. A graphical representation of the new process is shown in Figure 4.7.

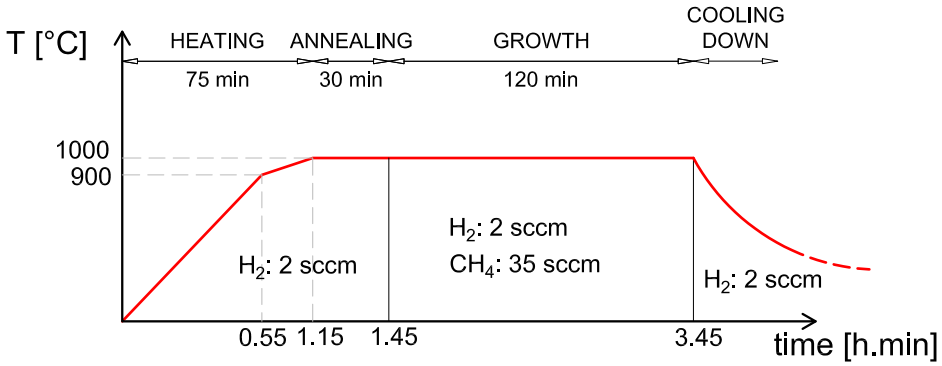

Figure 4.7: Sample T03. Time and temperature used to grow the graphene layer.

The CH_4:H_2 ratio is increased from 6:2 to 35:2 and the growth time is decreased from 210 to 120 *min*.

An optical image of the obtained sample after the transfer is shown in Figure 4.8.

The image shows again a light brown background with dark spots randomly distributed on the surface. The spots distribution is more homogeneous, but their dimension is still small and with varying thickness. Raman analysis proves that the light brown part is again a monolayer

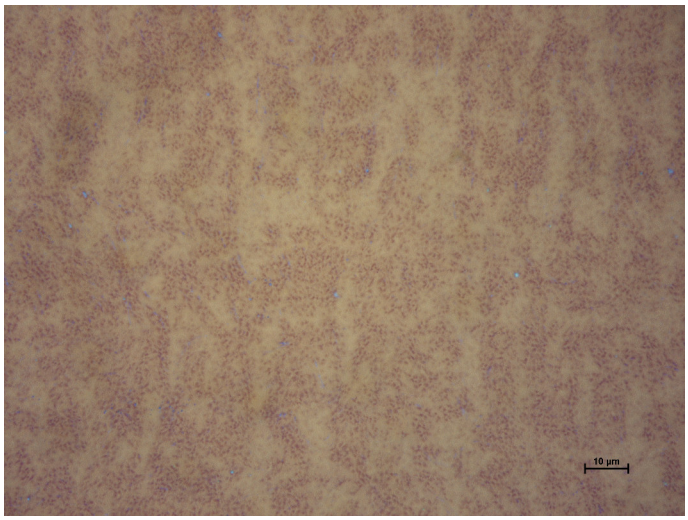

Figure 4.8: Sample T03. Optical image of graphene layers on $Si - SiO_2$ substrate, grown with the recipe described in Table 4.3.

graphene, while the dark spots are composed of few layers. Figure 4.9 shows spectra of light brown points and dark spots. Also in this case the spots are smaller than the area of the laser used for the Raman analysis, thus the spectrum is a superposition of single and few layers graphene.

Sample T04

The growth parameters used in the following recipe are reported in Table 4.4:

Temperature:	1000 $^{\circ}C$
Gas flow:	H_2 2 *sccm*
	CH_4 35 *sccm*
Pressure:	$\approx$ 1 *Torr*
Time:	210 *min*

Table 4.4: Sample T04 growth recipe.

The only difference with the previous one is the growth time (increased from 120 to 210 *min*). A graphical representation of the process is shown in Figure 4.10.

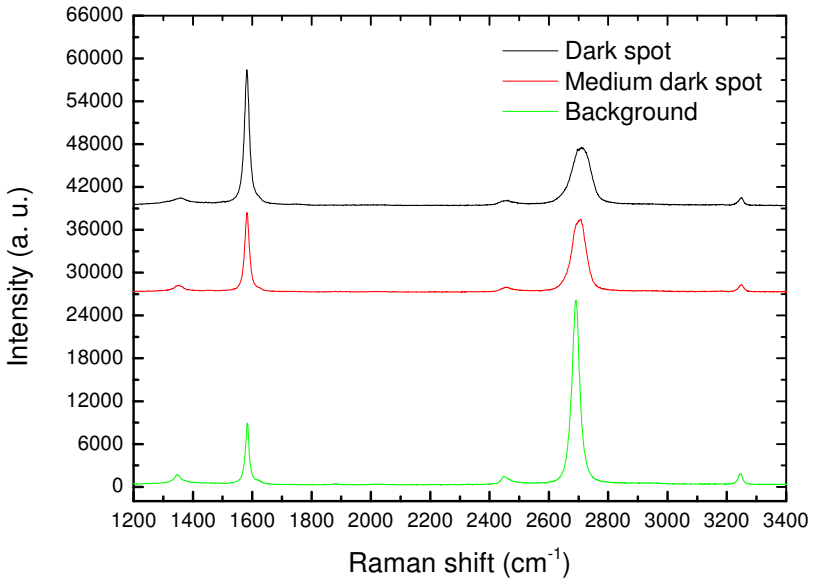

Figure 4.9: Sample T03. Raman spectra acquired with 514 nm wave length laser on $Si - SiO_2$ substrate. Surface grown with the recipe described in Table 4.3.

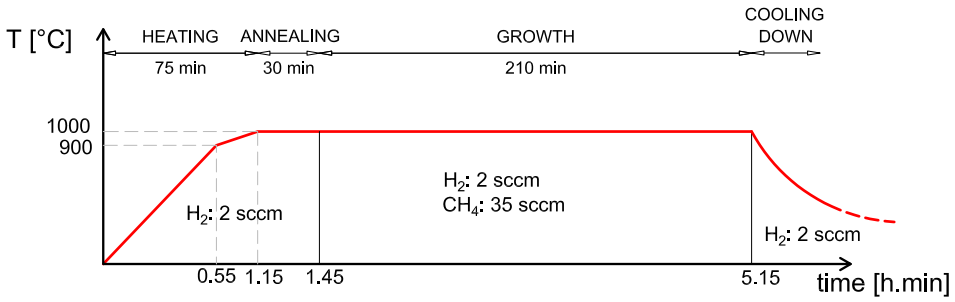

Figure 4.10: Sample T04. Time and temperature used to grow the graphene layer.

As a consequence, an increase of the spots size is expected. An optical image of the obtained surface after the transfer is shown in Figure 4.11.

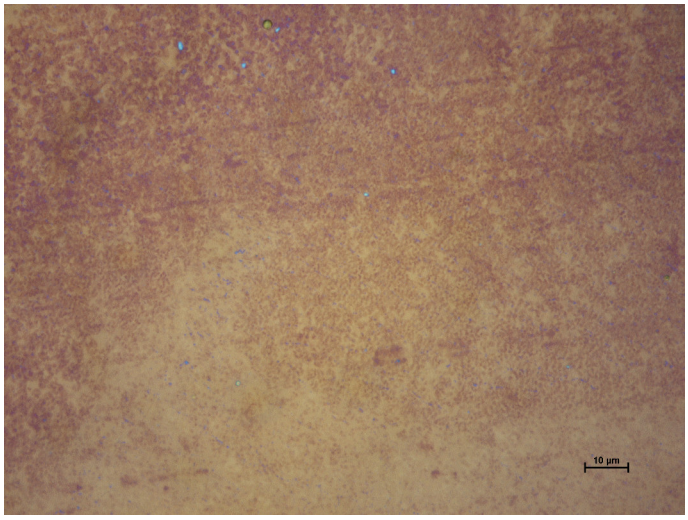

Figure 4.11: Sample T04. Optical image of graphene layers on $Si - SiO_2$ substrate, grown with the recipe described in Table 4.4.

The sample shows dark spots of the same dimension, but with an enhancement in their density. The light brown background is still visible, even if completely covered by dark spots distributed with a lower homogeneity than the previous case. Local regions with different colours are visible, the darker is the region the higher is the number of layers. Raman analysis shows the presence of few layer graphene everywhere. The spots density is too high to focus the laser only on the light brown background, thus the spectrum is a superposition of single and few layers graphene. Figure 4.12 shows different spectra of the surface. In the darker regions spectrum the 2D peak is larger, as expected in a few layers graphene. Furthermore, the D peak is broad, indicating the presence of amorphous carbon. Not all the carbon has been bonded to give the sp_2 structure of graphene, some atoms are deposited on the surface with a random structure.

Sample T05

Different examples in literature show that multi-layer graphene can be grown increasing the pressure in the chamber from hundreds of *mTorr* to hundreds of *Torr* [43, 42, 38].

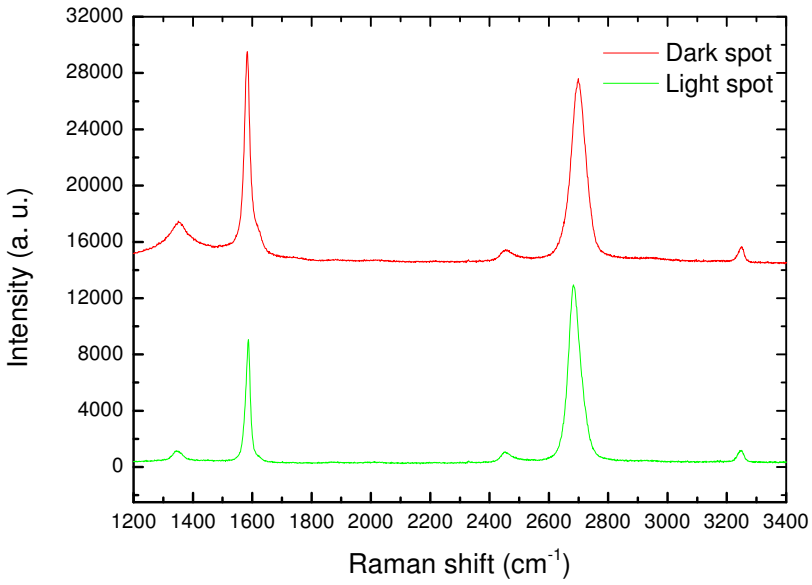

Figure 4.12: Sample T04. Raman spectra acquired with 514 nm wave length laser on $Si - SiO_2$ substrate. Surface grown with the recipe described in Table 4.4.

This furnace has been designed for growing monolayer graphene, therefore it has a good control on pressure in the range of *mTorr*, with a fixed velocity pump and a fine regulation valve. The maximum change due to the valve position is only few percentage of the plateau level, thus the only way to rise the pressure up to tens of *Torr* is to perform the growth in an inert atmosphere of argon.

The first recipe has been developed starting from the process described in Ref. [42]. Temperature and gases flow follow the recipe used to grow bilayer graphene. The pressure value in the chamber is obtained as a consequence from those parameters.

The growing parameters are itemized in Table 4.5:

Temperature:	940 $^{\circ}C$
Gas flow:	Ar 300 *sccm*
	H_2 30 *sccm*
	CH_4 10 *sccm*
Pressure:	$\approx$ 7 *Torr*
Time:	5 *min*

Table 4.5: Sample T05 growth recipe.

The chamber is heated directly to 940 $^{\circ}C$ in 75 *min*, followed by 30 *min* of annealing. Argon starts to flow with H_2 from the beginning. A graphical representation of the process is shown in Figure 4.13.

In order to increase the final amount of carbon on the surface, some changes have been applied also to the cooling down procedure. Once the growth step is completed, the heater is switched off but it is not moved aside as in the previous cases. Thus, the temperature decrease slowly.

An optical image of the obtained surface after the transfer is shown in Figure 4.14.

The result is not as expected and the surface is inhomogeneous. The Raman spectrum of the light brown background, shown in the lower part of Figure 4.15, has a really low intensity with a very high D peak. From this signal it is possible to infer the nature of the deposited material: not a continuous graphene layer but few graphene spots surrounded by

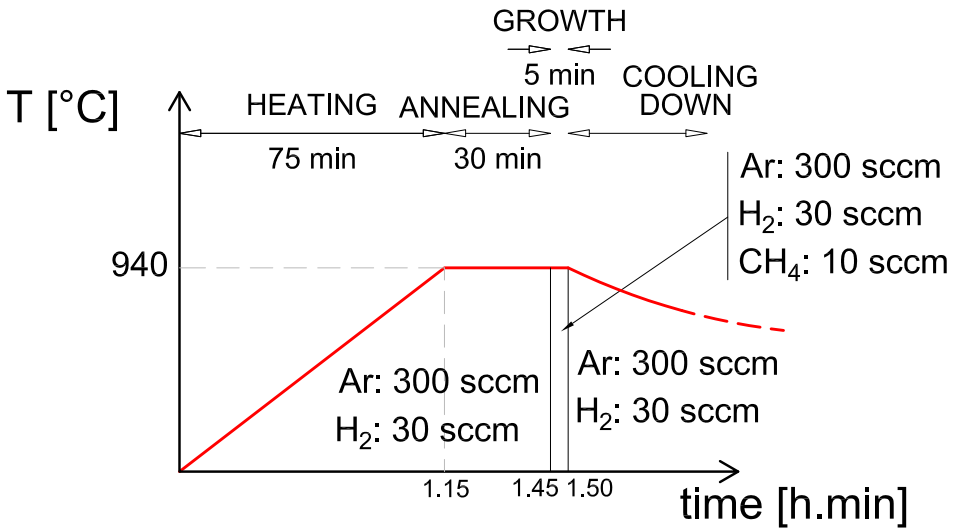

Figure 4.13: Sample T05. Time and temperature used to grow the graphene layer.

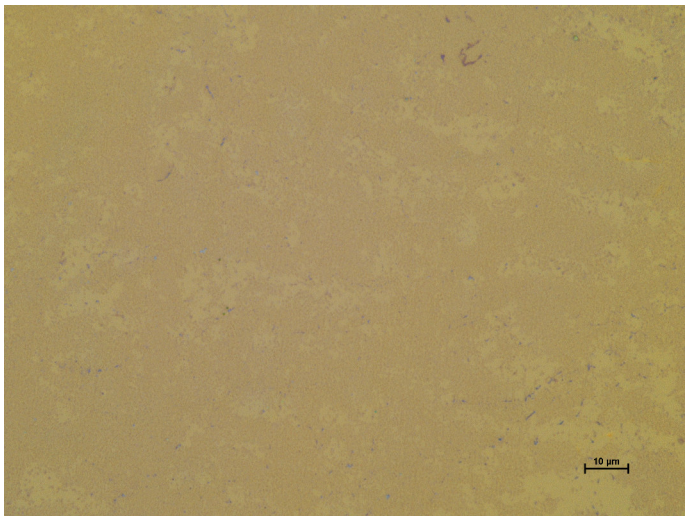

Figure 4.14: Sample T05. Optical image of graphene layers on $Si - SiO_2$ substrate, grown with the recipe described in Table 4.5.

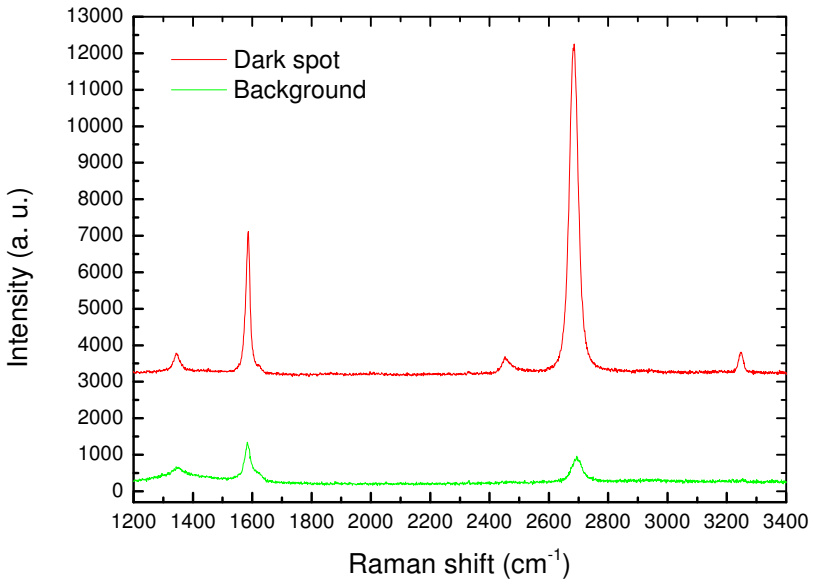

Figure 4.15: Sample T05. Raman spectra acquired with 514 nm wave length laser on $Si - SiO_2$ substrate. Surface grown with the recipe described in Table 4.5.

amorphous carbon. The brown spots (upper part of Figure 4.15) are single graphene layers.

Sample T06

In the following recipe, temperature and CH_4:H_2 gases ratio are kept at the same level as before while the Ar flow is increased in order to reach the pressure used in Ref. [42] to grow bilayer.

The resultant recipe has the parameters itemized in Table 4.6:

Temperature:	940 $^{\circ}C$
Gas flow:	Ar 600 *sccm*
	H_2 30 *sccm*
	CH_4 10 *sccm*
Pressure:	$\approx$ 11 *Torr*
Time:	5 *min*

Table 4.6: Sample T06 growth recipe.

Heating, annealing and cooling down are kept as in sample T05. A graphical representation of the process is shown in Figure 4.16.

An optical image of the obtained surface after the transfer is shown in Figure 4.17.

The surface grown is again not as expected. A single layer of graphene is grown on the surface but a lot of holes are visible. Raman analysis proves the absence of graphene in the lighter part of the surface and the presence of a high defected single layer in the other part. Figure 4.18 shows the spectrum of the part with graphene: a really pronounced D peak is visible.

Different reasons have been identified as causes of the surface weakness. First at all, the argon atoms flowing in the chamber wear away the surface. Few layers graphene growth is enhanced, due to the higher pressure, but part of the carbon is subsequently removed from the surface. The resulting surface is not compact and it is easily damageable. Furthermore, the temperature used in these last two recipes is lower. This implies a reduced catalytic activity of the surface and thus a reduction in the growth rate.

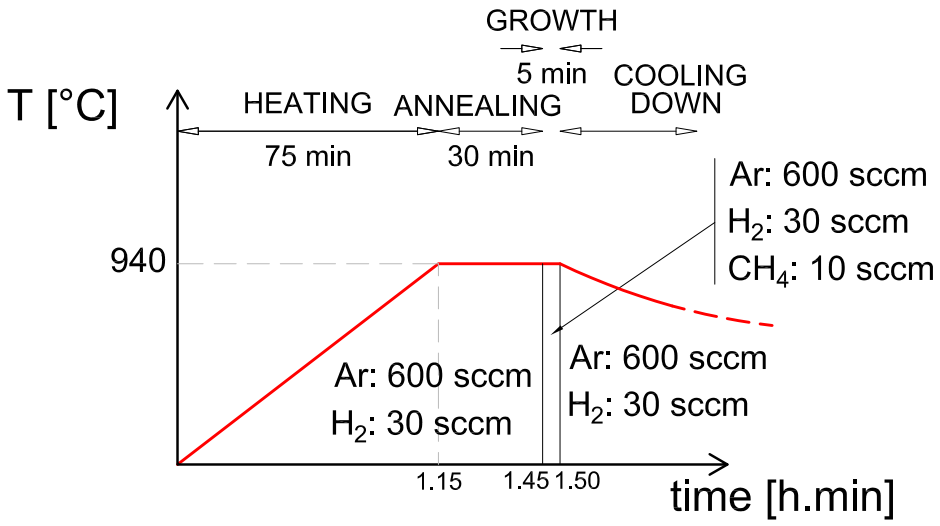

Figure 4.16: Sample T06. Time and temperature used to grow the graphene layer.

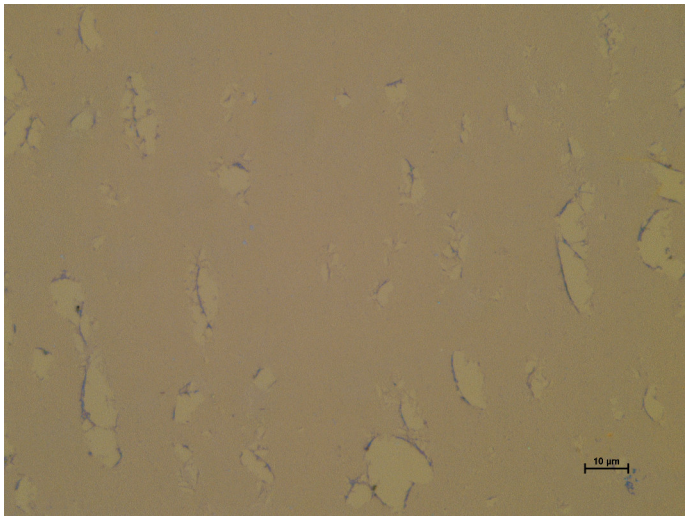

Figure 4.17: Sample T06. Optical image of graphene layers on $Si - SiO_2$ substrate, grown with the recipe described in Table 4.6.

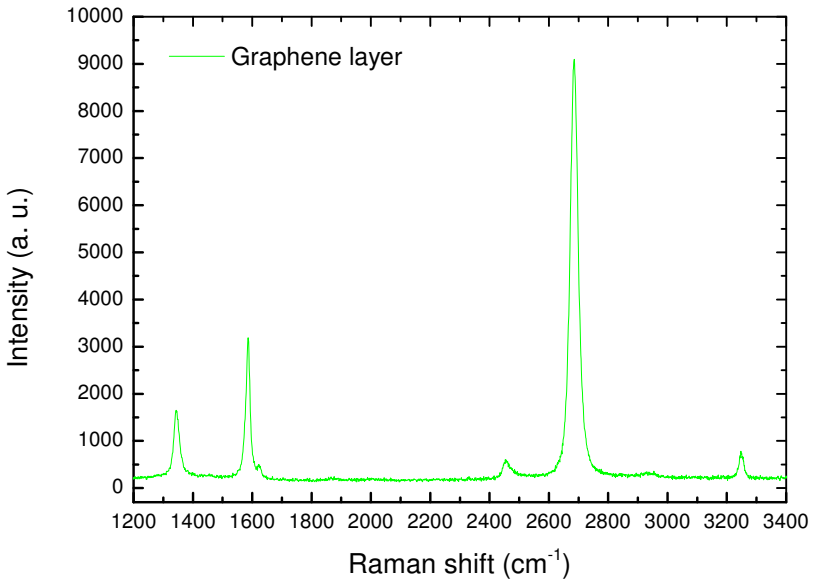

Figure 4.18: Sample T06. Raman spectrum acquired with 514 nm wave length laser on $Si - SiO_2$ substrate. Surface grown with the recipe described in Table 4.6.

Sample T07

The next recipe uses the parameter taken from Ref. [42] but with a final temperature increased from 940 $^{\circ}C$ to 1000 $^{\circ}C$.

The parameters are itemized in Table 4.7:

Temperature:	1000 $^{\circ}C$
Gas flow:	Ar 300 *sccm*
	H_2 30 *sccm*
	CH_4 10 *sccm*
Pressure:	$\approx$ 7 *Torr*
Time:	5 *min*

Table 4.7: Sample T07 growth recipe.

A graphical representation of the process is shown in Figure 4.19. Figure 4.20 shows the optical image of the resultant growth.

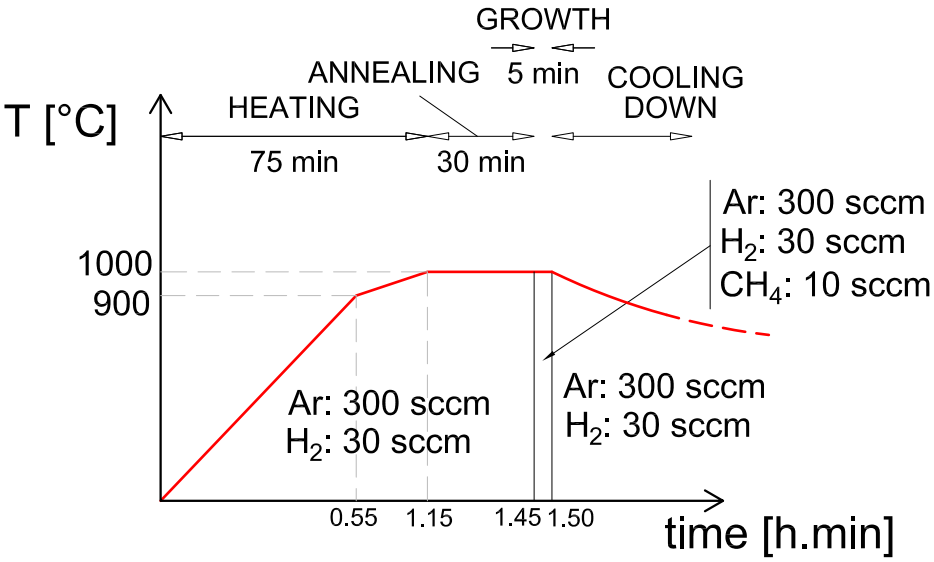

Figure 4.19: Sample T07. Time and temperature used to grow the graphene layer.

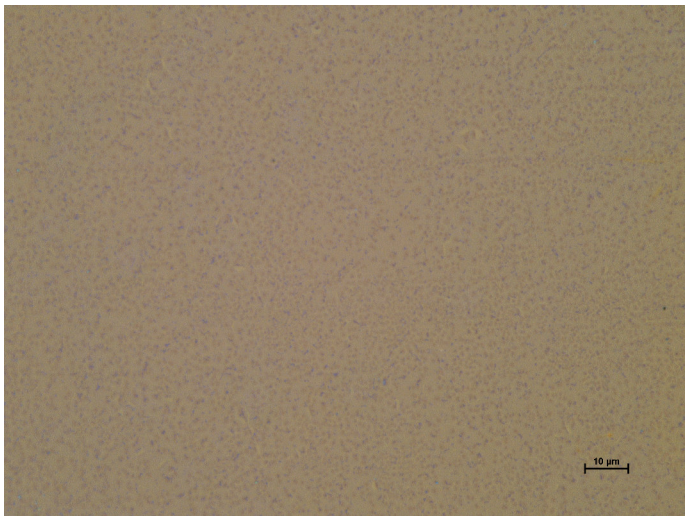

Figure 4.20: Sample T07. Optical image of graphene layers on $Si - SiO_2$ substrate, grown with the recipe described in Table 4.7.

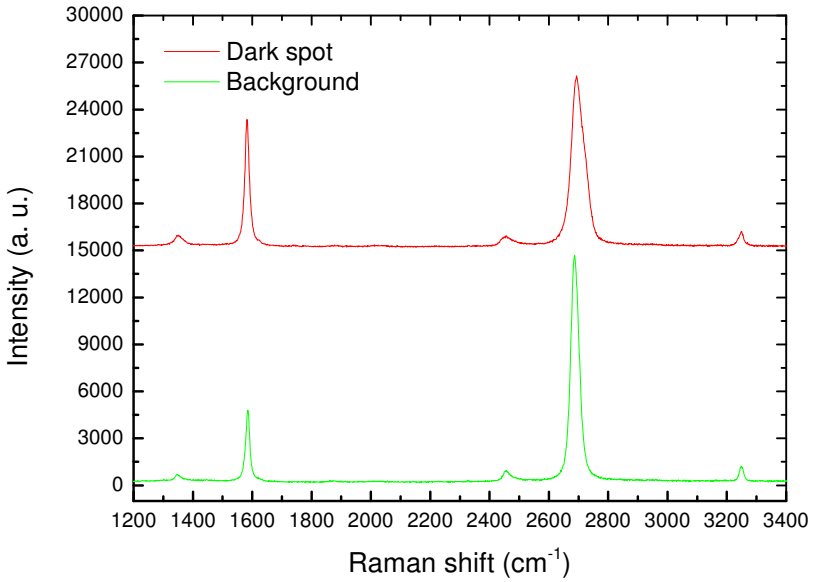

Figure 4.21: Sample T07. Raman spectra acquired with 514 nm wave length laser on $Si - SiO_2$ substrate. Surface grown with the recipe described in Table 4.7.

The higher temperature changed completely the result. A homogeneous single layer graphene completely covers the surface, and presents few dark spots on top. The spot size is higher than the previous one and the colour is more homogeneous. Raman spectra on the lighter and the darker part are shown in Figure 4.21.

Sample T08

In this recipe has been used the CH_4:H_2 gases ratio suggested by Ref. [45], as in sample T03, adding an argon flow to increase the pressure. The growing parameters are itemized in Table 4.8:

Temperature:	1000 $^{\circ}C$
Gas flow:	Ar 300 *sccm*
	H_2 2 *sccm*
	CH_4 35 *sccm*
Pressure:	$\approx$ 7 *Torr*
Time:	30 *min*

Table 4.8: Sample T08 growth recipe.

Heating, annealing and cooling down are kept as in sample T03. A graphical representation of the process is shown in Figure 4.22.

Figure 4.23 shows the optical image of the graphene obtained.

The surface looks compact and completely covered with a single layer graphene. Uniformly distributed spots, with the presence of only few darker regions, are visible on top of it. Figure 4.24 shows the different Raman spectra of the surface.

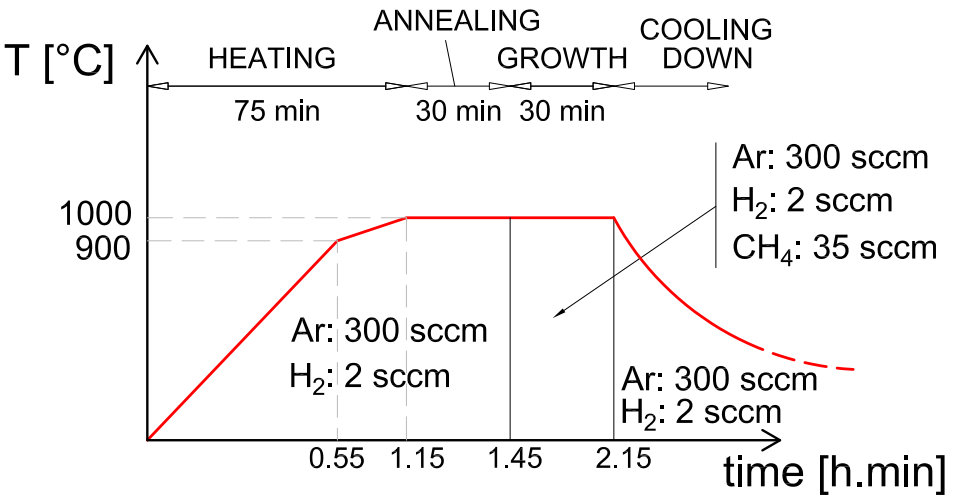

Figure 4.22: Sample T08. Time and temperature used to grow the graphene layer.

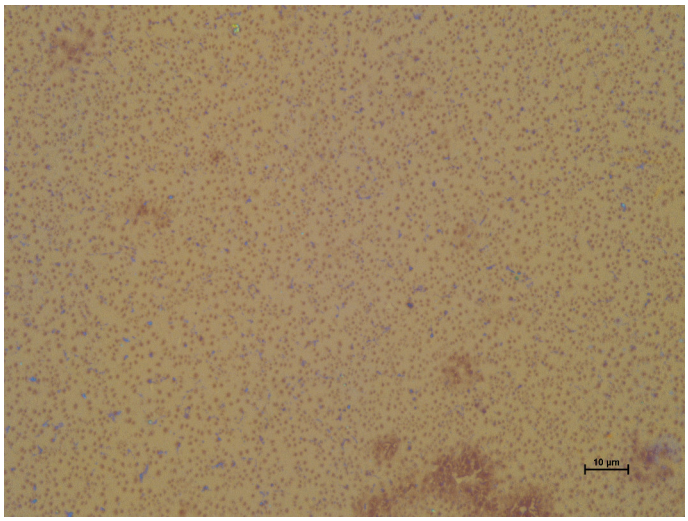

Figure 4.23: Sample T08. Optical image of graphene layers on $Si - SiO_2$ substrate, grown with the recipe described in Table 4.8.

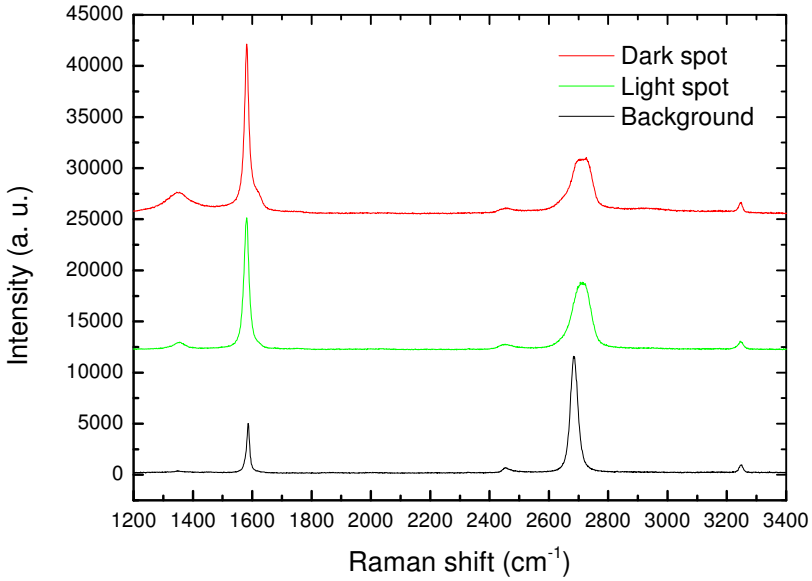

Figure 4.24: Sample T08. Raman spectra acquired with 514 nm wave length laser on $Si - SiO_2$ substrate. Surface grown with the recipe described in Table 4.8.

4.1.3 Conclusions

Among the developed recipes, sample T07 and sample T08 provide the best material for sensing applications. Both have a homogeneous single layer graphene partially covered with few layers graphene flakes with a size of about $1\mu m$.

In this way, the top layer shows large amount of edges which are chemically reactive and are preferential sites for functionalization while the bottom continuous layer ensures electrical conductivity, essential for sensing applications.

A surface with high heterogeneity of course can lead to an even higher surface area, but at the cost of disturbing the properties of the single layer. Furthermore, the higher is the heterogeneity of surface the higher is the properties variability inside the sample.

Although CVD graphene is intrinsically heterogeneous, a material as

more homogeneous as possible is required to perform the characterization steps. For those reasons, the sample T07 is preferred to T08, since it shows a higher homogeneity on both spatial distribution and thickness of the flakes.

4.2 Electrical measurements results

Once optimal growing conditions have been identified, the optimized material has been integrated into field-effect transistors. For comparison, both ”standard” (Sample T01) and optimized (Sample T07) graphene have been investigated.

The electrical measurements have been performed with a Lake Shore CRX-VF probe station. It has a closed chamber with a control system for pressure and temperature, and six ultra stable micromanipulated probe arms, each providing precise 3-axis control to land the probe tips accurately on the device. A picture of the chamber open with the sketch of the vertical section is shown in Figure 4.25.

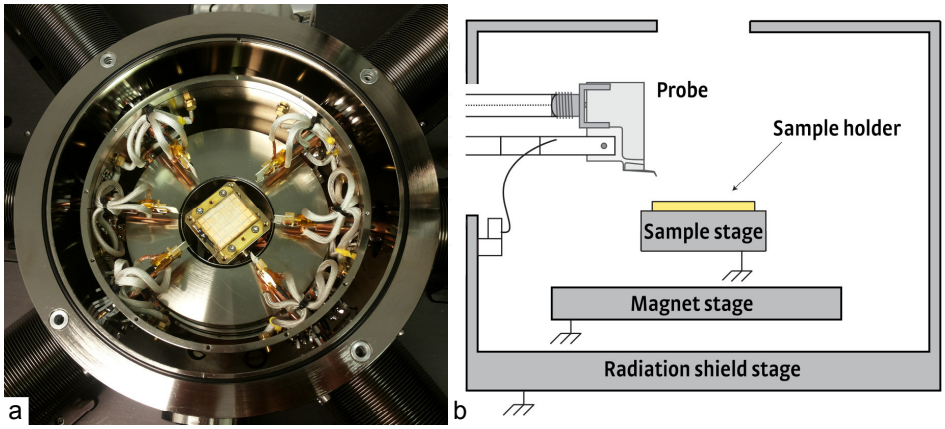

Figure 4.25: CRX-VF probe station. a) View of the chamber open. Six ultra stable micromanipulated probe arms are placed around the sample holder. b) Sketch of the vertical section of the chamber.

The samples have been placed on the sample holder and fixed on it using silver paint (a metallic paste that once deposited creates a conductive surface). The silver paint fixes the sample on the plate but also electrically connects the substrate to the plate, allowing the Si to be used as back gate

for the I-V measurements. Then the chamber is closed and pumped down.

The measurements are done at a temperature of 25 $°C$ and pressure of $10^{-6}\,mbar$. An annealing, consisting of heating the chamber up to a temperature of 100 $°C$ for 4 hours, is performed to allow the samples to release the moisture that might be present on them. The I-V measurements are performed on "standard" and optimized graphene both before and after the annealing procedure. Since the water molecules can act as doping agent, a change in the trans-characteristic is expected.

Figure 4.26 shows the tips arrangement to perform the measurements. On the left the two-probe setting and on the right the four-probe setting (the two setups have been described in section 3.5).

In the two-probe arrangement the two tips are placed on two pads connected to two adjacent contacts, in order to apply voltage to a single channel for every measure. The same arrangement is used also for the TLM devices.

In the four-probe one, the tips are placed on the pads to control four adjacent contacts. The current is injected via the outer electrodes (Force) and the potential is measured via the inner ones (Sense).

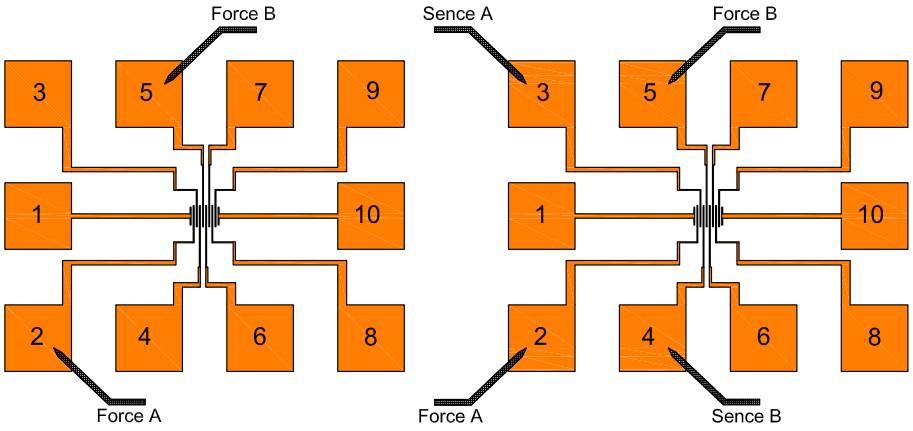

Figure 4.26: Sketches of the tips arrangements to perform the measurements. Left) two-probe arrangement: the two tips are placed on two pads connected to two adjacent contacts. Right) four-probe arrangement: four tips are placed on the pads to control four adjacent contacts. The current is injected via the outer electrodes (Force) and the potential is measured via the inner ones (Sense).

In the two-probe and the four-probe measurements the input signal is an increasing voltage between the forcing probes from 0 to $10\,mV$ and the current is measured and stored.

The graphene behaves as a resistor: the current-voltage characteristic is a straight line. The resistance can be obtained as the inverse of the slope of the curve; this is the total resistance of the structure R_{tot} for the two-probe configuration and the resistance of the channel R_{gr} for the four-probe one.

Different channels of different devices have been characterised with those techniques. Once the curves have been obtained, the two-probe and the four-probe measures on the same contacts have been plotted on a graph and the data have been analysed with a Matlab script to fit the curves (linear fit). The contact resistance R_c and the unit length contact resistance R_{uc} have been calculated according Eq. 3.8 and Eq. 3.10. An example of the plots is shown in Figure 4.27.

The sheet resistance R_s is then extracted from the four-probe measurements inverting Eq. 3.7:

$$R_s = R_{gr}\,\frac{w}{L} \tag{4.1}$$

where L and w are the length and the width of the graphene channel (respectively $5\,\mu m$ and $40\,\mu m$).

Tables 4.9 and 4.10 show all the data extracted respectively on samples T01 and T07.

The TLM measurements use the same configuration of the two-probe one, with the two tips placed systematically on all the different adjacent contacts to measure the resistance of all the graphene channels with increasing length. A voltage from 0 to $10\,mV$ has been applied and the current has been measured. The data have then been analysed with a Matlab script to extract the inverse of the slope (the total resistance R_{tot}) with a liner fit. The resistances are then plotted together versus the length of the channels and the contact resistance R_c has been extracted as explained in section 3.5.2.

Figure 4.28 shows the resistance versus the channel length of one of the devices. As can be seen, a linear fitting is not appropriate for this set of data. Analysing the resistance of the channels R_{gr} in Tables 4.9 and 4.10 a difference up to $200\,\Omega$ between adjacent channels can be noticed.

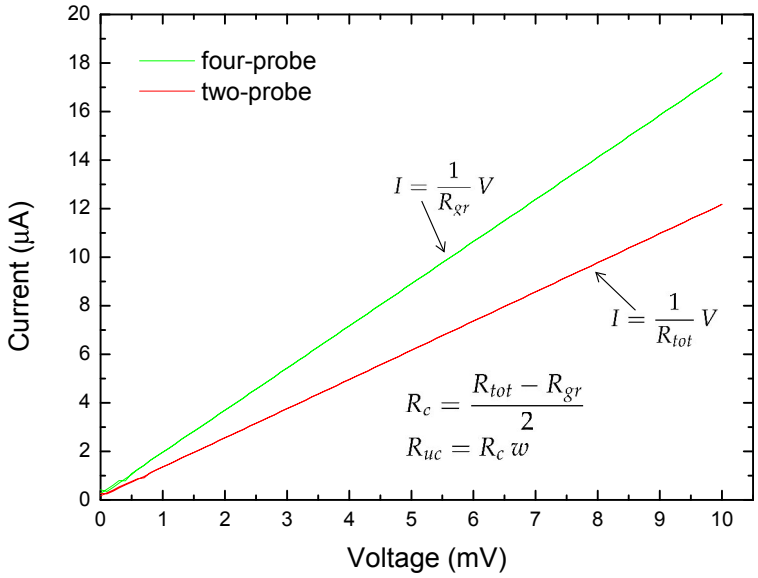

Figure 4.27: Graphical representation of two-probe and four-probe measurements between two contacts: the inverse of the slope of the two-probe measure (the lowest curve) is the total resistance R_{tot}, the inverse of the slope of the four-probe measure (the highest curve) is the resistance of the channel R_{gr}. The contact resistance R_c and the unit length contact resistance R_{uc} can be calculated according Eq. 3.8 and Eq. 3.10.

DEVICE 1d	contacts 3 - 4		contacts 5 - 6		contacts 7 - 8	
	before annealing	*after annealing*	*before annealing*	*after annealing*	*before annealing*	*after annealing*
R_{tot} (Ω)	2145	4032	1987	4585	3124	6763
R_{gr} (Ω)	201	507,7	175	496,1	186	822,1
R_c (Ω)	972	1762,15	906	2044,45	1469	2970,45
R_{uc} ($\Omega\ \mu m$)	38880	70486	36240	81778	58760	118818
R_s (Ω/sq)	1608	4061,6	1400	3968,8	1488	6576,8
DEVICE 2d	contacts 3 - 4		contacts 5 - 6		contacts 7 - 8	
	before annealing	*after annealing*	*before annealing*	*after annealing*	*before annealing*	*after annealing*
R_{tot} (Ω)	1987	4652	2087	6044	2143	6419
R_{gr} (Ω)	254	573,4	297	589,9	194	497,5
R_c (Ω)	866,5	2039,3	895	2727,05	974,5	2960,75
R_{uc} ($\Omega\ \mu m$)	34660	81572	35800	109082	38980	118430
R_s (Ω/sq)	2032	4587,2	2376	4719,2	1552	3980
DEVICE 2f	contacts 3 - 4		contacts 5 - 6		contacts 7 - 8	
	before annealing	*after annealing*	*before annealing*	*after annealing*	*before annealing*	*after annealing*
R_{tot} (Ω)	1982	5874	2710	5906	3346	7981
R_{gr} (Ω)	187,6	598	176,1	609,8	196,2	662,6
R_c (Ω)	897,2	2638	1266,95	2648,1	1574,9	3659,2
R_{uc} ($\Omega\ \mu m$)	35888	105520	50678	105924	62996	146368
R_s (Ω/sq)	1500,8	4784	1408,8	4878,4	1569,6	5300,8
DEVICE 2i	contacts 3 - 4		contacts 5 - 6		contacts 7 - 8	
	before annealing	*after annealing*	*before annealing*	*after annealing*	*before annealing*	*after annealing*
R_{tot} (Ω)	2456	5433	1608	3059	1651	3166
R_{gr} (Ω)	235	417,5	206,8	1287	210,8	494,1
R_c (Ω)	1110,5	2507,75	700,6	886	720,1	1335,95
R_{uc} ($\Omega\ \mu m$)	44420	100310	28024	35440	28804	53438
R_s (Ω/sq)	1880	3340	1654,4	10296	1686,4	3952,8
DEVICE 4b	contacts 3 - 4		contacts 5 - 6		contacts 7 - 8	
	before annealing	*after annealing*	*before annealing*	*after annealing*	*before annealing*	*after annealing*
R_{tot} (Ω)	2097	4096	2176	4962	1976	4228
R_{gr} (Ω)	187	409,5	199	447,3	168	459,8
R_c (Ω)	955	1843,25	988,5	2257,35	904	1884,1
R_{uc} ($\Omega\ \mu m$)	38200	73730	39540	90294	36160	75364
R_s (Ω/sq)	1496	3276	1592	3578,4	1344	3678,4
DEVICE 4d	contacts 3 - 4		contacts 5 - 6		contacts 7 - 8	
	before annealing	*after annealing*	*before annealing*	*after annealing*	*before annealing*	*after annealing*
R_{tot} (Ω)	1867	3616	2243	4787	3265	8416
R_{gr} (Ω)	164	397,9	203	489,2	234	615,3
R_c (Ω)	851,5	1609,05	1020	2148,9	1515,5	3900,35
R_{uc} ($\Omega\ \mu m$)	34060	64362	40800	85956	60620	156014
R_s (Ω/sq)	1312	3183,2	1624	3913,6	1872	4922,4

Table 4.9: Sample T01. Data extracted from the two-probe and the four-probe measurements.

DEVICE 3b	contacts 3 - 4		contacts 5 - 6		contacts 7 - 8	
	before annealing	*after annealing*	*before annealing*	*after annealing*	*before annealing*	*after annealing*
R_{tot} (Ω)	956	1294	740	927	724	941,8
R_{gr} (Ω)	690	1078	532	700,6	523	710,3
R_{c} (Ω)	133	108	104	113,2	100,5	115,75
R_{uc} ($\Omega\,\mu m$)	5320	4320	4160	4528	4020	4630
R_{s} (Ω/sq)	5520	8624	4256	5604,8	4184	5682,4
DEVICE 3d	contacts 3 - 4		contacts 5 - 6		contacts 7 - 8	
	before annealing	*after annealing*	*before annealing*	*after annealing*	*before annealing*	*after annealing*
R_{tot} (Ω)	881,7	1031	928,8	1265	1039	1314
R_{gr} (Ω)	593,5	754,4	792,4	1015	790,5	1037
R_{c} (Ω)	144,1	138,3	68,2	125	124,25	138,5
R_{uc} ($\Omega\,\mu m$)	5764	5532	2728	5000	4970	5540
R_{s} (Ω/sq)	4748	6035,2	6339,2	8120	6324	8296
DEVICE 3f	contacts 3 - 4		contacts 5 - 6		contacts 7 - 8	
	before annealing	*after annealing*	*before annealing*	*after annealing*	*before annealing*	*after annealing*
R_{tot} (Ω)	721	901,1	750	935,2	712	887,1
R_{gr} (Ω)	512	635,8	543	687,1	531	624,3
R_{c} (Ω)	104,5	132,65	103,5	124,05	90,5	131,4
R_{uc} ($\Omega\,\mu m$)	4180	5306	4140	4962	3620	5256
R_{s} (Ω/sq)	4096	5086,4	4344	5496,8	4248	4994,4
DEVICE 3i	contacts 3 - 4		contacts 5 - 6		contacts 7 - 8	
	before annealing	*after annealing*	*before annealing*	*after annealing*	*before annealing*	*after annealing*
R_{tot} (Ω)	831,7	1096	806,9	1299	1246	1432
R_{gr} (Ω)	576,1	769,1	534,7	766,1	708,8	965
R_{c} (Ω)	127,8	163,45	136,1	266,45	268,6	233,5
R_{uc} ($\Omega\,\mu m$)	5112	6538	5444	10658	10744	9340
R_{s} (Ω/sq)	4608,8	6152,8	4277,6	6128,8	5670,4	7720
DEVICE 4b	contacts 3 - 4		contacts 5 - 6		contacts 7 - 8	
	before annealing	*after annealing*	*before annealing*	*after annealing*	*before annealing*	*after annealing*
R_{tot} (Ω)	902	1159	894	1084	965	1180
R_{gr} (Ω)	689	890	652	857,6	654	884,1
R_{c} (Ω)	106,5	134,5	121	113,2	155,5	147,95
R_{uc} ($\Omega\,\mu m$)	4260	5380	4840	4528	6220	5918
R_{s} (Ω/sq)	5512	7120	5216	6860,8	5232	7072,8
DEVICE 4i	contacts 3 - 4		contacts 5 - 6		contacts 7 - 8	
	before annealing	*after annealing*	*before annealing*	*after annealing*	*before annealing*	*after annealing*
R_{tot} (Ω)	1003	1675	1176	1765	1043	1345
R_{gr} (Ω)	765	1329	801	1385	796	915,8
R_{c} (Ω)	119	173	187,5	190	123,5	214,6
R_{uc} ($\Omega\,\mu m$)	4760	6920	7500	7600	4940	8584
R_{s} (Ω/sq)	6120	10632	6408	11080	6368	7326,4

Table 4.10: Sample T07. Data extracted from the two-probe and the four-probe measurements.

Since the TLM measurement is based on the assumption that the different channels have the same properties except for the length, this method does not provide accurate results, although qualitatively correct.

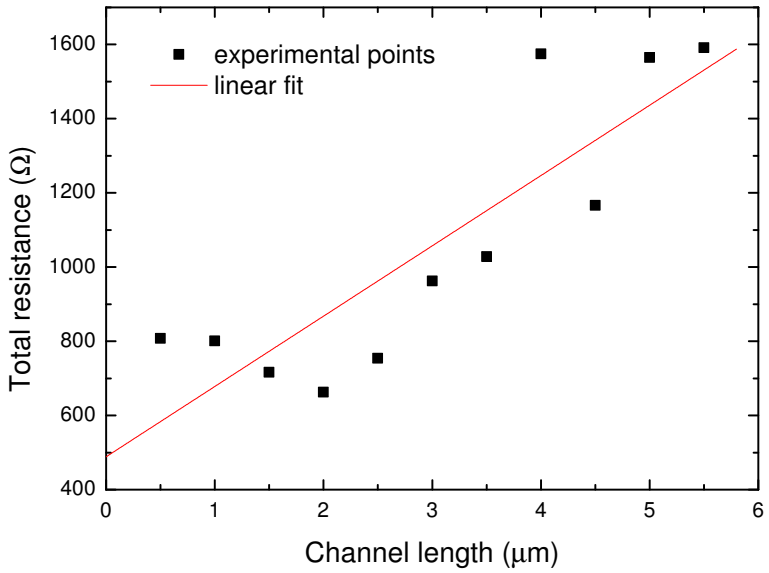

Figure 4.28: Graphical representation of a TML measurement. The total resistance on each channel is plotted versus the relative channel length. A linear fitting is not appropriate for this set of data. The TLM measurement is based on the assumption that the different channels have the same properties except for the length, while the resistance of adjacent channels in this case is quite different.

To measure the trans-characteristic and calculate the mobility of the devices a four-probe configuration has been used, in order to extract only the properties of the channel. The gate voltage has been applied controlling the potential between the sample holder (electrically connected to the silicon substrate through the silver paint) and the source tip. Three curves have been obtained for any channel, applying an increasing gate voltage V_G from $-40\,V$ to $40\,V$ with a constant source-drain voltage V_{DS} of $10\,mV$, $20\,mV$ and $30\,mV$. The plots of the current I_{DS} versus the gate voltage V_G of one measurement before and after the annealing are shown in Figure

4.29 for sample T01 and Figure 4.30 for sample T07.

In sample T01, before annealing (upper part of Figure 4.29) it is not possible to see the Dirac point. It is only visible the first part of the trans-characteristic. The reason is that the graphene, before annealing, is highly doped thus the Dirac point is shifted to higher voltage that could damage the silicon dioxide if reached.

The curves after annealing (lower part of Figure 4.29) instead show a main Dirac point at about 11-13 V but they present another shallow minimum at lower voltage. This is due to the doping inhomogeneity of the graphene in the channel that creates an overlap of different trans-characteristics associated to graphene zones with different properties [69].

In sample T07 (Figure 4.30) all the curves show the Dirac point. Before annealing it is shifted to higher voltage, since the doping level is higher.

The maximum field effect mobility is extracted from these plots using Eq. 3.11 reported here as well:

$$\mu_{FE} = \frac{\Delta I_{DS}}{\Delta V_G} \frac{L}{w\, C_{OX}\, V_{DS}} \tag{4.2}$$

The maximum slope of the $I_{DS} - V_G$ plot, $\frac{\Delta I_{DS}}{\Delta V_G}$, is calculated using a Matlab script and it is always located near the Dirac point. The drain voltage V_{DS} is $10\,mV$, $20\,mV$ or $30\,mV$ according the measurement. The length of the channel is $L = 5\,\mu m$ and its width is $w = 40\,\mu m$. The gate capacitance per unit area is $C_{OX} = 12.12\,nF/cm^2$ considering a vacuum permittivity ϵ_0 of $8.854 \cdot 10^{12} F/m$, a relative permittivity of the SiO_2 ϵ_r of 3.9 and a thickness of the SiO_2 d of $285\,nm$.

The data extracted from different devices on both samples are shown in Table 4.11 and Table 4.12.

The mobility has not been calculated in sample T01 before annealing since the curves obtained are too far from the Dirac point to extract the real maximum slope.

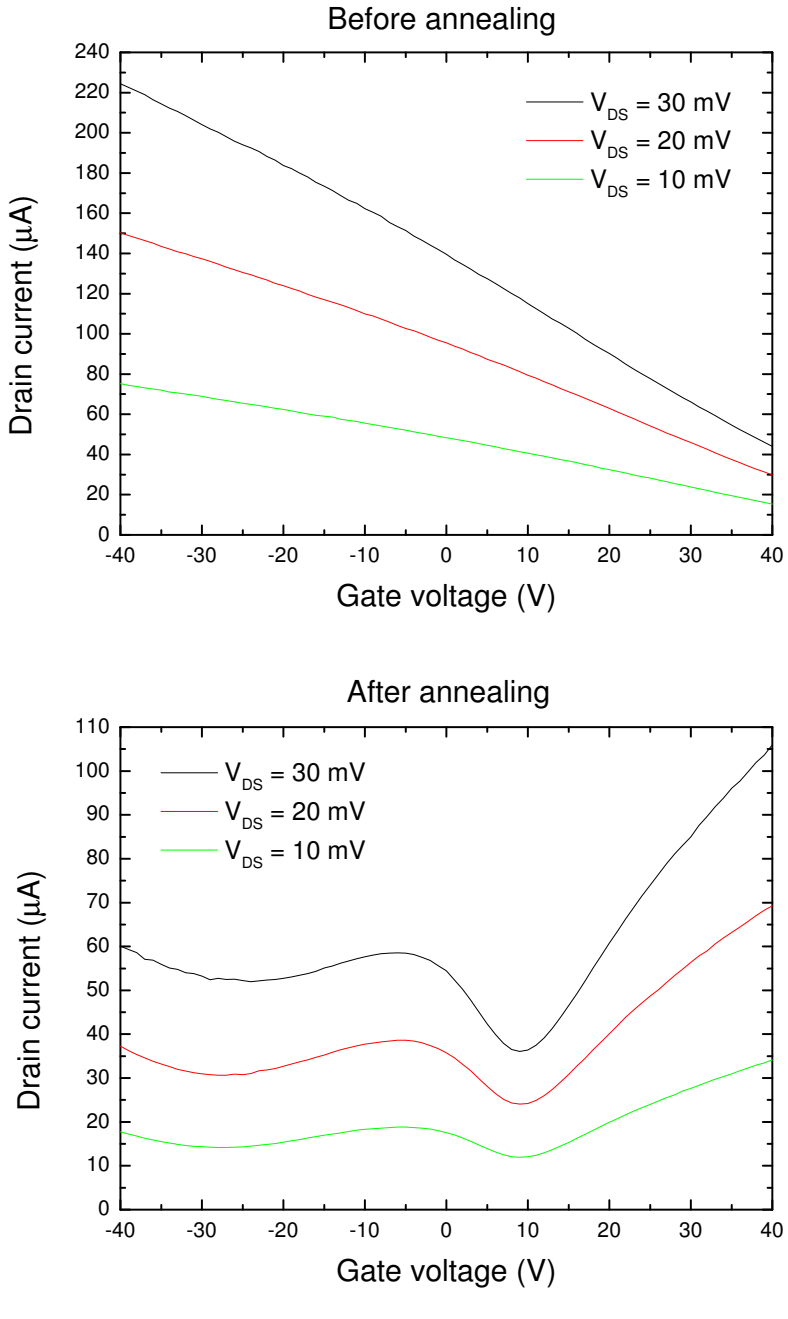

Figure 4.29: Sample T01: Graphical representation of a gate voltage dependent measurements on the "standard" graphene. Up) Current I_{DS} versus the gate voltage V_G measured before annealing. Only the first part of the transfer characteristic is visible, the Dirac point is located at voltage higher than 40 V. Down) Current I_{DS} versus the gate voltage V_G measured after annealing. All the transfer characteristic is visible, the Dirac point is located around 11-13 V.

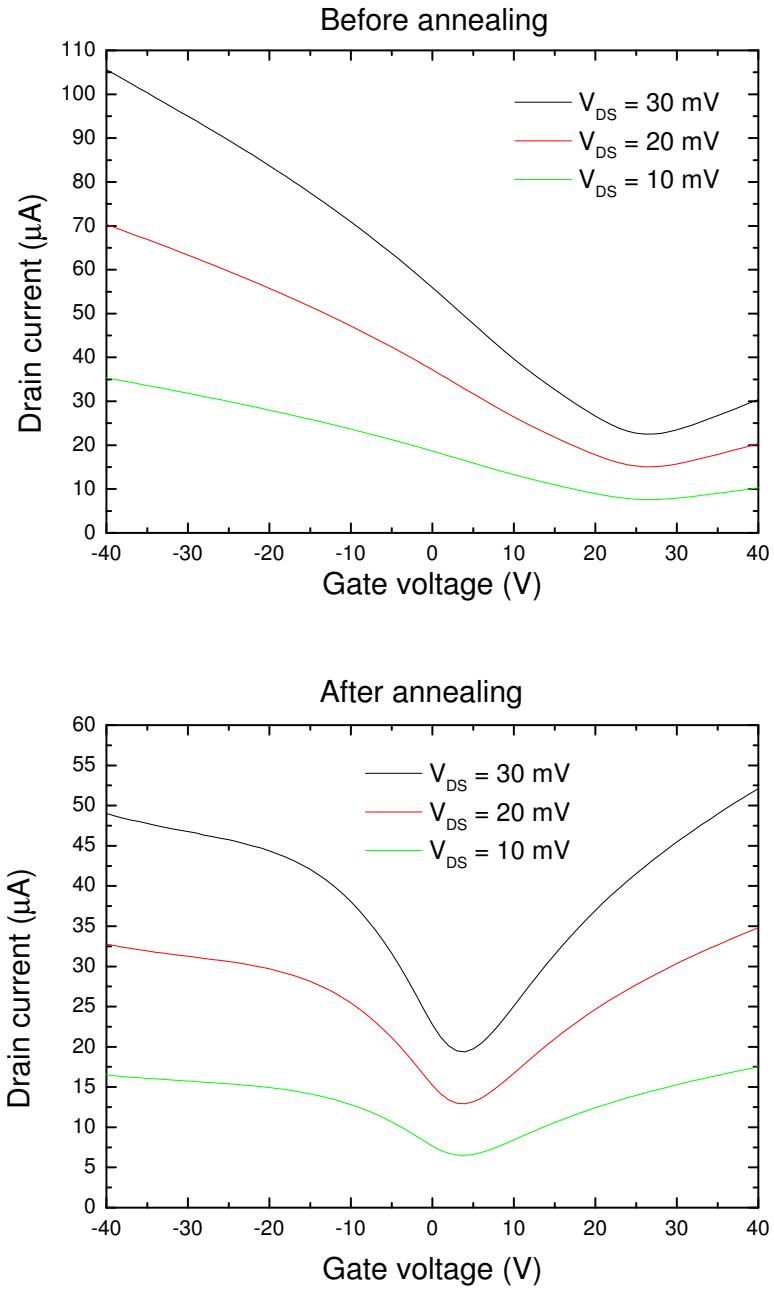

Figure 4.30: Sample T07: Graphical representation of a gate voltage dependent measurements on the optimized graphene. Up) Current I_{DS} versus the gate voltage V_G measured before annealing. The Dirac point is located at voltage around 27-30 V. Down) Current I_{DS} versus the gate voltage V_G measured after annealing. The Dirac point is located around 3-5 V.

DEVICE 1d	contacts 3 - 4		contacts 5 - 6		contacts 7 - 8	
before annealing	*Mobility* (cm^2/Vs)	*Dirac point position* (V)	*Mobility* (cm^2/Vs)	*Dirac point position* (V)	*Mobility* (cm^2/Vs)	*Dirac point position* (V)
V_{DS} = 10 mV	-	> 40	-	> 40	-	> 40
V_{DS} = 20 mV	-	> 40	-	> 40	-	> 40
V_{DS} = 30 mV	-	> 40	-	> 40	-	> 40
after annealing	*Mobility* (cm^2/Vs)	*Dirac point position* (V)	*Mobility* (cm^2/Vs)	*Dirac point position* (V)	*Mobility* (cm^2/Vs)	*Dirac point position* (V)
V_{DS} = 10 mV	1153	13	1179	13	861	12
V_{DS} = 20 mV	1222	13	1150	13	863	12
V_{DS} = 30 mV	1162	13	1157	13	874	12
DEVICE 2f	contacts 3 - 4		contacts 5 - 6		contacts 7 - 8	
before annealing	*Mobility* (cm^2/Vs)	*Dirac point position* (V)	*Mobility* (cm^2/Vs)	*Dirac point position* (V)	*Mobility* (cm^2/Vs)	*Dirac point position* (V)
V_{DS} = 10 mV	-	> 40	-	> 40	-	> 40
V_{DS} = 20 mV	-	> 40	-	> 40	-	> 40
V_{DS} = 30 mV	-	> 40	-	> 40	-	> 40
after annealing	*Mobility* (cm^2/Vs)	*Dirac point position* (V)	*Mobility* (cm^2/Vs)	*Dirac point position* (V)	*Mobility* (cm^2/Vs)	*Dirac point position* (V)
V_{DS} = 10 mV	905	13	844	13	810	11
V_{DS} = 20 mV	896	13	834	13	802	11
V_{DS} = 30 mV	901	13	887	13	860	11
DEVICE 4d	contacts 3 - 4		contacts 5 - 6		contacts 7 - 8	
before annealing	*Mobility* (cm^2/Vs)	*Dirac point position* (V)	*Mobility* (cm^2/Vs)	*Dirac point position* (V)	*Mobility* (cm^2/Vs)	*Dirac point position* (V)
V_{DS} = 10 mV	-	> 40	-	> 40	-	> 40
V_{DS} = 20 mV	-	> 40	-	> 40	-	> 40
V_{DS} = 30 mV	-	> 40	-	> 40	-	> 40
after annealing	*Mobility* (cm^2/Vs)	*Dirac point position* (V)	*Mobility* (cm^2/Vs)	*Dirac point position* (V)	*Mobility* (cm^2/Vs)	*Dirac point position* (V)
V_{DS} = 10 mV	1215	10	155	10	982	9
V_{DS} = 20 mV	1198	10	148	10	1011	9
V_{DS} = 30 mV	1198	10	148	10	1021	9

Table 4.11: Sample T01. Data extracted from the gate voltage dependent measurements: maximum mobility μ_{FE} extracted with Eq. 3.11 and Dirac point position.

DEVICE 3i	contacts 3 - 4		contacts 5 - 6		contacts 7 - 8	
before annealing	*Mobility* (cm^2/Vs)	*Dirac point position* (*V*)	*Mobility* (cm^2/Vs)	*Dirac point position* (*V*)	*Mobility* (cm^2/Vs)	*Dirac point position* (*V*)
V_{DS} = 10 *mV*	577	27	600	27	458	29
V_{DS} = 20 *mV*	572	27	602	28	452	29
V_{DS} = 30 *mV*	580	27	598	28	451	29
after annealing	*Mobility* (cm^2/Vs)	*Dirac point position* (*V*)	*Mobility* (cm^2/Vs)	*Dirac point position* (*V*)	*Mobility* (cm^2/Vs)	*Dirac point position* (*V*)
V_{DS} = 10 *mV*	630	3	591	3	381	3
V_{DS} = 20 *mV*	609	3	585	3	378	3
V_{DS} = 30 *mV*	600	3	577	3	377	3
DEVICE 4b	contacts 3 - 4		contacts 5 - 6		contacts 7 - 8	
before annealing	*Mobility* (cm^2/Vs)	*Dirac point position* (*V*)	*Mobility* (cm^2/Vs)	*Dirac point position* (*V*)	*Mobility* (cm^2/Vs)	*Dirac point position* (*V*)
V_{DS} = 10 *mV*	654	28	694	27	626	29
V_{DS} = 20 *mV*	638	28	682	27	619	29
V_{DS} = 30 *mV*	639	28	685	28	623	28
after annealing	*Mobility* (cm^2/Vs)	*Dirac point position* (*V*)	*Mobility* (cm^2/Vs)	*Dirac point position* (*V*)	*Mobility* (cm^2/Vs)	*Dirac point position* (*V*)
V_{DS} = 10 *mV*	678	5	688	4	653	5
V_{DS} = 20 *mV*	656	5	673	4	644	5
V_{DS} = 30 *mV*	655	5	673	4	644	5
DEVICE 4i	contacts 3 - 4		contacts 5 - 6		contacts 7 - 8	
before annealing	*Mobility* (cm^2/Vs)	*Dirac point position* (*V*)	*Mobility* (cm^2/Vs)	*Dirac point position* (*V*)	*Mobility* (cm^2/Vs)	*Dirac point position* (*V*)
V_{DS} = 10 *mV*	284	30	292	29	439	30
V_{DS} = 20 *mV*	280	30	293	29	438	30
V_{DS} = 30 *mV*	283	30	291	29	431	30
after annealing	*Mobility* (cm^2/Vs)	*Dirac point position* (*V*)	*Mobility* (cm^2/Vs)	*Dirac point position* (*V*)	*Mobility* (cm^2/Vs)	*Dirac point position* (*V*)
V_{DS} = 10 *mV*	358	4	344	3	494	4
V_{DS} = 20 *mV*	353	4	343	3	483	4
V_{DS} = 30 *mV*	349	4	336	4	482	4

Table 4.12: Sample T07. Data extracted from the gate voltage dependent measurements: maximum mobility μ_{FE} extracted with Eq. 3.11 and Dirac point position.

4.2.1 Conclusions

The data extracted can be summarized as following:

- The **contact resistance** R_c of sample T07 is highly decreased with respect to the contact resistance of sample T01. While the T01 has values between 700 and 3000 Ω, the T07 shows a resistance between 60 and 200 Ω.

- Comparing the values of R_c before and after the annealing, it slightly increases (tens of Ω) in part of the devices of sample T07, while a higher affect is visible in sample T01, where it increases more than 1000 Ω.

- In term of **unit length contact resistance** the values found are quite high with respect the ones reported in literature [65]. Values from 30 to 120 $K\Omega/sq$ are extracted in sample T01 and between 3 and 9 $K\Omega/sq$ in sample T07.

  It is important to consider that the graphene in both the samples is inhomogeneous. The current injected in the channels could found a faster path through a zone in which the graphene has locally higher performance. For this reason, a normalization process using the total channel dimensions can lead to a wrong evaluation of the properties.

- The **resistance of the graphene channels** R_{gr} and thus the **sheet resistance** R_s in sample T07 is higher than that in sample T01. Values of R_{gr} mainly between 600 and 1000 Ω are found in sample T07 and values between 200 and 800 Ω are found in sample T01.

- The annealing procedure also affects the resistance of the channel. In particular, in sample T01, values of sheet resistance R_s between 1400 and 2000 Ω/sq are found before annealing, while values between 3500 and 5000 Ω/sq are found after it. In sample T07, R_s ranges between 4000 and 6000 Ω/sq before annealing and between 5000 and 9000 Ω/sq after it.

- The **maximum field effect mobility** ranges between 800 and 1200 cm^2/Vs in sample T01 and between 300 and 700 cm^2/Vs in sample T07. It remains more or less unvaried before and after the annealing, only a slight decrease in detected some devices.

- The **Dirac point** in sample T07 initially ranges around 27-30 V and then shifts to values around 3-5 V after the annealing. In sample T01 initially it is at values higher than 40 V and then shifts to 11-13 V.

Some considerations can be done. The contact resistance is decreased by the presence of the edges that, as expected, helps the adhesion and the charge injection between metal and graphene. This behaviour has been already proved by Ref. [18] in which enhanced carried injection has been achieved by forming cuts in the graphene within the contact regions. These cuts facilitated bonding between the contact metal and carbon atoms at the graphene cut edges, maximizing the current injection.

The decrease of the contact resistance also prove that the new graphene surface has higher reactivity than the standard monolayer.

The resistance of sample T07 is higher mostly because the graphene is less doped, as can be seen by the difference in the position of the Dirac point of the two samples.

The scattering of the electrons, due to the presence of a high number of edges, leads to a slight decrease in the mobility, which also contributes in the increasing of the sheet resistance.

In both the samples the resistance after annealing increases because removing the moisture the doping lever decreases, thus the graphene becomes less conductive.

The difference in the position of the Dirac point is only about 25 V in sample T07 while is more accentuated in sample T01. The presence of the graphene islands in sample T07 acts as a screen to shield the effect of the environment. The moisture can attach to the more reactive not continuous layer and leave almost unaltered the properties of the other continuous one.

Due to the screen effect of the top layer, graphene in sample T07 is less doped already before the annealing. Furthermore, the change in resistance due to the procedure is less marked in sample T07 than in sample T01 and no change in mobility is seen.

Another proof of the shield effect is the high change in the contact resistance of sample T01 after annealing, that cannot be seen in sample T07. The contact resistance depend as well on the doping level, because the metal contacts generate a potential energy barriers [13] that change with the doping level. Thus a low variation in the contact resistance means low change in the doping level.

In conclusion, this material meets all the requirements for sensing applications. It is conductive as a standard single layer graphene, but has a lot of reactive sites suitable for functionalization.

The reactivity is enhanced by the presence of the edges as can be seen by the reduced contact resistance, although ultimate proof of the high reactivity will be given only by functionalization, which is currently being carried.

The low doping level leads to a more sensible sensor, since the material can be used where it is more sensitive, i.e. at the maximum slope of the trans-characteristic, i.e. maximum transconductance.

Furthermore, the shield effect of the top layer can increase the selectivity of the sensor. The highly conductive bottom layer can accurately sense the effect of exposure to specific molecules that react with the chemical species added with functionalization while the top reactive layer can shield the effect of other substances of the environment.

The combined properties of the two layers offer the possibility of high sensitive and selective detectors.

Chapter 5

Conclusions and future work

Chemical vapour deposition growth is one of the most promising technique to produce large area graphene with high electronic properties.

This dissertation reported on the investigation and optimization of graphene CVD growth parameters in order to achieve a novel functional material combining high conductivity, field effect and chemical reactivity, to be used for sensing application.

In this work different protocols have been developed with the aim to synthesize a bilayer graphene with of a bottom continuous layer covered by top discontinuous one, consisting of small "islands". The bottom layer ensures high conductivity, while the top offers a large number of edges and therefore is highly reactive and suitable for functionalization. The combined properties of the two layers offers therefore the possibility of assembling detectors, as the highly conductive bottom layer can accurately sense the effect of exposure to specific molecules.

Overall, the work can be summarized as following:

- Materials production and optimization of growing parameters. Starting from the parameters normally used for the growth of polycrystalline single layer graphene on Cu, the effect of pressure, temperature, growth time and gas flow ratio have been investigated and optimized in order to obtain an homogeneous bottom layer, with densely packed amount of small island on top to maximize the number of available edges.

- Materials characterization. The grown graphene has been transfered on a $Si - SiO_2$ substrate and the samples have been analysed by means of optical and Raman analysis. Optical analysis allowed the visualization of the morphology of the surface and Raman analysis proved the presence of single or few layers graphene in the different areas.

- Devices fabrication. Two sets of devices, one with the standard CVD monolayer and one with the "functional" CVD layer have been simultaneously fabricated in order to compare the electrical properties of the two materials.

- Electrical measurements. Two-probe and four-probe I-V measurements have been performed in order to extract sheet resistance, contact resistance and mobility of the devices.

For the change of the growing parameters the following consideration can be done.

First at all, a temperature of at least $1000\,^{\circ}C$ is needed to allow the decomposition of the methane and permit a uniform graphene growth.

Higher methane flow lead to higher concentration of carbon atom on the surface, thus the formation of few layers graphene is promoted but it is not a necessary condition for the growth of bilayers. Pressure is another important parameter to be considered. A higher pressure enhance the probability of few layers nucleation, with limited effect on the amount of carbon flow.

The presence of the argon atmosphere helps the multi-layer growth, increasing the pressure of the chamber, but argon atoms can act as wearing agent and erode part of the graphene layers already deposited.

Longer growth time does not lead to larger islands size, only their concentration is partially enhanced. It can also be noted that very long growth time (more than 3 hours) in presence of high carbon concentration can induce the deposition of amorphous carbon.

Those consideration confirms the complexity of the growth mechanism, and the difficulty in controlling it. In addition to the parameters here taken in consideration, there are many other factors that can be scarcely controlled. Among the others, the contamination of the chamber, maybe

due to previous growth, plays an important role. The chamber and the small tube used to hold the samples are always cleaned before starting a new process, but the presence of a small contamination is inevitable.

The electric measurements proved the effectively increase in the reactivity of the rough surface with respect to the flat one. Contact resistance almost one other of magnitude less has been measured.

Furthermore, the rough surface is less doped and its properties are less affected by the annealing procedure. The Dirac point shifted only about 20 V and the mobility remained almost unvaried. The presence of the graphene islands acts as a screen to shield the effect of the environment.

On the other hand, a loss in the electrical performances is found. Sheet resistance is increased and mobility is decreased. This can be attributed to the presence of the islands, that, rising the number of edges, enhances the scattering of the electrons through the channel.

Overall, the data analysed proves:

- The presence of a high quality bottom continuous layer, with low doping and good conductivity. The top layer provides edges for functionalization, without losing the overall conductivity of the film.
- The decreasing of the contact resistance, although is still high, respect the standard CVD graphene. The material is considerably more reactive. The effect can be compared with the one achieved in Ref. [18] in which the lower contact resistance has been reached in the same way by increasing the number of edges, but with the need of a complex procedure to pattern the contact area.

Future work

This material exhibit high transparency, stretchability and charge carrier mobility, making it suitable for next generation of stretchable and transparent electronics.

The combination of high conductivity with the high density of edges makes it ideally suited for sensing application, accomplishing the goal of this work.

A chemical sensor is a device that converts information about the concentration of a chemical specie in an electrical signal. Sensors consist of two elements: a receptor and a transducer. The receptor can be any organic or inorganic material with a specific interaction with one analyte or group of analytes. The transducer, instead, converts chemical information into a measurable signal [1].

Graphene can be used as perfect transducer, due to its electronic structure and high surface to volume ratio that can lead to a very high sensitivity [7].

In most of the structure a functionalization is needed to tailor the chemical specificity of the sensor [4]. Specific molecules have to be attached to the graphene surface, often by means of a chemical reaction.

The presence of defects on the graphene surface in sensor applications is not disadvantageous, it helps the functionalization procedure since chemical reactions occur preferentially on edges and defects and not at the basal plane of the graphene sheet [1].

On the other hand, a graphene surface with a lot of edges is a very disordered material, thus with very low conductivity. Furthermore, functionalization changes a single layer graphene from conductive to resistive, since the covalent bonding induces a large amount of sp_3 sites into the graphene lattice [7].

A material with at the same time high conductivity and a lot of edges available would meet all the requirements to have a very high performances transducer.

An example of a possible sensor's structure is shown in Figure 5.1. A graphene channel, on top of an insulating substrate, is placed between two electrical contacts. The surface is functionalized and the presence of the analyte is detected by measuring the change in the resistivity of the channel.

The surface developed in this work matches all the requirements to have highly sensitive and selective sensors. The presence of the islands allows the functionalization process, promoting chemical reaction at their edges, while the continuous monolayer keeps its conductive properties.

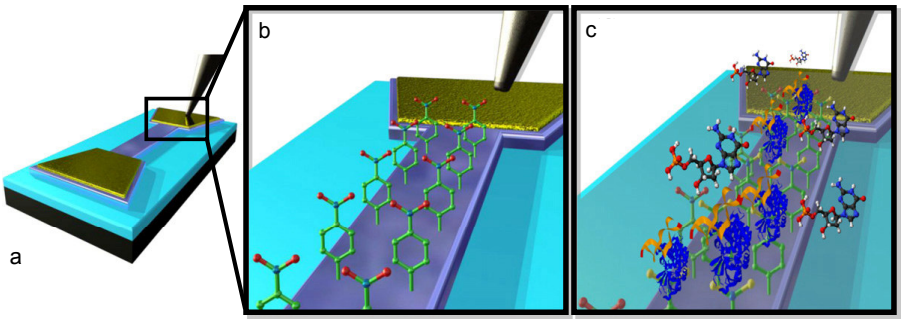

Figure 5.1: Illustration of a graphene channel sensor. a) Schematic of the device. b) Graphene surface after functionalization. c) Attachment of the analyte and subsequent detection by change in the resistivity of the channel. Adapted from [4]

The low doping level of the bottom layer leads to a more sensible sensor, since the material is used near the maximum slope of the trans-characteristic, where it is more sensitive.

Furthermore, the shield effect of the top layer increase the selectivity of the sensor since the highly conductive bottom layer accurately sense the interaction of specific molecules with the chemical species added with functionalization while the top reactive layer shield the effect of other substances of the environment.

A single layer transducer with its entire volume exposed to the surroundings can be obtained, with the advantage to have an almost monolayer structure in which the electronical properties are already known and the sensitivity is very high.

The devices investigated in this work are being tested for chemical functionalization in order to assess their suitability for detection of human chorionic gonadotropin, a cancer risk biomarker.

Bibliography

[1] M. Pumera. Graphene in biosensing. *Materials Today*, 14(7-8):308–315, 2011.

[2] K. S. Novoselov, V. I. Fal'ko, L. Colombo, P. R. Gellert, M. G. Schwab, and K. Kim. A roadmap for graphene. *Nature*, 490(7419):192–200, 2012.

[3] F. Bonaccorso, A. Lombardo, T. Hasan, Z. P. Sun, L. Colombo, and A. C. Ferrari. Production and processing of graphene and 2d crystals. *Materials Today*, 15(12):564–589, 2012.

[4] Z. Tehrani, G. Burwell, M. A. Mohd Azmi, A. Castaing, R. Rickman, J. Almarashi, P. Dunstan, A. Miran Beigi, S. H. Doak, and O. J. Guy. Generic epitaxial graphene biosensors for ultrasensitive detection of cancer risk biomarker. *2D Materials*, 1(2):025004, 2014.

[5] Phaedon Avouris and Christos Dimitrakopoulos. Graphene: synthesis and applications. *Materials Today*, 15(3):86–97, 2012.

[6] M. Pumera, A. Ambrosi, A. Bonanni, E. L. K. Chng, and H. L. Poh. Graphene for electrochemical sensing and biosensing. *TrAC - Trends in Analytical Chemistry*, 29(9):954–965, 2010.

[7] S. Teixeira, G. Burwell, A. Castaing, D. Gonzalez, R. S. Conlan, and O. J. Guy. Epitaxial graphene immunosensor for human chorionic gonadotropin. *Sensors and Actuators, B: Chemical*, 190:723–729, 2014.

[8] T. Kuila, S. Bose, A. K. Mishra, P. Khanra, N. H. Kim, and J. H. Lee. Chemical functionalization of graphene and its applications. *Progress in Materials Science*, 57(7):1061–1105, 2012.

[9] R. Sharma, J. H. Baik, C. J. Perera, and M. S. Strano. Anomalously large reactivity of single graphene layers and edges toward electron transfer chemistries. *Nano Letters*, 10(2):398–405, 2010.

[10] A. K. Geim and K. S. Novoselov. The rise of graphene. *Nature Materials*, 6(3):183–191, 2007.

[11] A. H. Castro Neto, F. Guinea, N. M. R. Peres, K. S. Novoselov, and A. K. Geim. The electronic properties of graphene. *Reviews of Modern Physics*, 81(1):109–162, 2009.

[12] M. C. Lemme, T. J. Echtermeyer, M. Baus, B. N. Szafranek, J. Bolten, M. Schmidt, T. Wahlbrink, and H. Kurz. Mobility in graphene double gate field effect transistors. *Solid-State Electronics*, 52(4):514–518, 2008.

[13] P. Avouris. Graphene: Electronic and photonic properties and devices. *Nano Letters*, 10(11):4285–4294, 2010.

[14] D. C. Elias, R. V. Gorbachev, A. S. Mayorov, S. V. Morozov, A. A. Zhukov, P. Blake, L. A. Ponomarenko, I. V. Grigorieva, K. S. Novoselov, F. Guinea, and A. K. Geim. Dirac cones reshaped by interaction effects in suspended graphene. *Nature Physics*, 7(9):701–704, 2011.

[15] S. De and J. N. Coleman. Are there fundamental limitations on the sheet resistance and transmittance of thin graphene films? *ACS Nano*, 4(5):2713–2720, 2010.

[16] Phaedon Avouris and Fengnian Xia. Graphene applications in electronics and photonics. *MRS Bulletin*, 37(12):1225–1234, 2012.

[17] F. Schwierz. Graphene transistors. *Nature Nanotechnology*, 5(7):487–496, 2010.

[18] J. T. Smith, A. D. Franklin, D. B. Farmer, and C. D. Dimitrakopoulos. Reducing contact resistance in graphene devices through contact area patterning. *ACS Nano*, 7(4):3661–3667, 2013.

[19] A. B. Kuzmenko, E. Van Heumen, F. Carbone, and D. Van Der Marel. Universal optical conductance of graphite. *Physical Review Letters*, 100(11), 2008.

[20] C. Casiraghi, A. Hartschuh, E. Lidorikis, H. Qian, H. Harutyunyan, T. Gokus, K. S. Novoselov, and A. C. Ferrari. Rayleigh imaging of graphene and graphene layers. *Nano Letters*, 7(9):2711–2717, 2007.

[21] P. Blake, E. W. Hill, A. H. Castro Neto, K. S. Novoselov, D. Jiang, R. Yang, T. J. Booth, and A. K. Geim. Making graphene visible. *Applied Physics Letters*, 91(6), 2007.

[22] T. J. Booth, P. Blake, R. R. Nair, D. Jiang, E. W. Hill, U. Bangert, A. Bleloch, M. Gass, K. S. Novoselov, M. I. Katsnelson, and A. K. Geim. Macroscopic graphene membranes and their extraordinary stiffness. *Nano Letters*, 8(8):2442–2446, 2008.

[23] C. Lee, X. Wei, J. W. Kysar, and J. Hone. Measurement of the elastic properties and intrinsic strength of monolayer graphene. *Science*, 321(5887):385–388, 2008.

[24] A. K. Geim. Graphene: Status and prospects. *Science*, 324(5934):1530–1534, 2009.

[25] K. P. Loh, Q. Bao, P. K. Ang, and J. Yang. The chemistry of graphene. *Journal of Materials Chemistry*, 20(12):2277–2289, 2010.

[26] K. S. Novoselov, D. Jiang, F. Schedin, T. J. Booth, V. V. Khotkevich, S. V. Morozov, and A. K. Geim. Two-dimensional atomic crystals. *Proceedings of the National Academy of Sciences of the United States of America*, 102(30):10451–10453, 2005.

[27] W. Kern and G. L. Schnable. Low-pressure chemical vapor-deposition for very large-scale integration processing - review. *Ieee Transactions on Electron Devices*, 26(4):647–657, 1979.

[28] X. S. Li, W. W. Cai, J. H. An, S. Kim, J. Nah, D. X. Yang, R. Piner, A. Velamakanni, I. Jung, E. Tutuc, S. K. Banerjee, L. Colombo, and R. S. Ruoff. Large-area synthesis of high-quality and uniform graphene films on copper foils. *Science*, 324(5932):1312–1314, 2009.

[29] J. C. Shelton, H. R. Patil, and J. M. Blakely. Equilibrium segregation of carbon to a nickel (111) surface: A surface phase transition. *Surface Science*, 43(2):493–520, 1974.

[30] A. Reina, X. Jia, J. Ho, D. Nezich, H. Son, V. Bulovic, M. S. Dresselhaus, and K. Jing. Large area, few-layer graphene films on arbitrary substrates by chemical vapor deposition. *Nano Letters*, 9(1):30–35, 2009.

[31] M. E. Ramn, A. Gupta, C. Corbet, D. A. Ferrer, H. C. P. Movva, G. Carpenter, L. Colombo, G. Bourianoff, M. Doczy, D. Akinwande, E. Tutuc, and S. K. Banerjee. Cmos-compatible synthesis of large-area, high-mobility graphene by chemical vapor deposition of acetylene on cobalt thin films. *ACS Nano*, 5(9):7198–7204, 2011.

[32] K. S. Kim, Y. Zhao, H. Jang, S. Y. Lee, J. M. Kim, K. S. Kim, J. H. Ahn, P. Kim, J. Y. Choi, and B. H. Hong. Large-scale pattern growth of graphene films for stretchable transparent electrodes. *Nature*, 457(7230):706–710, 2009.

[33] X. Li, Y. Zhu, W. Cai, M. Borysiak, B. Han, D. Chen, R. D. Piner, L. Colomba, and R. S. Ruoff. Transfer of large-area graphene films for high-performance transparent conductive electrodes. *Nano Letters*, 9(12):4359–4363, 2009.

[34] S. Bae, H. Kim, Y. Lee, X. Xu, J. S. Park, Y. Zheng, J. Balakrishnan, T. Lei, H. Ri Kim, Y. I. Song, Y. J. Kim, K. S. Kim, B. zyilmaz, J. H. Ahn, B. H. Hong, and S. Iijima. Roll-to-roll production of 30-inch graphene films for transparent electrodes. *Nature Nanotechnology*, 5(8):574–578, 2010.

[35] X. Li, C. W. Magnuson, A. Venugopal, R. M. Tromp, J. B. Hannon, E. M. Vogel, L. Colombo, and R. S. Ruoff. Large-area graphene single crystals grown by low-pressure chemical vapor deposition of methane on copper. *Journal of the American Chemical Society*, 133(9):2816–2819, 2011.

[36] N. Petrone, C. R. Dean, I. Meric, A. M. Van Der Zande, P. Y. Huang, L. Wang, D. Muller, K. L. Shepard, and J. Hone. Chemical vapor deposition-derived graphene with electrical performance of exfoliated graphene. *Nano Letters*, 12(6):2751–2756, 2012.

[37] X. S. Li, C. W. Magnuson, A. Venugopal, J. H. An, J. W. Suk, B. Y. Han, M. Borysiak, W. W. Cai, A. Velamakanni, Y. W. Zhu, L. F. Fu, E. M.

Vogel, E. Voelkl, L. Colombo, and R. S. Ruoff. Graphene films with large domain size by a two-step chemical vapor deposition process. *Nano Letters*, 10(11):4328–4334, 2010.

[38] A. W. Robertson and J. H. Warner. Hexagonal single crystal domains of few-layer graphene on copper foils. *Nano Letters*, 11(3):1182–1189, 2011.

[39] A. W. Tsen, L. Brown, R. W. Havener, and J. Park. Polycrystallinity and stacking in cvd graphene. *Accounts of Chemical Research*, 46(10):2286–2296, 2013.

[40] Y. B. Zhang, T. T. Tang, C. Girit, Z. Hao, M. C. Martin, A. Zettl, M. F. Crommie, Y. R. Shen, and F. Wang. Direct observation of a widely tunable bandgap in bilayer graphene. *Nature*, 459(7248):820–823, 2009.

[41] L. X. Liu, H. L. Zhou, R. Cheng, W. J. Yu, Y. Liu, Y. Chen, J. Shaw, X. Zhong, Y. Huang, and X. F. Duan. High-yield chemical vapor deposition growth of high-quality large-area ab-stacked bilayer graphene. *Acs Nano*, 6(9):8241–8249, 2012.

[42] Z. Q. Tu, Z. C. Liu, Y. F. Li, F. Yang, L. Q. Zhang, Z. Zhao, C. M. Xu, S. F. Wu, H. W. Liu, H. T. Yang, and P. Richard. Controllable growth of 1-7 layers of graphene by chemical vapour deposition. *Carbon*, 73:252–258, 2014.

[43] Z. Z. Sun, A. R. O. Raji, Y. Zhu, C. S. Xiang, Z. Yan, C. Kittrel, E. L. G. Samuel, and J. M. Tour. Large-area bernal-stacked bi-, tr-, and tetralayer graphene. *Acs Nano*, 6(11):9790–9796, 2012.

[44] S. Nie, W. Wu, S. R. Xing, Q. K. Yu, J. M. Bao, S. S. Pei, and K. F. McCarty. Growth from below: bilayer graphene on copper by chemical vapor deposition. *New Journal of Physics*, 14, 2012.

[45] K. Yan, H. L. Peng, Y. Zhou, H. Li, and Z. F. Liu. Formation of bilayer bernal graphene: Layer-by-layer epitaxy via chemical vapor deposition. *Nano Letters*, 11(3):1106–1110, 2011.

[46] Z. Q. Luo, T. Yu, J. Z. Shang, Y. Y. Wang, S. Lim, L. Liu, G. G. Gurzadyan, Z. X. Shen, and J. Y. Lin. Large-scale synthesis of bi-

layer graphene in strongly coupled stacking order. *Advanced Functional Materials*, 21(5):911–917, 2011.

[47] S. Chen, W. Cai, R. D. Piner, J. W. Suk, Y. Wu, Y. Ren, J. Kang, and R. S. Ruoff. Synthesis and characterization of large-area graphene and graphite films on commercial cu-ni alloy foils. *Nano Letters*, 11(9):3519–3525, 2011.

[48] P. Blake, P. D. Brimicombe, R. R. Nair, T. J. Booth, D. Jiang, F. Schedin, L. A. Ponomarenko, S. V. Morozov, H. F. Gleeson, E. W. Hill, A. K. Geim, and K. S. Novoselov. Graphene-based liquid crystal device. *Nano Letters*, 8(6):1704–1708, 2008.

[49] Y. Hernandez, V. Nicolosi, M. Lotya, F. M. Blighe, Z. Sun, S. De, I. T. McGovern, B. Holland, M. Byrne, Y. K. Gun'ko, J. J. Boland, P. Niraj, G. Duesberg, S. Krishnamurthy, R. Goodhue, J. Hutchison, V. Scardaci, A. C. Ferrari, and J. N. Coleman. High-yield production of graphene by liquid-phase exfoliation of graphite. *Nature Nanotechnology*, 3(9):563–568, 2008.

[50] S. Wang, Y. Zhang, N. Abidi, and L. Cabrales. Wettability and surface free energy of graphene films. *Langmuir*, 25(18):11078–11081, 2009.

[51] M. Lotya, Y. Hernandez, P. J. King, R. J. Smith, V. Nicolosi, L. S. Karlsson, F. M. Blighe, S. De, W. Zhiming, I. T. McGovern, G. S. Duesberg, and J. N. Coleman. Liquid phase production of graphene by exfoliation of graphite in surfactant/water solutions. *Journal of the American Chemical Society*, 131(10):3611–3620, 2009.

[52] T. Hasan, F. Torrisi, Z. Sun, D. Popa, V. Nicolosi, G. Privitera, F. Bonaccorso, and A. C. Ferrari. Solution-phase exfoliation of graphite for ultrafast photonics. *Physica Status Solidi (B) Basic Research*, 247(11-12):2953–2957, 2010.

[53] Q. H. Wang, K. Kalantar-Zadeh, A. Kis, J. N. Coleman, and M. S. Strano. Electronics and optoelectronics of two-dimensional transition metal dichalcogenides. *Nature Nanotechnology*, 7(11):699–712, 2012.

[54] F. H. L. Koppens, T. Mueller, Ph Avouris, A. C. Ferrari, M. S. Vitiello, and M. Polini. Photodetectors based on graphene, other two-

dimensional materials and hybrid systems. *Nat Nano*, 9(10):780–793, 2014.

[55] H. Ma, D. Wu, Z. Cui, Y. Li, Y. Zhang, B. Du, and Q. Wei. Graphene-based optical and electrochemical biosensors: A review. *Analytical Letters*, 46(1):1–17, 2012.

[56] W. Liu, H. Li, C. Xu, Y. Khatami, and K. Banerjee. Synthesis of high-quality monolayer and bilayer graphene on copper using chemical vapor deposition. *Carbon*, 49(13):4122–4130, 2011.

[57] H. D. Hu, C. B. Ma, and Z. W. Liu. Plasmonic dark field microscopy. *Applied Physics Letters*, 96(11), 2010.

[58] A. Das, S. Pisana, B. Chakraborty, S. Piscanec, S. K. Saha, U. V. Waghmare, K. S. Novoselov, H. R. Krishnamurthy, A. K. Geim, A. C. Ferrari, and A. K. Sood. Monitoring dopants by raman scattering in an electrochemically top-gated graphene transistor. *Nat Nano*, 3(4):210–215, 2008.

[59] P. Yu and M. Cardona. *Fundamentals of Semiconductors: Physics and Materials Properties*. Springer, Heidelberg, 2010.

[60] A. C. Ferrari and D. M. Basko. Raman spectroscopy as a versatile tool for studying the properties of graphene. *Nature Nanotechnology*, 8(4):235–246, 2013.

[61] A. C. Ferrari, J. C. Meyer, V. Scardaci, C. Casiraghi, M. Lazzeri, F. Mauri, S. Piscanec, D. Jiang, K. S. Novoselov, S. Roth, and A. K. Geim. Raman spectrum of graphene and graphene layers. *Physical Review Letters*, 97(18):187401, 2006.

[62] A. Venugopal, L. Colombo, and E. M. Vogel. Contact resistance in few and multilayer graphene devices. *Applied Physics Letters*, 96(1), 2010.

[63] J. Krupka. Contactless methods of conductivity and sheet resistance measurement for semiconductors, conductors and superconductors. *Measurement Science and Technology*, 24(6), 2013.

[64] A. P. Schuetze, W. Lewis, C. Brown, and W. J. Geerts. A laboratory on the four-point probe technique. *American Journal of Physics*, 72(2):149–153, 2004.

[65] F. Xia, V. Perebeinos, Y. M. Lin, Y. Wu, and P. Avouris. The origins and limits of metal-graphene junction resistance. *Nature Nanotechnology*, 6(3):179–184, 2011.

[66] M. F. Craciun, S. Russo, M. Yamamoto, and S. Tarucha. Tuneable electronic properties in graphene. *Nano Today*, 6(1):42–60, 2011.

[67] K. S. Novoselov, A. K. Geim, S. V. Morozov, D. Jiang, Y. Zhang, S. V. Dubonos, I. V. Grigorieva, and A. A. Firsov. Electric field in atomically thin carbon films. *Science*, 306(5696):666–669, 2004.

[68] B. Radisavljevic, A. Radenovic, J. Brivio, V. Giacometti, and A. Kis. Single-layer mos2 transistors. *Nat Nano*, 6(3):147–150, 2011.

[69] M. R. Connolly, K. L. Chiou, C. G. Smith, D. Anderson, G. A. C. Jones, A. Lombardo, A. Fasoli, and A. C. Ferrari. Scanning gate microscopy of current-annealed single layer graphene. *Applied Physics Letters*, 96(11), 2010.